

PASSIVATED EMITTER REAR SIDE CONTACT SOLAR CELLS

A THESIS SUBMITTED TO
THE GRADUATE SCHOOL OF NATURAL AND APPLIED SCIENCES
OF
MIDDLE EAST TECHNICAL UNIVERSITY

BY

ZEYNEP NİLÜFER ÖZTÜRK

IN PARTIAL FULFILLMENT OF THE REQUIREMENTS
FOR
THE DEGREE OF MASTER OF SCIENCE
IN
PHYSICS

JANUARY 2016

Approval of the thesis:

PASSIVATED EMITTER REAR SIDE CONTACT SOLAR CELLS

submitted by **ZEYNEP NİLÜFER ÖZTÜRK** in partial fulfillment of the requirements for the degree of **Master of Science in Physics Department, Middle East Technical University** by,

Prof. Dr. Gülbin Dural Ünver
Dean, Graduate School of **Natural and Applied Sciences**

Prof. Dr. Mehmet T. Zeyrek
Head of Department, **Physics**

Prof. Dr. Raşit Turan
Supervisor, **Physics Dept., METU**

Examining Committee Members:

Prof. Dr. Bülent Akınoğlu
Physics Dept., METU

Prof. Dr. Raşit Turan
Physics Dept., METU

Prof. Dr. Mehmet Parlak
Physics Dept., METU

Assoc. Prof. Dr. Alpan Bek
Physics Dept., METU

Assist. Prof. Dr. Tunay Tansel
Institute of Nuclear Sciences, Hacettepe University

Date: 29.01.2016

I hereby declare that all information in this document has been obtained and presented in accordance with academic rules and ethical conduct. I also declare that, as required by these rules and conduct, I have fully cited and referenced all material and results that are not original to this work.

Name, Last name : Zeynep Nilüfer Öztürk

Signature :

ABSTRACT

PASSIVATED EMITTER REAR SIDE CONTACT SOLAR CELLS

Öztürk, Zeynep Nilüfer
M.Sc. Department of Physics
Supervisor: Prof. Dr. Raşit Turan

January 2016, 91 pages

The purpose of this research is to identify the production processes and working principles of passivated emitter and rear contact (PERC) solar cells and produce working PERC samples.

PERC solar cells are extremely promising among next generation industrialized solar cells due to their high efficiencies and low costs. Backside of a PERC cell is coated with dielectric layer with micro holes that increases the recombination time thus increases the overall efficiency. Moreover, the top surface of the cell is textured with pyramids and bottom surface of the cell is polished which provides better light confinement as well as increases quantum efficiencies at longer wavelengths. Thus, PERC cells have crucial importance for the solar cell industry.

PERC solar cell's working principle is very close to standard photovoltaic solar cell working principle. However, PERC cells have some benefits due to its design difference. The most important difference of PERC cell design is local back surface field metal contacts and passivation layer. Backside of a PERC cell is coated with dielectric layer with laser opening holes for back surface metal contacts that decrease the recombination which is directly associated to the overall efficiency. If an electron is generated near the rear side of the conventional solar cell, it is recombined by back

surface metallization layer and it doesn't contribute to the overall cell current. However, the dielectric layer of PERC solar cells restrains the electron-aluminium metallization layer attraction. Hence, most of the electrons do reach the depletion region and contribute to the current.

Back side metal coverage percentage is the most important parameter for PERC solar cells. With the Transmission Line Method (TLM) measurements, laser parameters were optimized. In this thesis work, EO Technics Super Mark GF pulsed (nanosecond) laser having 1064 nm wavelength, 200 ns pulsed width, 4.5 kW peak power for 30kHz and 30 μ m focal spot size was used. Laser parameters of having 100% power (27.5 Watt), 5493 mm/s velocity and 25% power (4.75 Watt), 586mm/sec velocity were chosen for the laser ablation. Back side metal coverage percentage is also aimed to be parametrized. Power 100% and velocity 5493 mm/s laser parameter resulted in better results according to other chosen laser parameter. Highest efficiency of 14.1 was obtained with 10% back surface metal coverage percentage parameter. Moreover, PERC cell production results exceeded the results of reference cell produced.

Keywords: *PERC solar cells, Back surface passivation.*

ÖZ

PASİVE EDİLMİŞ YAYICI ARKA KONTAK GÜNEŞ HÜCRELERİ

Öztürk, Zeynep Nilüfer
Yüksek Lisans Fizik Bölümü
Tez Yöneticisi: Prof. Dr. Raşit Turan

Ocak 2016, 91 sayfa

Bu tez çalışmasının amacı pasive edilen yayıcı arka kontak güneş hücresi (PERC) üretim basamakları ve çalışma prensiplerini irdelemek ve çalışan PERC güneş hücresi üretmek.

PERC güneş hücreleri yüksek verimliliğinden ve düşük üretim maliyetinden ötürü güneş panelleri endüstrisinde gelecek vaadeden önemli bir güneş paneli çeşididir. PERC güneş hücresinin arka yüzeyi dielektrik malzemeyle kaplanarak mikro deliklerin açılması elektronların birleşme zamanını arttırarak toplam verimliliği arttırmaktadır. Bunlara ek olarak hücrenin üst piramitlerle yapılandırılması ve arka yüzeyinin parlatılması ışığı daha iyi güneş hücresinin içine hapsederek uzun dalga boylarından verimlilik elde etmemizi sağlar. Bu sebeplerden ötürü PERC güneş hücreleri güneş enerji sektöründe çok değerli bir yere sahiptir.

PERC güneş hücrelerinin çalışma prensibi standart fotovoltajik güneş hücrelerinin çalışma prensibine çok benzerdir. Lakin PERC güneş hücresinin dizayn farkından ötürü çeşitli avantajları vardır. PERC güneş hücre dizaynının standart güneş hücresinden en önemli farkı lokal arka yüzey alan kontakları ve arka yüzey pasivasyon katmanıdır. PERC güneş hücresinin arka yüzeyine kaplanan dielektrik katman ve lazerle açılan delikler elektronların tekrar birleşmesini yavaşlatarak hücrede toplam elde edilen verimliliği arttırır.

Eğer bir elektron standard güneş hücresinin arka yüzeyine yakın üretilirse, o elektron arka yüzey metalizasyon katmanı tarafından yeniden birleştirilir ve toplam üretilen akıma katılmaz.

Lakin PERC güneş hücrelerindeki dielektrik katman, elektron-alüminyum metalizasyon katmanı arasındaki çekimi güçlendirmektedir. Bu sayede, çoğu elektron tükenim bölgesine ulaşarak akıma katkı sağlamaktadır.

Arka yüzey metal kaplama yüzde parametresi PERC güneş hücreleri için en önemli değişkendir. Lazer parametreleri iletim çizgi yöntemi (TLM) ölçüleriyle optimize edilmiştir. Bu tez çalışmasında, 1064 nm dalga boyu, 200 ns darbe süresi, 4.5 kWatt maksimum gücü (30kHz için) ve 30 µm odak nokta boyutuna sahip EO Technics Super Mark GF darbeleri (nanosaniye) lazer kullanılmıştır. Lazer ablasyon parametreleri; %100 güçte (27.5 Watt), 5493 mm/s hızda ve %25 güçte (4.75 Watt), 586mm/s hızda olmak üzere 2 tane seçilmiştir. Arka yüzey metal kaplama yüzde parametresi optimizasyonu da hedeflenmiştir. %100 güçte ve 5493 mm/s lazer parametresinde ve %10 arka yüzey kaplama yüzdesinde en yüksek 14.1 verimlilik elde edilmiştir. Ek olarak, PERC güneş hücresi üretim sonuçları referans güneş hücresi üretimini sonuçlarından daha yüksek elde edilmiştir.

Anahtar Kelimeler: *PERC güneş hücreleri, Arka yüzey pasivasyonu.*

To my dearest husband, family and friends...

ACKNOWLEDGEMENTS

I would like to thank Professor Raşit TURAN for giving me the opportunity of working with him and being a member of GÜNAM family. I will be always grateful to him for his guidance, endless support and patience. I would also like to thank Prof. Dr. Mehmet PARLAK, Prof. Dr. Bülent AKINOĞLU, Assoc. Prof. Dr. Alpan BEK, Assist. Prof. Dr. Tunay TANSEL for all their help and kind attitude towards me.

I would like to continue with Fırat ES. He is the best group leader that a student can ever have. I don't know how I can pay for so many things he has done for me. He has always been a great teacher, lab-partner, supporter, brother and a real friend for me. I need to continue with Hande ÇİFTPINAR. She is the one who has always been ready for help with a great smile on her pretty face. She gave me her hand when I was struggling and she has always been a great friend for me.

I would also like to thank GÜNAM researches Kamil ÇINAR, Olgu DEMİRCİOĞLU, Serra ALTINOLUK, Engin ÖZKOL, Hisham NASSER, Pantea AURANG, Arezoo HOSSEINI, Zişan İrem ÖZYURT and Gence BEKTAŞ for their help and friendship.

I also need to thank all GUNAM staff including Harun TANIK, Buket GÖKBAKAN and Tuncay GÜNGÖR for their kind attitude since I participated into the group. I would like to thank our technical staff Nevzat GÖRMEZ, Tayfun YILDIZ and Dursun ERDOĞAN. I would like to continue with our pretty department secretaries Gülşen ÖZDEMİR PARLAK and Zeynep EKE for their endless help and positive attitude for all seven years that I spent in METU physics department.

I would also like to thank my dearest friends Şeyda ŞAHİNER, Nilhan GÜRTUNA and Burcu ALTUNTAŞ for being in my life.

I would like to thank my mother in law Melek ÖZTRÜK, my father in law Mustafa ÖZTÜRK. They make me feel like as I am their biological daughter. They always support me and I am very lucky to have them. My sister in laws Göksu and Cansu ÖZTÜRK behaves me as I am their real sister. I love my new family so much.

I would like to thank my grandmother Hatice Sivrikaya, especially my mother Mine Güven, my father Zeki Güven, my sister Yasemen Güven Kutlu and my brother in law Veysel Kutlu. I can barely find the words to express all their wisdom, love and support they have given me. I love all of them so much. I am very lucky to have as great family as them.

I need to thank my the deceased grandfather Ahmet Tevfik Sivrikaya:

I miss you so much. I love you so much. I wish we had more time together. You were the best grandfather a child could ever have. I always remember and will remember all the things you said, taught to me.

And finally, to my dearest husband İbrahim Murat Öztürk:

You are the best husband in the world. You are my lover, my best friend, my soulmate, my joy of life, my everything... I've never had a moment of doubt. I love you so much... I believe in you completely. You are my dearest one. My reason for life... I would like to thank you so much for providing me with unfailing support and continuous encouragement throughout my years of study and through the process of researching and writing this thesis. This accomplishment would not have been possible without you.

TABLE OF CONTENTS

ABSTRACT	v
ÖZ.....	vii
ACKNOWLEDGEMENTS	x
TABLE OF CONTENTS	xii
LIST OF TABLES	xv
LIST OF FIGURES.....	xvi
CHAPTERS	
1 INTRODUCTION.....	1
1.1 History of Photovoltaics	2
1.2 Types of Photovoltaic Solar Cells	4
1.2.1 Crystalline Silicon Solar Cells	4
1.2.2 Thin Film Solar Cells	5
1.2.3 Organic & Dye Sensitized Solar Cells	6
1.2.4 III-V Semiconductors	7
1.3 Fundamental Concepts of Photovoltaic Technology	7
1.3.1 Solar Irradiation.....	7
1.3.2 Basics of Photovoltaic Solar Cell Operation.....	8

2	FUNDAMENTALS OF CRYSTALLINE SILICON SOLAR CELL TECHNOLOGY	15
2.1	Introduction	15
2.2	Basic Steps of Standard Crystalline Silicon Solar Cell Production	16
2.2.1	Texturing	16
2.2.2	Doping	18
2.2.3	Anti-reflection Coating	21
2.2.4	Metallization	22
3	PASSIVATED EMITTER REAR CONTACT (PERC) SOLAR CELLS	25
3.1	Structure of PERC Solar Cell	25
3.2	Working Principles of PERC Solar Cell	26
3.3	Literature Review of PERC Solar Cells	27
4	EXPERIMENTAL PROCEDURES	37
4.1	PERC Solar Cell Fabrication Procedure	37
4.1.1	Single side etching	39
4.1.2	Backside passivation	41
4.1.3	Laser structuring.....	42
5	RESULTS AND DISCUSSION	45
5.1	Single side etching results	45
5.1.1	HNA and HF+HNO ₃ solution single side etching	45
5.1.2	KOH-H ₂ O ₂ alkaline solution single side etching.....	52
5.2	Backside Passivation Results	59
5.3	Laser Structuring Results	61

5.4 Rear Surface Metal Coverage.....	63
5.5 Produced PERC solar cell results	66
5.5.1 First PERC solar cell production.....	66
5.5.2 Second PERC solar cell production	69
5.5.3 Third PERC solar cell production	75
6 CONCLUSIONS.....	83
REFERENCES.....	87

LIST OF TABLES

TABLES

Table 1: Different rear passivation results table [40].....	32
Table 2: Efficiency results of pyramid smoothing thicknesses [42]	34
Table 3: Transmission line method results.....	62
Table 4: Result table of first production	67
Table 5: SunsVoc results of first production	68
Table 6: Reference production solar cell results	73
Table 7: Characterization data obtained from 0% back surface metal coverage sample and reference sample.....	75
Table 8: Characterization results of laser parameter 1 [power= 100%, velocity= 5493 mm/s]	75
Table 9: Characterization results of laser parameter 2 [power= 25%, velocity= 586 mm/s]	76

LIST OF FIGURES

FIGURES

Figure 1. Becquerel’s photoconductivity investigation set-up.....	2
Figure 2. Best cell efficiency results graph of National Renewable Energy Laboratory, Adopted from [5].....	3
Figure 3: Fabrication methods of crystalline solar modules [6].....	5
Figure 4: Flexible thin film solar cell [9]	6
Figure 5: Band gap energy diagram of a semiconductor	9
Figure 6: Schematic diagram of a photovoltaic solar cell adopted from [14].....	9
Figure 7: Illuminated diode I-V curve example	10
Figure 8: Ideal, real I-V curve and Fill Factor calculation.....	12
Figure 9: Cross section of crystalline silicon solar cell structure adopted from [6]...	16
Figure 10: Spectral irradiance of silicon, adopted from [20]	17
Figure 11: Pyramid surface texturing light trapping schematic	17
Figure 12 : Crystal structure of intrinsic, p-type and n-type doped silicon.....	19
Figure 13: Electron-hole pair separation in depletion region adopted from [26].....	19
Figure 14: Energy band diagram of n-type semiconductor, p-type semiconductor, adopted from [16].....	20
Figure 15: Reflectance of antireflective layer coated silicon wafer	21
Figure 16: Transmission line method measurement contacts	22

Figure 17: Voltage-current graph of ohmic contact.....	23
Figure 18: Resistance vs distance graph of TLM sample	24
Figure 19: Front surface metallization design.....	24
Figure 20: Standard and PERC solar cell structure.....	26
Figure 21: Schematic diagram of PERC cell fabricated by Blakers Group, adopted from [34]	28
Figure 22: Fabricated PERC cell design of ISFH Group, adopted from [36].....	29
Figure 23: Process details after HF dip [39]	31
Figure 24: Process flow of PERC cell in this thesis work	38
Figure 25: SEM picture of pyramid textured surface.....	39
Figure 26: Total reflection graph of polished and pyramid textured wafer	39
Figure 27: Specular reflection graph of polished and pyramid textured wafer.....	40
Figure 28: Specular and Diffuse Reflection.....	41
Figure 29: Laser speed-power graph of frequency 30kHz.....	43
Figure 30: Total reflection AM 1.5 G weighted percentage graph of HF-HNO ₃ -H ₂ O (420 ml-280 ml-45 ml) polishing solution.....	46
Figure 31: Specular reflection AM 1.5 G weighted percentage graph of HF-HNO ₃ - H ₂ O (420 ml-280 ml-45 ml) polishing solution	46
Figure 32: Total and specular reflection AM1.5 G weighted percentage graph of samples treated with HF+HNO ₃ (420 ml/280 ml) polishing solution	47
Figure 33: Optical microscope photographs of wafer etched in HF+HNO ₃ (420ml/280ml) polishing solution and bare pyramid textured wafer surface (x1500 magnification)	48
Figure 34: Total and specular reflection AM 1.5G weighted percentage graph of HF- HNO ₃ -CH ₃ COOH (100 ml-150 ml-300 ml)	49

Figure 35: Total and specular reflection AM 1.5G weighted percentage graph of HF-HNO ₃ -CH ₃ COOH (60 ml-450 ml-150 ml)	49
Figure 36: Total and specular reflection AM 1.5G weighted percentage graph of HF-HNO ₃ -CH ₃ COOH (60 ml-450 ml-150 ml) with magnetic stirring effect	50
Figure 37: SEM images of surface etched by HF-HNO ₃ -CH ₃ COOH (60 ml-450 ml-150 ml) with magnetic stirring for 20 minute	51
Figure 38: Total and specular reflection AM 1.5G weighted percentage graph of surface etched in HF-HNO ₃ -CH ₃ COOH (60 ml-450 ml-150 ml) solution in ultrasonic cleaner manually stirred with previous magnetic stirring effect	51
Figure 39: SEM pictures of surface etched by HF-HNO ₃ -CH ₃ COOH (60 ml-450 ml-150 ml) solution in ultrasonic cleaner manually stirred with previous magnetic stirring effect	52
Figure 40: Total reflection AM 1.5G weighted percentage graph of etched surfaces in KOH-H ₂ O ₂ -H ₂ O (40%-20%-40%) solution.....	53
Figure 41: Total reflection AM 1.5G weighted percentage graph of etched and silicon nitride covered surfaces in KOH-H ₂ O ₂ -H ₂ O (40%-20%-40%) solution.....	53
Figure 42: Optical microscope images of bare and silicon nitride covered surfaces in KOH-H ₂ O ₂ -H ₂ O (40%-20%-40%) solution with respect to time [All images are at 1500x magnification]	54
Figure 43: Total reflection AM1.5G weighted percentage graph of etched surfaces in KOH-H ₂ O ₂ -H ₂ O (40%-10%-40%) solution.....	55
Figure 44: Etch rate of KOH-H ₂ O ₂ -H ₂ O (40%-10%-40%) solution.....	55
Figure 45: Optical microscope images of etched surfaces in KOH-H ₂ O ₂ -H ₂ O (40%-10%-40%) solution with respect to process time [All images are at 1500x magnification]	56

Figure 46: SEM images of etched surface in KOH-H ₂ O ₂ -H ₂ O (40%-10%-40%) solution with etching time 480 s	56
Figure 47: Rear side n-layer etching and etching thickness results	57
Figure 48: PERC sample front surface sheet resistance graph	58
Figure 49: PERC sample rear surface sheet resistance graph	58
Figure 50: SEM pictures of, (a) silicon nitride covered front surface and (b) etched rear surface of the PERC sample	59
Figure 51: Average life-time graphs of samples done for PERC process.....	60
Figure 52: Life-time measurement graph of PERC set sample.....	60
Figure 53: Transmission line method measurement preparation procedure	61
Figure 54: SEM view of TLM sample 1 (Table 3)	63
Figure 55: SEM view of TLM sample 4 (Table 3)	63
Figure 56: Calculation of laser writing frequency [Green lines represents laser writing, blue square represents rear surface of the wafer, x represents distance between laser written-lines]	64
Figure 57: Quakka simulation result graph of Fill Factor (FF) and Open circuit voltage (Voc) vs. rear surface metal coverage percentage.....	65
Figure 58: Quakka simulation result graph of Efficiency and Short circuit current (Jsc) vs rear surface metal coverage.....	65
Figure 59: Quakka simulation result of loss percentages vs. rear surface metal coverage	66
Figure 60: Open circuit volrage and fill factor vs. back metal coverage graph.....	67
Figure 61: Efficiency and short circuit current vs. back metal coverage graph.....	68

Figure 62: SEM images of aluminium local back contacts (a) view of aluminium local back contacts after the laser writing, (b) and (c) are zoomed pictures showing the cross-section. 69

Figure 63: Open circuit current and Fill Factor vs. Back metal coverage graph of laser parameter 1 [velocity: 586 mm/s, frequency: 30 kHz, power: 25%]..... 71

Figure 64: Open circuit current and Fill Factor vs. Back metal coverage graph of laser parameter 2 [velocity: 5493 mm/s, frequency: 30kHz, power: 100%]..... 71

Figure 65: Efficiency and short circuit current vs. Back metal coverage graph of laser parameter 1 [velocity: 586 mm/s, frequency: 30 kHz, power: 25%] 72

Figure 66: Efficiency and Jsc vs. Back metal coverage graph of samples produced using laser parameter 2 [velocity: 5493 mm/s, frequency: 30kHz, power: 100%] 72

Figure 67: Pseudo efficiency [SunsV_{oc} results] versus back metal coverage graph .. 73

Figure 68: Pseudo Fill Factor [SunsV_{oc} results] versus back metal coverage graph . 74

Figure 69: i-V_{oc} [SunsV_{oc} results] versus Back metal coverage graph 74

Figure 70: Fill Factor versus back surface metal coverage graph of laser parameter 1 [Power= 100%, velocity= 5493 mm/sec]..... 77

Figure 71: Open circuit voltage versus back surface metal coverage graph of samples produced using the laser parameter 1 [Power= 100%, velocity= 5493 mm/sec]..... 78

Figure 72: Short circuit current density versus back surface metal coverage graph of samples produced using the laser parameters [Power= 100%, velocity= 5493 mm/s and power= 25%, velocity= 586 mm/s] compared to the reference sample 78

Figure 73: Efficiency vs. back surface metal coverage graph of the sample produced using the laser parameters [Power= 100%, velocity= 5493 mm/sec (orange dots) and Power= 25%, velocity= 586 mm/s (green dots)] compared to the reference sample. 79

Figure 74: Current-voltage graph of best produced PERC cell compared to the reference cell 80

Figure 75: External Quantum Efficiency vs. wavelength graph of reference cell and best *short circuit current density* cell..... 80

Figure 76: SEM images of laser parameter 1 [Power=100%, velocity=5493 mm/s] with calculated back surface metal coverage values of (a) 5 %, (b) 14 %, (c) 50 %. 81

CHAPTER 1

INTRODUCTION

Energy resources have been crucially important for human being since ancient ages. With the advancement of technology and increase of population, demand for energy resources is dramatically increasing. After industrial revolution, energy resources became the mainstream of economics and political arithmetic all over the world. Fuel and electricity have become as important as oxygen and water for developed countries. However, people should also consider next generations, while consuming the power resources. Hence, countries should meet this growing energy demand in an environmentally safe manner.

Energy resources can be grouped as renewable and non-renewable sources. Non-renewable means the source cannot be recreated and is available in limited supplies. Coal, natural gas are the main examples of non-renewable sources [1]. Non-renewable sources are not only limited sources but also the main problem for atmospheric pollution. Global warming and serious health problems are two unfortunate results of atmospheric pollution due to these energy sources. On the other hand, populations' demand for fuel and electricity cannot be ignored. At this point, renewable energy resources seem to be the solution to all of the problems mentioned above. Wind, solar and geothermal energy are the main types of renewable energy sources [1]. They are unlimited sources of nature and hence are environmentally friendly.

Sun is the unique, clean and infinite source of free power. Radiant light and heat from the sun is the source of life on earth. Plants convert carbon dioxide to oxygen that humans need for living. Furthermore, energy which reaching to earth from the nuclear fusions of the sun can be also converted into electrical and thermal energy

that people need. At this point, photovoltaic solar energy conversion technology becomes a hope for clean energy need of the earth.

The purpose of this research is to identify the production processes and working principles of passivated emitter and rear contact (PERC) solar cells and produce working PERC samples. This thesis is composed of six chapters. Theoretical background of photovoltaic solar cells is explained in the first chapter. Crystalline silicon solar cell working principles and basic fabrication procedures are studied in second chapter. Third chapter of the thesis is aimed to investigate best efficiency PERC cells produced all over the world. Experimental procedures are explained in fourth chapter. Results are investigated in chapter five and discussed in chapter six.

1.1 History of Photovoltaics

Photovoltaics is the subject of the solar energy conversion to electrical energy with the principle of photovoltaic effect. Photovoltaic effect was found by Alexander Edmund Becquerel in 1839 [2]. In other words, physics behind photovoltaic solar cells was found 175 years ago. Edmund Becquerel investigated the p-type and n-type semiconductor electrodes by measuring the photo-electromotive force of the electrolyte solution [3]. He discovered the photocurrent with the set-up as shown in Figure 1.

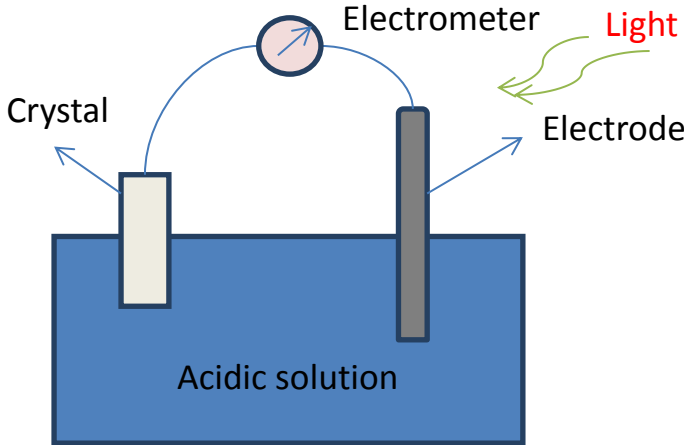


Figure 1. Becquerel’s photoconductivity investigation set-up

In 1873 Willoughby Smith discovered photoconductivity in solids while working with selenium. In 1883 Charles Fritts made the first working solar cells with efficiency lower than 1% [2]. The first silicon solar cell was demonstrated at Bell Laboratory for space applications in 1954 with an efficiency of 6 % [4]. In 1990's photovoltaics became frequently used power source for electronic watches and calculators. The journey of photovoltaic energy conversion science has reached to efficiency percentage of 44 today with the multi-junction solar cell, which can be seen in Figure 2.

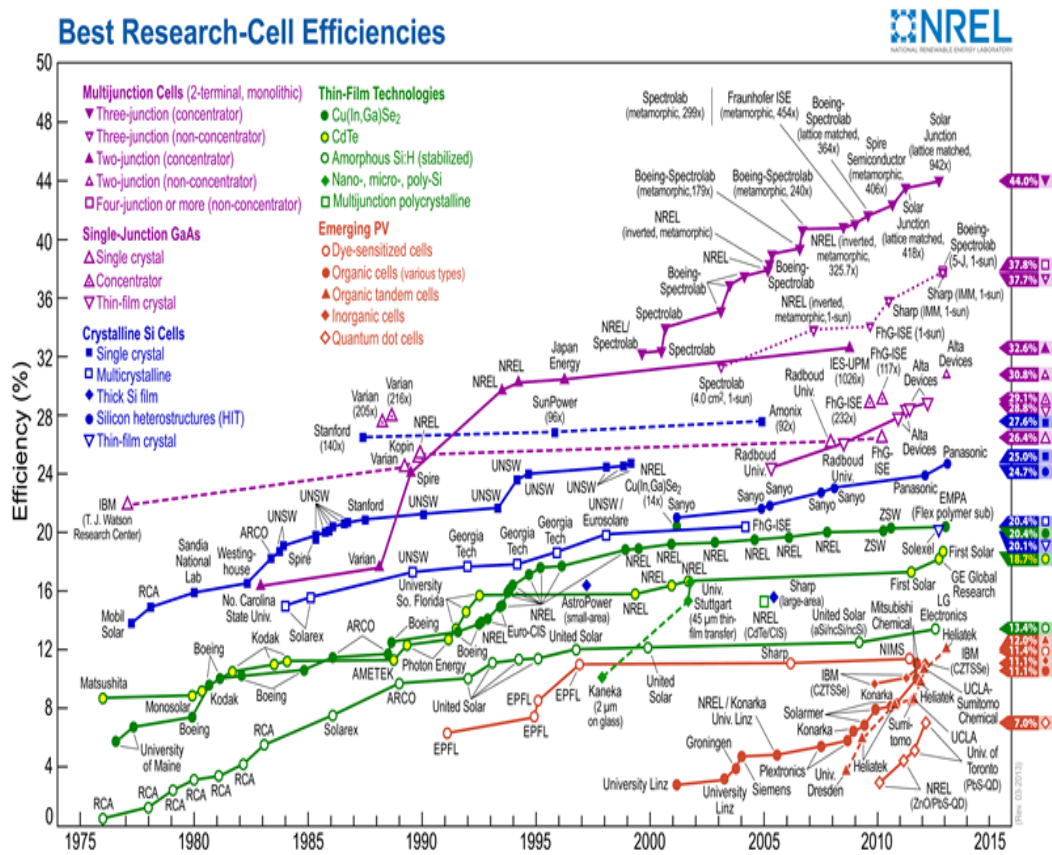


Figure 2. Best cell efficiency results graph of National Renewable Energy Laboratory, Adopted from [5]

1.2 Types of Photovoltaic Solar Cells

1.2.1 Crystalline Silicon Solar Cells

Earth's crust is composed of silicon with a percentage of 26 [6]. Moreover, the efficiency percentages of the crystalline type of photovoltaic devices are very promising. Crystalline silicon solar cell technology has reached efficiency of 27.4 % as can be seen from the Figure 2, NRELS best cell efficiencies all over the world [5]. Moreover, crystalline solar cells are the most commonly used type of solar cell in photovoltaic market.

The crystalline silicon photovoltaic device is a type of silicon based semiconductor device [6]. C-silicon solar cells can be grouped as monocrystalline and multicrystalline solar cells due to their physical properties and the fabrication methods, shown in Figure 3. Monocrystalline silicon solar wafers are sliced from ingots which are grown with the Czochralski method, whereas multicrystalline wafers are sliced from block ingots which are grown with the quartz crucible method [6]. Standard crystalline solar cells are made up of monocrystalline or multicrystalline boron doped p-type silicon substrate. The size of cells are generally square shaped 125 mm by 125 mm or 156 mm by 156 mm [6].

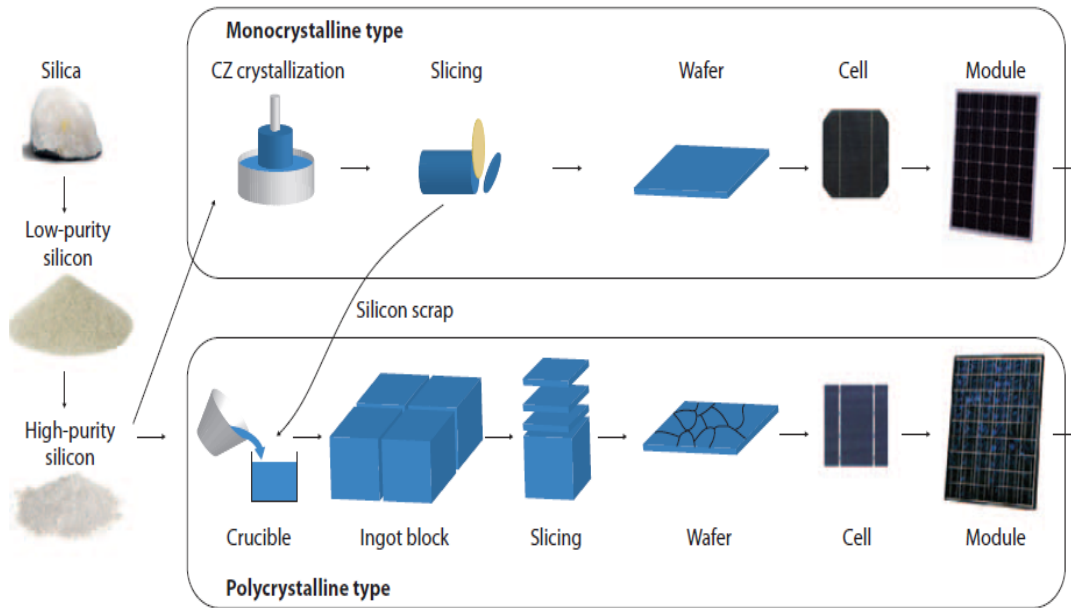


Figure 3: Fabrication methods of crystalline solar modules [6]

The maximum theoretical efficiency of a crystalline solar cell efficiency is 30 % due to silicon's energy band gap, which is 1.1 eV [6]. However, multijunction design of crystalline silicon solar cells is very promising for the efficiency improvements.

1.2.2 Thin Film Solar Cells

Thin film solar cells are second generation solar cells, which are made up of thin layers, deposited on a thick substrate such as glass, metal or plastic. The main logic of thin film solar cells was introduced in 1975 with the proposal of enhancing the optical absorption results in the same efficiency with thinner fabricated solar cells [7]. Most important speciality of thin film solar cells is the low cost of production due to its reduced thickness[8]. However, the main problem of the thin film solar cell fabrication is difficulty in the deposition of thin layer on large areas. Example of a flexible thin film solar cell structure is shown in Figure 4. The most efficient thin film solar cell is announced by Solixel with 20.4 % efficiency, which can be seen from Figure 2 [5].

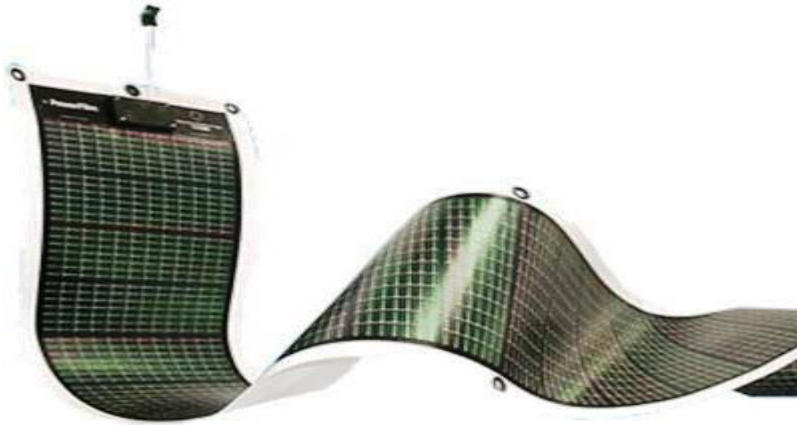


Figure 4: Flexible thin film solar cell [9]

1.2.3 Organic & Dye Sensitized Solar Cells

Organic solar cells are photovoltaic solar cell type produced with organic polymers. In organic solar cells active polymer layer absorbs the light and generate electron-hole pairs. Organic compounds, used for organic solar cell production, have high absorption coefficients. Hence, thin layers of deposition are enough for light confinement for fabrication of organic solar cells, which reduces the cost of production. However, their efficiencies and stability are low according to other solar cell types. The most efficient organic solar cell is announced to have an efficiency of 11.1 % in NREL's efficiency graph [5].

Dye sensitized solar cells (DSSC) are third generation photovoltaic thin film solar cells. In dye sensitized solar cells, sensitizer absorbs the light, generate electron-hole pairs, transports the charge carriers and generates the current [10]. Moreover sensitizers have broad absorption band, which provides cells to harvest large spectral ranges of light. DSSCs have low production cost and easy fabrications techniques as conventional roller printing. The most efficient produced DSSC is reported to have an efficiency of 11.4 % in NREL's best efficiency 2015 graph [5].

1.2.4 III-V Semiconductors

III-V semiconductors are obtained by combination of group III elements and group V elements of periodic table. These compounds have broad energy band gap, which makes them very important for the production of high efficient solar cells. GaAs, InAs and InP are mostly used compounds of III-V semiconductor group for solar cell technologies. However, the production cost of these compounds is extremely high. Generally, they are used for space shuttle technologies. Since, they can produce higher energy from small areas according to other types of solar cell technologies [11].

1.3 Fundamental Concepts of Photovoltaic Technology

1.3.1 Solar Irradiation

Solar irradiation is amount of solar energy reaching a particular area in a particular time. Since, photovoltaic solar cells harvest solar energy into electrical energy. It is very important to calculate the solar irradiation of the sun to find the best position and angle for most efficient harvesting. Temperature of the sun's surface is about 6000 K and it can be approximated as a blackbody. Earth's average distance from sun is approximately 1.5×10^8 km. Hence radiation reaching from sun to earth's atmosphere is only 1.360 W/m^2 , whereas sun's surface having total power density is $5.91 \times 10^7 \text{ W/m}^2$ [7]. However, there exists decrease of solar irradiation density until it reaches to the crust of the earth due to the scattering through the atmosphere. The measure of solar energy reaching the earth may be the air mass (AM) unit, which defines the shortest possible path length of light through the earth's atmosphere. The simplest form of air mass is calculated by following equation [12];

$$\frac{1}{\cos \theta_z} = AM \quad (\text{Eq.1})$$

In Equation 1, ' θ_z ' is the angle of the sun light with the vertical axis. AM calculation is an important parameter for PV panels and cells. Since, it provides an international standard for efficiency measurements.

1.3.2 Basics of Photovoltaic Solar Cell Operation

Conversion process of solar energy into electrical energy by photovoltaic solar cells can be summarized under four main steps. First, light beam from the sun generates electron-hole pair in the vicinity of the depletion region. This process is called generation of carriers. Second, generated carriers are collected to generate current, which is collection of the carriers. Third, generated current is converted into voltage across the solar cell. Final step is to channel obtained power from the solar cell to charge the battery or be used directly by other electrical devices. To understand this four processes, semiconductor material's energy band gap structures should be investigated.

Solar cells are made up of semiconductor materials. Band gap energy diagram of a semiconductor is shown in Figure 5. When a photon, having energy higher than the semiconductor band gap energy, is incident on a solar cell, electron in the valance band of the semiconductor absorbs the photon. Then, that electron is excited to the conduction band [13]. Moreover, the excited electron leaves a hole in the valance band of the semiconductor. This process is the charge generation of solar cell operation.

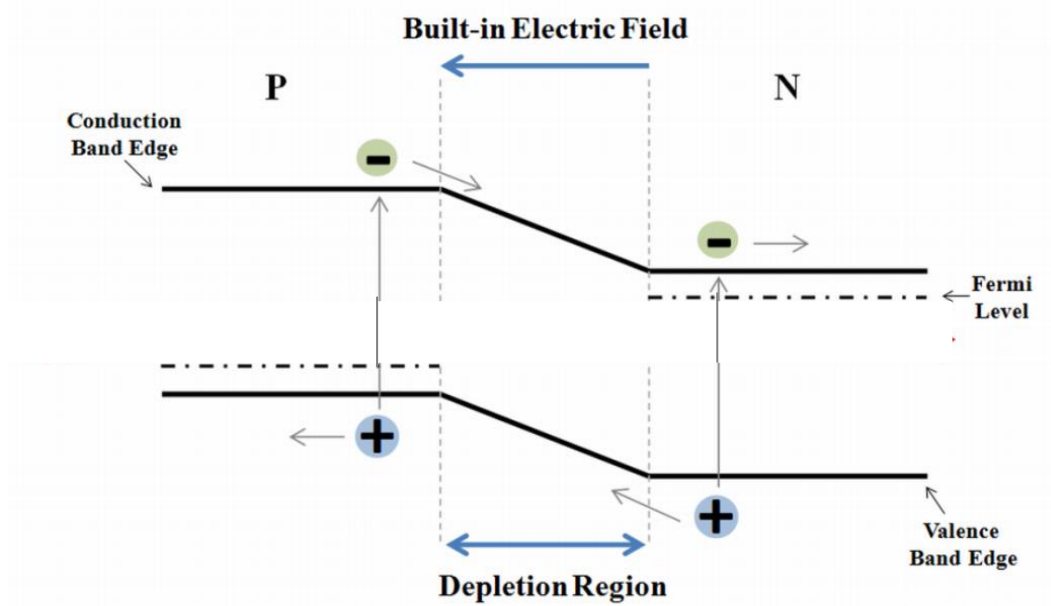


Figure 5: Band gap energy diagram of a semiconductor

Basic photovoltaic solar cell, shown in Figure 6, is composed of front metal finger contacts, anti-reflection coating, p-n junction and back metal contact from top to bottom. Metal contacts supply the electrical conductivity for current transformation. Anti-reflection coating layer is used for better light trapping in the junction. P-n junction generates electron-hole pairs and collects generated pairs.

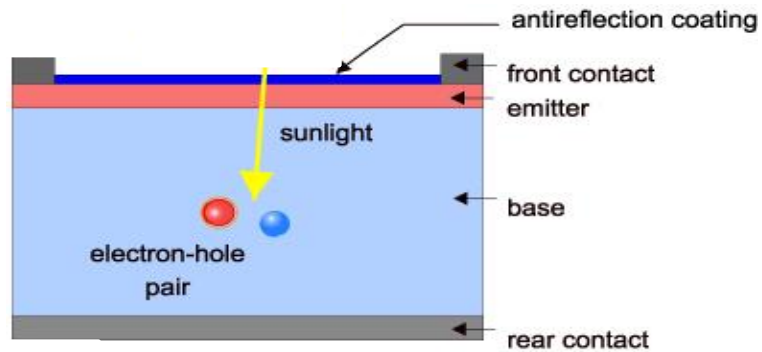


Figure 6: Schematic diagram of a photovoltaic solar cell adopted from [14]

To further understanding of solar cell operation, cell parameters should be investigated:

Diode equation

Photovoltaic solar cells are basically a p-n junction. Hence, they can be treated as diodes. At this point, diode equation should be investigated in order to understand I-V curve of the photovoltaic solar cells. The ideal diode equation is [15]:

$$I = I_0 \cdot (e^{\frac{qV}{kT}} - 1) \quad (\text{Eq.2})$$

I_0 : Dark saturation current

q : Electron charge

k : Boltzmann constant

T : Temperature (in Kelvin)

V : Applied voltage between contacts

I : Current through the diode

However, solar cells are not ideal diodes. Hence, we should calculate the resulting illuminated current by non-ideal diode equation as [15]:

$$I = I_0 \cdot \left(e^{\frac{qV}{nkT}} - 1 \right) - I_L \quad (\text{Eq.3})$$

I_L : Light generated current

n : Ideality factor

By this equation, I-V curve of the photovoltaic solar cells can be drawn. In Figure 7, current voltage graph is illustrated.

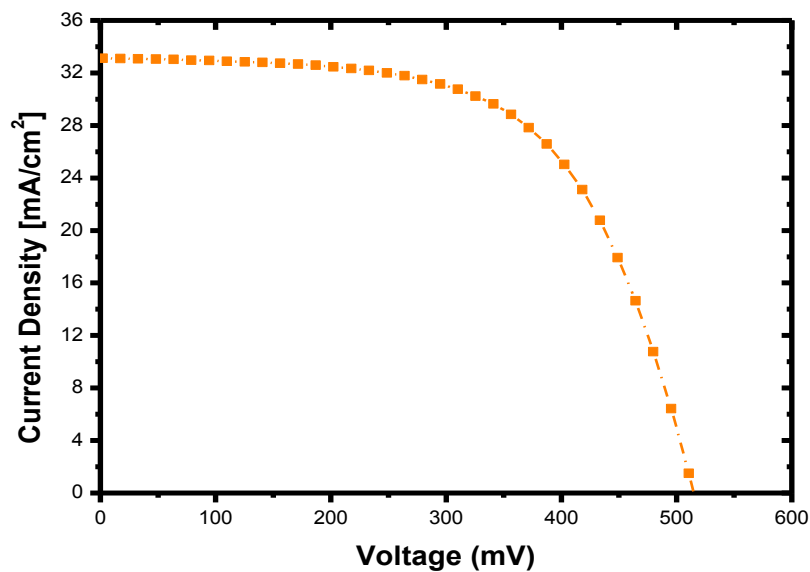


Figure 7: Illuminated diode I-V curve example

Open circuit voltage

When the PV solar cell is illuminated, the maximum voltage measured across the cell is called open circuit voltage (V_{oc}). In Figure 7, V_{oc} is the value of the data where the net current through the cell is zero. Open circuit voltage can be calculated using form the diode equation of the circuit equation by inserting zero value over resulting current through the solar cell in Equation 7. Then the open circuit voltage becomes [15]:

$$V_{OC} = \frac{nkT}{q} \cdot \ln \left(\frac{I_L}{I_0} + 1 \right) \quad (\text{Eq.8})$$

Short circuit current

Short circuit current (I_{sc}) is the maximum current measured when the light is illuminated on the solar cell. Short circuit current indicates the maximum number of carriers which reaches the junction of the solar cell [16]. In Figure 7, I_{sc} is the value where the net voltage through the cell is zero. I_{sc} can be calculated from the diode equation by inserting zero over the voltage in Equation 3. Then the short circuit current becomes equal to the light generated current.

Series resistance

Total resistance of a cell is called as series resistance. When the series resistance of the cell is low, cell becomes more efficient. Resistance of the metal-silicon contact, resistance of front and back metal contacts and the bulk resistance of the semiconductor material of the cell are the main three components to change the series resistance. Series resistance is zero for an ideal solar cell. Hence, diode equation of the solar cell changes with the appearance of series resistance parameter[17]:

$$I = I_L - I_0 \cdot \exp \left(\frac{q(V - IR_s)}{nkT} \right) \quad (\text{Eq.9})$$

Series resistance of the cell can be calculated from this equation.

Shunt resistance

Shunt resistance (R_{SH}) is resistance of the cell, which prevents the light generated current to pass short paths instead of the cell junction. Low shunt resistance is resulting from manufacturing problems. Higher shunt resistance value prevents the current leakage in the cell. Hence, shunt resistance value is infinite for ideal cell. Diode equation changes with the appearance of shunt resistance as[17]:

$$I = I_L - I_0 \cdot \exp\left(\frac{qV}{nkT}\right) - \frac{V}{R_{SH}} \quad (\text{Eq.10})$$

Fill factor

Fill factor (FF) parameter can be basically defined as the measure of the quality of the cell. For the ideal cell I-V curve is like a rectangular between corners of I_{SC} and V_{OC} , as shown in Figure 8. However, real I-V curve is different from ideal. Fill factor is the ratio of the area of the maximum power data square of the real I-V curve and the area of the ideal I_{max} - V_{max} curve as shown in Figure 8.

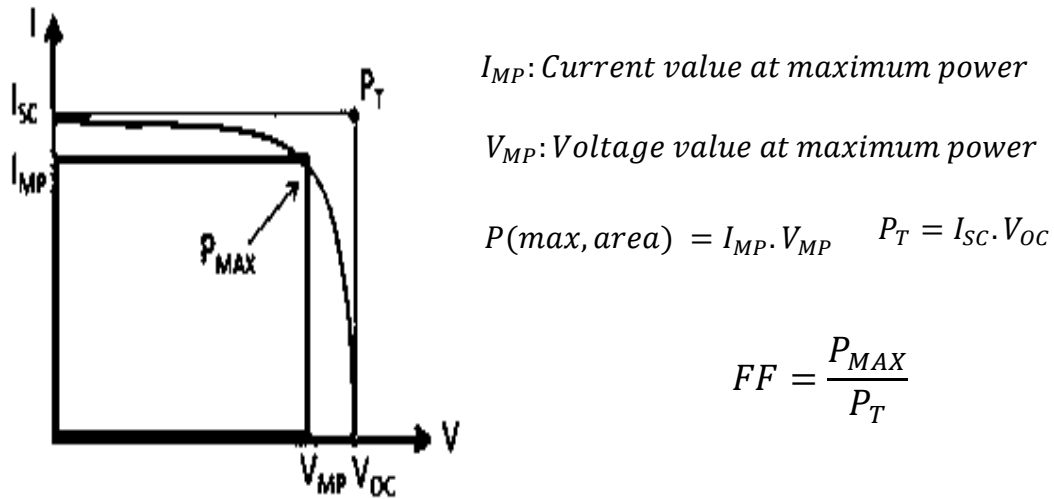


Figure 8: Ideal, real I-V curve and Fill Factor calculation

Efficiency

Efficiency (η) is the cell parameter, which is used to evaluate the cell performance. It is the ratio of resulting maximum power of the illuminated solar cell and the solar power incident on the cell. Standard temperature and standard solar irradiation for measurement of the cell efficiency is at 25°C and for AM 1.5 G [18]. Maximum resulting power of the solar cell, illuminated solar power and efficiency of the standard solar cell can be calculated from[6]:

$$P_{max} = V_{OC} \cdot I_{SC} \cdot FF \quad (\text{Eq.11})$$

$$P_{in} = 1000 \frac{W}{m^2} * \text{cell area [for 1.5AM and 25°C]} \quad (\text{Eq.12})$$

$$\eta = \frac{P_{max}}{P_{in}} \quad (\text{Eq.13})$$

Losses of the solar cell

Ideal silicon solar cells can theoretically have efficiency of around 30 % according to Shockley-Quisser limit [19]. However, the maximum efficiency record of the crystalline silicon solar cell is 26.7 %, as can be seen in Figure 2. For real solar cells recombination loss, high series resistance or low shunt resistance and optical loss problems are the main three loss parameters, which stand in the way of reaching the theoretical limit of efficiency.

CHAPTER 2

FUNDAMENTALS OF CRYSTALLINE SILICON SOLAR CELL TECHNOLOGY

2.1 Introduction

The crystalline silicon solar cell is a type of silicon based semiconductor device. Like all other semiconductor devices, it has a p-n junction. In c-silicon solar cell, electron-hole pairs are generated by absorption of photons and solar energy is converted into electrical energy. To confine more photons inside a solar cell, surface pyramid texturing is used. To reduce reflection losses, anti-reflection coating is processed on the top of pyramid textured surface. Front and back surface metal contacts are formed to collect the generated electrical current.

Standard c-silicon solar cell has a structure of front surface metal contact, anti-reflection coating on a pyramid textured surface, p-n junction, heavily doped region for back surface field and back metal contact from top to bottom. Structure of standard crystalline silicon solar cell design is shown in Figure 9.

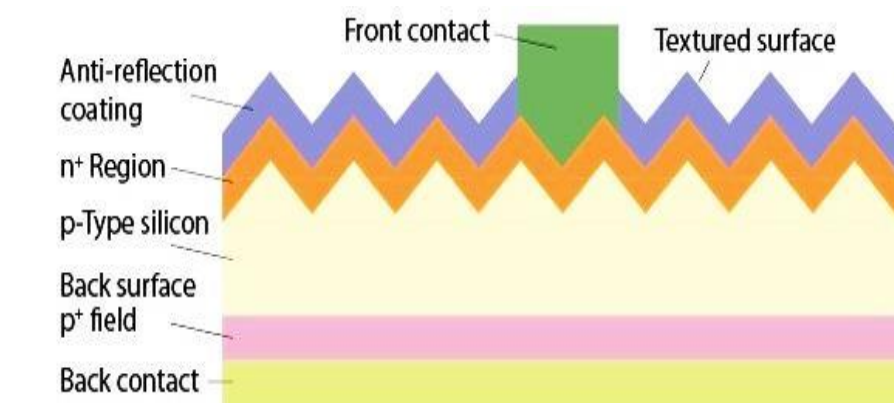


Figure 9: Cross section of crystalline silicon solar cell structure adopted from [6]

In this chapter, basic process steps of crystalline silicon solar cell production are presented. Surface texturing, doping, anti-reflection coating, metallization and edge isolation are the five main steps of standard crystalline silicon cell production.

2.2 Basic Steps of Standard Crystalline Silicon Solar Cell Production

2.2.1 Texturing

Photovoltaic solar cells absorb light and convert it into electrical energy. Absorbed photons generate electron-hole pairs in the cell. Hence, the number of photons absorbed by the cell is crucially important for solar cell efficiency. Silicon is a semiconductor material which has a band gap of 1.12 eV. In other words, silicon can only absorb photons having energy higher than 1.12 eV. This band gap energy corresponds to a wavelength of approximately 1100 nm. As can be seen from the solar spectrum in Figure 10, silicon material can absorb only photons of wavelengths between 300-1100 nm of the solar spectrum efficiently due to its energy band gap.

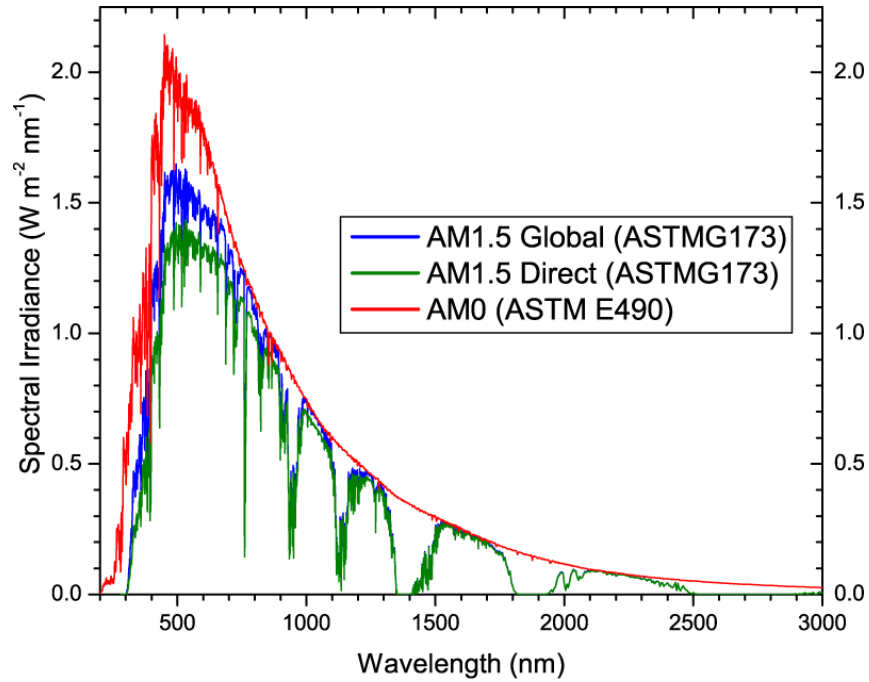


Figure 10: Spectral irradiance of silicon, adopted from [20]

Optical confinement of the solar cell is the most important parameter for the absorption of solar irradiation reaching the solar cell [22]. Light trapping in the cell will increase the number of absorbed photons. One of the most important light trapping methods is pyramid texturing. These techniques decrease the reflection losses of the incoming light and increase the path length of captured photon in the solar cell. The method of the light trapping of pyramid surface texturing can be seen in Figure 11.

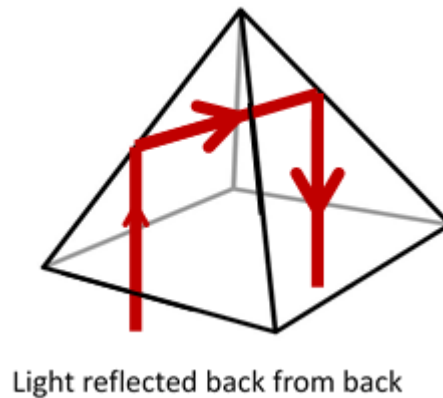


Figure 11: Pyramid surface texturing light trapping schematic

In this thesis work, anisotropic etching in a KOH solution is used for pyramid texturing. KOH with a certain percentage of isopropyl alcohol (IPA) is usually used for these anisotropic etching processes at about 80°C degrees temperature [23]. Etch rate of these alkaline solutions are decided by percentage of KOH, percentage of IPA in the solution and the temperature of the solution. Anisotropic etching of silicon's chemical reaction in KOH alkaline solution is [24];



2.2.2 Doping

Doping process of solar cells changes the balance of electron-hole pairs in the silicon crystal lattice. After the change of this balance, n-type and p-type semiconductor material can be produced. This shifting process forms p-n junction, in other words, active region of the cell. The aim of doping process is to separate the created electron-hole pairs by the balance shift in the silicon crystal lattice.

As mentioned above, semiconductors can be grouped as n-type and p-type semiconductor according to their electron hole pair balance. N-type semiconductor materials have more valance electron, whereas p-type semiconductors have less valance electron. N-type semiconductors are doped with group V elements of periodic table and p-type semiconductors are doped with group III elements of periodic table. To create a balance shift in the silicon crystal lattice, silicon is doped with n-type or p-type semiconductor material. The crystal structures of intrinsic silicon and n-type, p-type doped silicon are shown in Figure 12 [25].

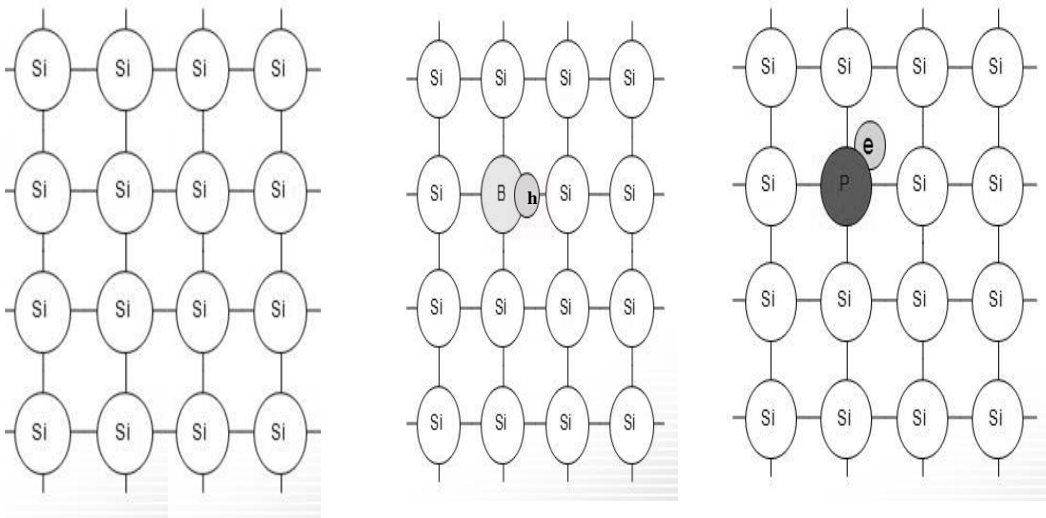


Figure 12 : Crystal structure of intrinsic, p-type and n-type doped silicon

When n-doped silicon and p-type silicon is brought together, an electric field is produced after the equilibrium is reached (Figure 13). This electric field provides to separate created electron hole pairs in the depletion region of the solar cell device, which can be seen in Figure 13.

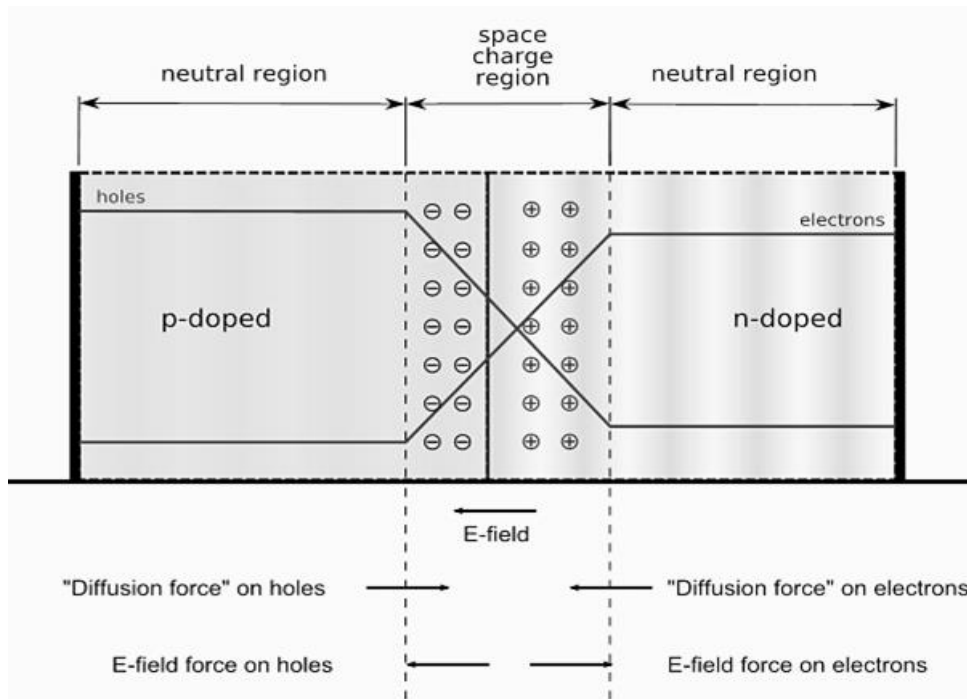


Figure 13: Electron-hole pair separation in depletion region adopted from [26]

In crystalline solar cells, p-n junction is formed by two methods according to the type of silicon wafer. Surface of n-type silicon wafer is doped with boron (Group III-A) atoms to create p-type region or surface of p-type silicon wafer is doped with phosphor (Group V-A) atoms to create n-type region. Silicon belongs to group IV of periodic table, which means silicon has four valence electrons. As group III element boron has three valence electrons, boron shares its three valence electron with silicon forming bonds. Each share between boron and silicon atoms in the lattice results in an extra hole, which makes material p-type semiconductor. As a group V element phosphor has five valence electrons, four of these five valence atoms are shared with Silicon. Hence, there exists an extra valence electron in the lattice. This extra valence electron of each share between phosphor and silicon in the lattice results in extra electron in the material, which makes material n-type material. These extra holes and electrons increase the conductivity of the silicon and changes the energy band diagram.

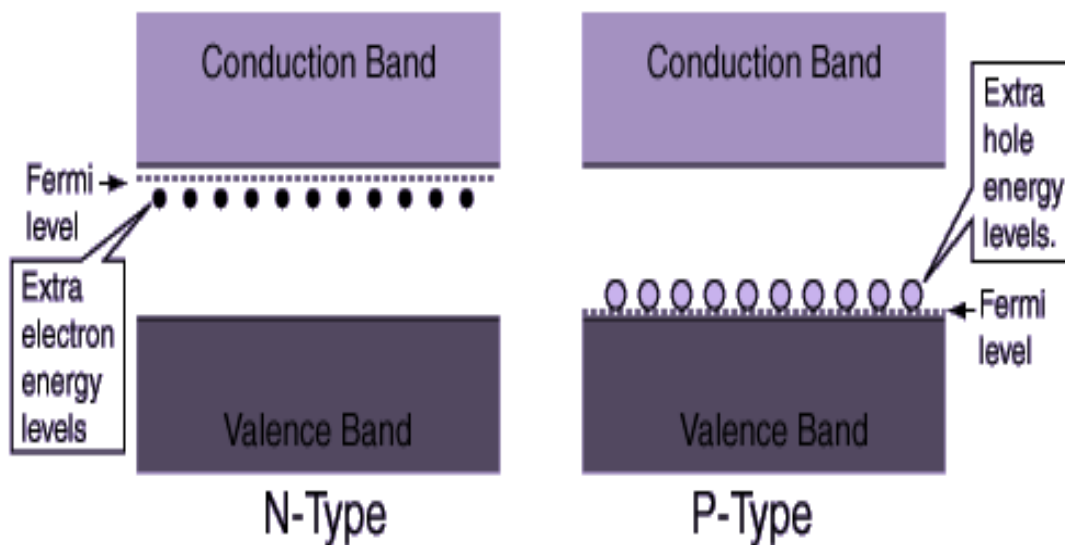


Figure 14: Energy band diagram of n-type semiconductor, p-type semiconductor, adopted from [16]

2.2.3 Anti-reflection Coating

Anti-reflection coating is aimed to decrease the reflection percentage of incoming light to increase the number of absorbed photons [27]. With the increase of number of absorbed photons, generated electron-hole pairs and hence efficiency of the solar cell also increases. The physical mechanism is the interference of the reflected light from the surface top and from the first boundary.

Chemical vapour deposition, spray or screen printing are three main methods for anti-reflection coating techniques [28]. In this thesis work, plasma enhanced chemical vapour deposition method is used for anti-reflection coating process. Moreover, silicon nitride is the chemical compound used as an anti-reflective coating.

Anti-reflection coating is a type of dielectric thin film applied onto top of the surface of the solar cell. Refractive index (n_a) and thickness (t_a) of anti-reflection coating, refractive index (n_s) of semiconductor material and refractive index of surrounding material (n_0) are the main four parameters for the determination of minimum reflectance of solar cells. For crystalline silicon solar cells, 80 nm silicon nitrite anti-reflection coating is mostly applied onto the surface of cell to have best optical confinement by means of interference [29].

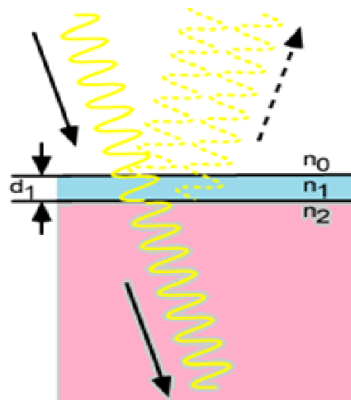


Figure 15: Reflectance of antireflective layer coated silicon wafer

In Figure 15, reflection of light from antireflective layer coated on silicon wafer is illustrated. Reflectance is decreased dramatically with the anti-reflection coating.

2.2.4 Metallization

Metallization process of production is aimed to collect optimally all the charges generated in the cell. Back surface of solar cell is fully coated with metal to have electrical contact, whereas front surface of solar cell is coated with finger shaped metals to have electrical contact so that to let the incoming light fall onto the cell with minimal reflection by the contacts. Thermal evaporation and screen printing are the two main methods for metallization process. In this thesis work, thermal evaporation process is used for back metal contact, whereas screen printing is the procedure for the front finger and grid contacts.

In order to have good electrical contact for solar cells, contact resistance should be very low. Current-voltage measurements (transmission line method) are carried out to find the contact resistances. In the case of a good contact design, I-V curve of the transmission line should be linear. In other words, a linear curve graph shows good ohmic contact, as shown in Figure 17 [17].

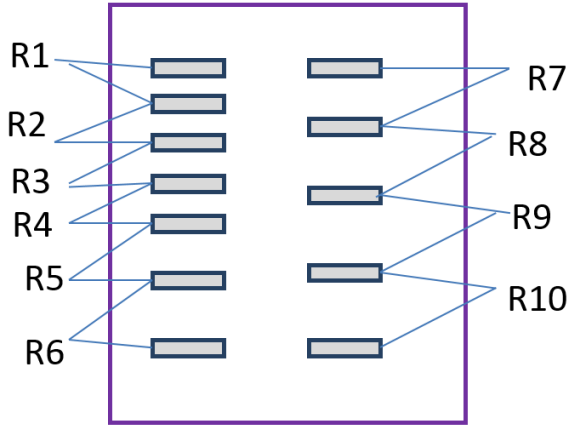


Figure 16: Transmission line method measurement contacts

Transmission line method (TLM) is a method to measure the contact resistance by eliminating the sheet resistance of the semiconductor [30]. To measure the resistance, metal contacts are coated over nitrite surface of the solar cell with different distances as shown in Figure 16. After metal evaporation process, current-voltages of R1 to R10 coupling of the metal contacts as shown in Figure 16 and resistances are measured. From slopes of I-V graphs contact resistances are calculated (Figure 17).

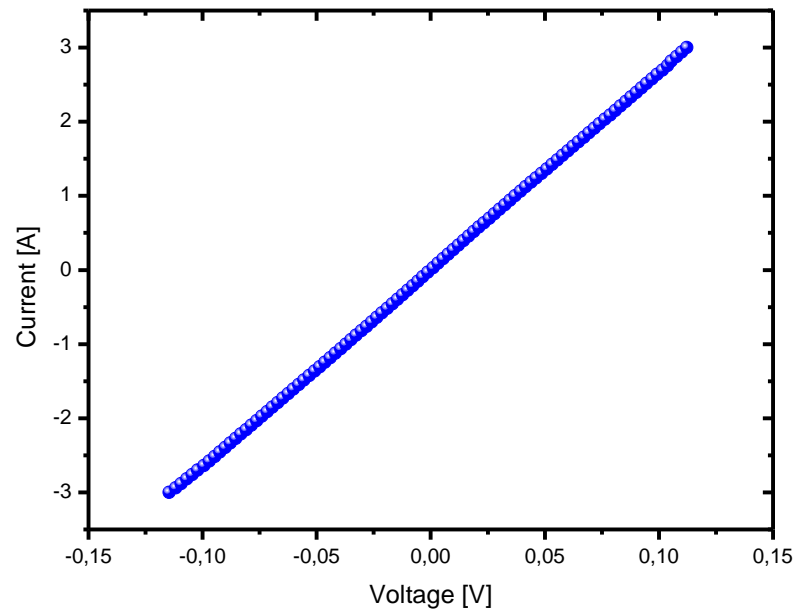


Figure 17: Voltage-current graph of ohmic contact

After calculating the resistances between each metal contact lines, resistance versus metal contact distance graph is plotted to calculate contact resistance (see as an example Figure 18). The linear regression applied to the points is of the form [31]:

$$y = ax + b \quad (\text{Eq.15})$$

In Equation 15, **y** corresponds to resistance values, **a** and **b** values are constants and **x** corresponds to the separation of the metal contact line. To calculate the metal contact resistance, **x** value in the equation is set to zero and then **y** value becomes twice the metal contact resistance value due to the coupling measurement [31].

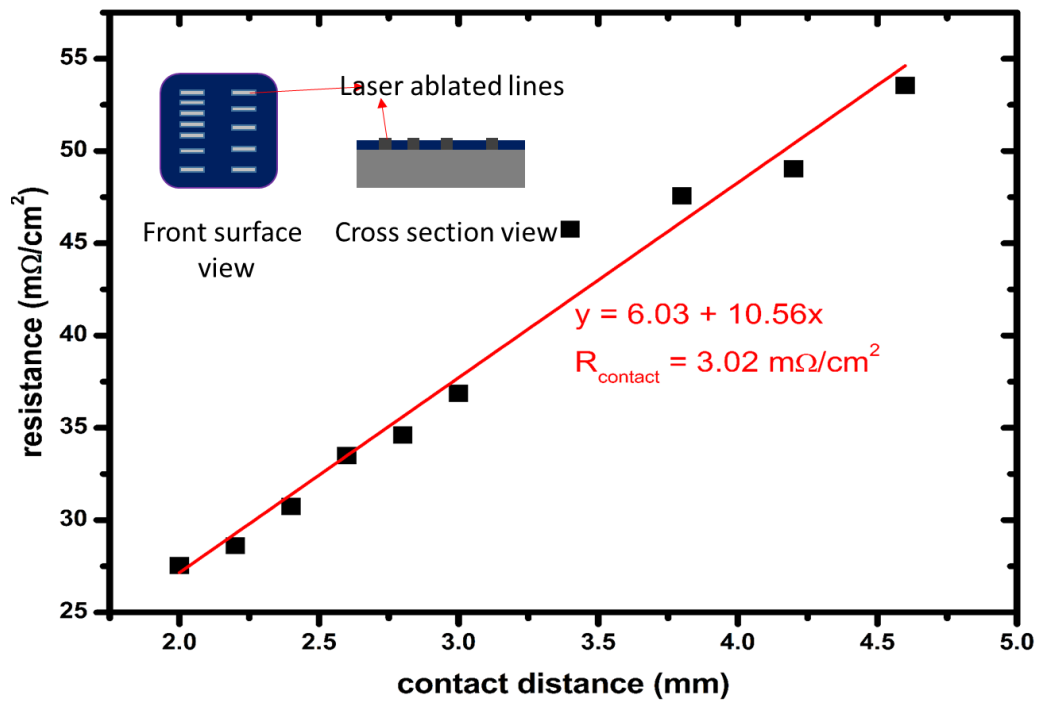


Figure 18: Resistance vs distance graph of TLM sample

Figure 18 depicts one of the results of contact resistance calculation. For the solar cell after front surface metallization process was done. Vertical and thicker white lines (metal contacts) show the busbars, whereas thinner and horizontal white lines show the fingers as in Figure 19. The contact resistance for this cell is calculated to be 3.02 mΩ/cm².



Figure 19: Front surface metallization design

CHAPTER 3

PASSIVATED EMITTER REAR CONTACT (PERC) SOLAR CELLS

3.1 Structure of PERC Solar Cell

PERC solar cells are very promising among next generation solar cells due to their high efficiencies and low costs. PERC solar cell structure was firstly presented by Blakers group in 1989 [32]. PERC solar cell structures have been developing since the invention of PERC structure. The first main advantage of PERC cell is highly reduced rear side surface recombination due to low as recombination velocity and high as internal reflection on the dielectrically passivated rear [33]. The second main advantage is to reduce the silicon consumption due to optical confinement of the cell structure [34]. Recombination tendency of photo-generated electrons in standard solar cells limits the efficiency percentage. PERC design of silicon solar cell result in high efficiencies due to reduced carrier recombination at the metal semiconductor contact interfaces [35].

Basic structure of PERC cells is composed of front contact fingers, anti-reflection coating, front passivation layer, n or p-type silicon base, rear dielectric layer, rear metal contact layer from top to bottom, as can be seen in Figure 20, which shows a standard and PERC cell structure.

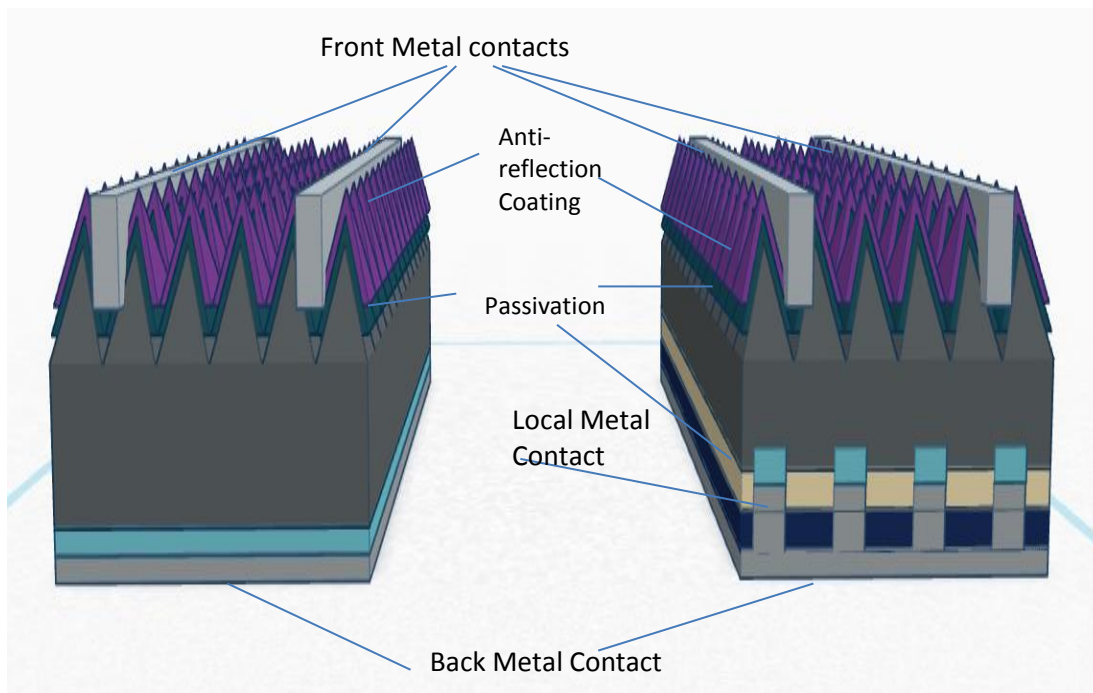


Figure 20: Standard and PERC solar cell structure

3.2 Working Principles of PERC Solar Cell

PERC solar cell's working principle is very close to standard photovoltaic solar cell working principle. However, PERC cells have some benefits due to its design difference. The most important difference of PERC cell design is local back surface field contacts and passivation layer which both can be seen in Figure 20. Backside of a PERC cell is coated with dielectric layer with laser opening holes that decrease the recombination thus increases the overall efficiency. If an electron is generated near the rear side of the conventional solar cell, it is recombined by back surface metallization layer and it doesn't contribute to the overall cell current. However, the dielectric layer of PERC solar cells restrains the electron-aluminium metallization layer attraction. Hence, most of the electrons do reach the depletion region and contribute to the current. Every step of production should be investigated in detail and should be optimized to produce high efficiency PERC cell structure such as the quality of the used silicon material, low contact resistance, proper dielectric layer etc.

3.3 Literature Review of PERC Solar Cells

This section of the thesis is aimed to investigate best efficiency PERC cells produced all over the world. Many solar cell researchers at universities and manufacturers are trying to investigate the PERC solar cell structure with higher efficiencies.

Solar Photovoltaic Laboratory ISFH (Australia) fabricated the first PERC cell structure with 22.8% efficiency on 4 cm² area, p-type, 0.2 Ω.cm resistivity, cell produced by float zone technique Si substrate. Fabricated cell design can be seen in Figure 21. Open circuit voltage was measured to be 696 mV, short circuit current density 40.3mA/cm² and fill factor 81.4%. Procedure of fabrication starts by formation of inverted pyramids at the top surface. To generate inverted pyramid structure, an oxide pattern was formed at the top surface, by anisotropically etching in dilute KOH solution. Secondly, oxide layer was removed and afterwards a second oxide layer was grown to form metal-silicon contact. Thirdly, oxide regions were exposed to heavy phosphorus diffusion. Then, a window was opened for top surface diffusion and oxide layer was removed. The passivation oxide and anti-reflection coating was grown. The etching of metal-silicon contact stripe regions and rear contact holes were carried out. Then the top contact metals of titanium and lead and rear Aluminium contact were evaporated. Finally, front surface metal contact was sintered [32].

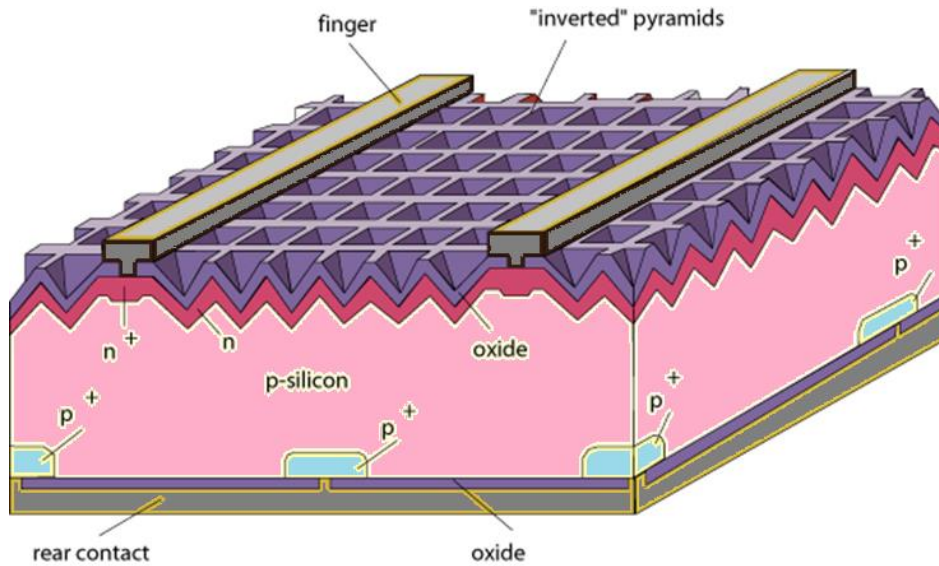


Figure 21: Schematic diagram of PERC cell fabricated by Blakers Group, adopted from [34]

ISFH group published five researches on PERC cell production. Their first paper reports fabrication of 21.7% efficiency, 673 mV open circuit voltage, 40,3 mA/cm² short circuit current PERC cell on 100-oriented, boron doped float zone silicon wafers with initial thickness of 300 μm . They started the process with KOH damage etching. After that they processed standard RCA cleaning process. Next step was 100 nm thick silicon nitrite deposition for diffusion barrier with PECVD. Then, window opening process was done with frequency doubled Nd:YVO₄ laser. After window opening, front side random pyramid texturing was processed in a KOH-IPA solution. An n⁺-emitter diffusion from POCl₃ source was processed in a quartz furnace. After that, PSG removal from front surface and SiN_x from back surface of the wafer was done in HF solution. Next step is the passivation of rear surface with 30 nm thick atomic layer deposition (ALD) aluminium oxide layer in ALD reactor at 200° C. Subsequently, annealing of cells in nitrogen atmosphere was processed at 425° C for 15 min. Next, 100 nm thick silicon nitrate capping layer was deposited. Laser opening of aluminium oxide and silicon nitrate stack at rear side of the cell was processed with geometry of 2.1 mm pitch-square points by picosecond laser. Then, RCA cleaning was again processed and wafers were again dipped into HF. 10 μm thick aluminium layer was deposited with e-beam evaporation on back surface of the cell. Tunnelling layer was formed by atomic layer deposited AlO_x. 10 nm thick

double layer of SiN_x anti-reflection coating was deposited on front side of the wafer. Finally, Aluminium grid evaporation was processed with electron-beam evaporation method [36].

ISFH group second research on PERC cells has maximum efficiency of 20.7%. Their research includes effect of different cleaning processes such as pSC1-HF/HCL, pSC1-HF/HCl-HFO₃, HF/O₃ and PSG-etch for $\text{AlO}_x/\text{SiN}_y$ passivation with comparing the results of RCA cleaning process on test wafers, which are 1.5 $\Omega\cdot\text{cm}$ float zone p-type wafers. On test wafers they researched effective carrier life-time effects of cleaning procedures. Results indicated that HF/O₃ terminated cleaning sequences as pSC1, HF-HCl, HF-O₃ or HF/O₃ prior to $\text{Al}_2\text{O}_3/\text{SiN}_x$ passivation result in effective lifetimes greater than 1 ms, emitter saturation currents of 80-140fA/cm² and corresponding surface recombination velocities 15 cm/s. Moreover, they used two different production methods for controlled test of PERC cell fabrication. Their procedure difference is protection of rear surface for texturing and extra polishing step. PERC solar cells applying the test wafer trial cleaning sequences show effective surface recombination velocities less than 50 cm/s. PERC cell fabricated, can be seen in Figure 22, with cleaning procedures of pSC1, HF-HCl indicated 19.4% efficiency whereas cells fabricated with pSC1,HF-O₃ cleaning resulted in 20.4% efficiency. Nevertheless, the best efficiency was obtained from the fabrication method with RCA cleaning procedure before rear passivation [37].

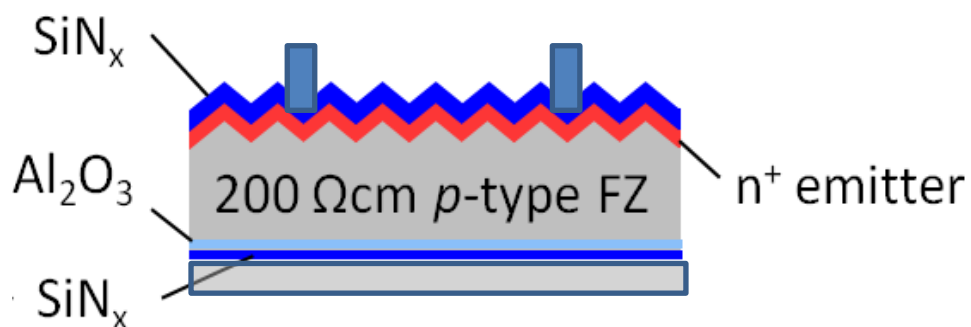


Figure 22: Fabricated PERC cell design of ISFH Group, adopted from [36]

ISFH group third research indicates 19.7% efficiency on 300 μ m thick boron doped p-type float zone wafers. The procedure is quite similar to above mentioned research. They researched the rear surface roughness effect on efficiency. The highest efficiency as 19.7% result was obtained from polishing removal of 7.5 μ m of pyramid texture on rear surface [38].

Another ISFH group design of PERC cell, indicates 20.6% efficiency on 100-oriented boron doped float zone p-type crystalline wafer with 300 μ m thickness and 0.5 Ω .cm resistivity. They started the fabrication with wet chemical cleaning. Secondly, silicon-oxide layer was grown on both surfaces with a wet oxidation procedure. Then, 2x2 cm² diffusion windows were opened photo-lithographically. Random pyramid texturing was processed through the windows with KOH-IPA solution. Phosphorus n+-emitter was diffused from POCl₃ source. Next, PGS was removed by dipping in HF solution. At this point, fabrication was separated into three branches as can be seen in Figure 23. The best efficiency trial is the most left line of the procedure in the process flow figure with 20.6% efficiency and 659 mV open circuit voltage values [39].

Finally ISFH research Group investigated the analysis of the bulk and rear recombination of screen printed PERC type solar cells. Different dielectric surface passivation layers with silicon-oxide, aluminium-oxide and silicon-nitrate were processed on p-type Czochralski silicon wafers. Wafers were cleaned in a RCA solution. 10 nm thick silicon oxide layer on both surfaces was deposited by dry thermal oxidation. Afterwards they processed silicon nitrate layers by PECVD. On rear surface, the SiO₂-SiN_x passivation stacks are locally ablated by a 532 nm laser with pulse lengths of 10 picoseconds. They examined the metallisation fraction at the rear surface. The best efficiency was obtained from application of Al₂O₃-SiN_x layer stack among all other rear passivation layers. Different rear passivation layer fabrication results can be seen in Table 1. They demonstrated an optimized optical and surface passivation performance of Al₂O₃/SiN_x layers at the rear side of fully screen-printed PERC solar cells with homogeneous phosphorus-doped front side emitter. With the excellent rear passivation layer, they resulted in 0.8 absolute increase in efficiency [40].

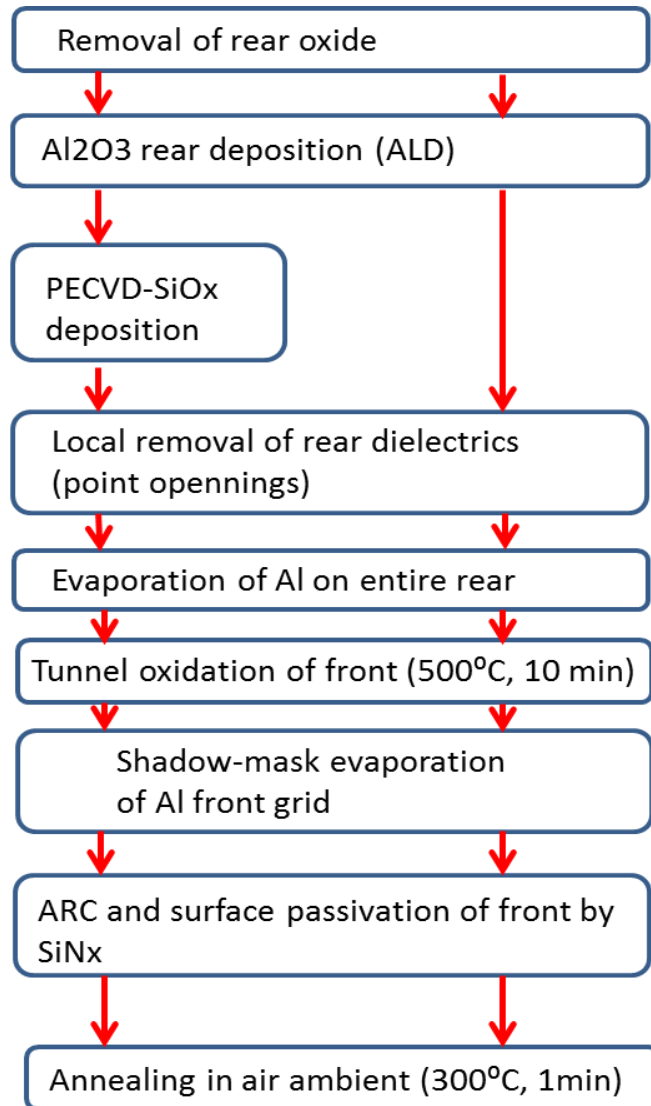


Figure 23: Process details after HF dip [39]

Table 1: Different rear passivation results [40]

Rear Passivation	Area [cm ²]	Dopant	Voc[mV]	Jsc[mA/cm ²]	FF[%]	Efficiency[%]
SiO ₂ /SiN _x	233	Boron	652	38.3	77.2	19.3
Al ₂ O ₃ /SiN _x	149	Boron	646	39.0	77.2	19.5
SiN _x	149	Boron	642	38.3	77.4	19.1
Al-BSF	147	Boron	632	37.1	79.8	18.7
SiO ₂ /SiN _x	233	Gallium	657	37.6	77.3	19.1

School of Photovoltaic and Renewable Energy Engineering fabricated 20.5 % efficiency PERC cell on 2 Ω .cm boron doped 156 mm x 156 mm area Czochralski silicon wafers [41]. They investigated laser doped selective emitter onto the industrialized PERC cell. Their fabrication procedure started with single side removal of saw damage etching by KOH alkaline solution. Wafers were resulted in thickness of 180 μ m after pyramid texturing. Standard chemical cleaning was next performed. Then, phosphorus diffusion and PSG removal took place. Rear side emitter was chemically removed. Subsequently, 15 nm thick silicon-oxide layer was grown. Anti-reflection coating on the front surface was deposited. Silicon oxide-silicon nitrate stack on the rear surface was done by PECVD. Sheet resistance of emitter was measured as 100 Ω /sq after thermal oxidation. Laser doping was performed by 355 nm wavelength laser with a power density of approximately 2.6 mW/cm². Sheet resistance boxes were ablated prior to HF dip and then, laser ablation was carried out for front surface. Front surface laser contact opening resulted in an opened line width of 12 μ m and process speed was 0.8 m/sec. Next, rear surface laser ablation procedure was done prior to firing and aluminium deposition of all rear surfaces. Ni-Cu-Ag plating and sintering was the final step of the fabrication.

Imec Group reported 20.1 % efficiency record on p-type Cz-Si 1.5 Ω -cm wafers [42]. Rear side polishing of monocrystalline perc solar cell is studied in their research. The effect of polishing was investigated by contact formation, light trapping and surface recombination measurements. They started their production of PERC cell with two sided random pyramid texturing on p-type silicon wafer. The process is continued with single side etching by HF/HNO₃ solution having an etch rate of 2 $\mu\text{m/s}$. They removed porous silicon with KOH solution after polishing process. The process was continued with anti-reflection coatings for back and front sides with PEVCD. For rear side and front side SiN_x and SiO₂ was deposited. Then laser ablation of dielectric layer was performed. Al sputtering, single Ag screen printing and finally co-firing processes are the last 3 steps. Their first conclusion is that entirely smooth rear side decreases the efficiency of the cell. Their results, shown in Table 2, indicates that 5-6 μm pyramid smoothening has the best effect on cell performance for 8-10 μm pyramid based textured wafers. In other words, roughness of 200-500 nm range is more efficient for light trapping and contact formation whereas a perfectly flat rear surface is more effective for surface recombination.

Solar Energy Development Group of Samsung published PERC cell efficiency of 19.4 % fabricated on 6 inch, boron doped, p-type Czochralski wafer [43]. They investigated the usage of nanosecond and picosecond pulse width of green laser having both 532 nm wavelength for the laser ablation process. Electron Probe Micro analyser method, quasi-steady state photo conductance measurements and transmission electron microscopy were used to analyse the laser ablation process in this research. Usage of picosecond green laser was observed to cause almost negligible damage on the surface. Local contact depth of PERC cell was about 10-17 μm . The maximum damage of the used lasers in this research is 2.5 μm which is shallower than local contact depth. PERC solar cells having maximum efficiency of 19.4% were fabricated with both ns and ps pulse lasers. The laser ablation process was aimed to remove the SiN_x and Al₂O₃ layers.

Table 2: Efficiency results of pyramid smoothing thicknesses, adopted from [42]

Si etch [μm]		Jsc [mA/cm^2]	Voc [mV]	FF [%]	Efficiency[%]
0	Average	37.99	650	78.8	19.5
	Best Result	38.04	651	79.3	19.6
3	Average	38.34	652	79.2	19.8
	Best Result	38.41	654	79.6	19.9
6	Average	38.38	651	79.7	19.9
	Best Result	38.52	653	80.1	20.1
10	Average	38.25	646	78.6	19.4
	Best Result	38.48	649	79.1	19.7

Suntech Power Holdings Group investigated the rear passivation of multicrystalline commercial PERC solar cells [44]. They has reported 18,63 % efficiency of PERC cell design on $156 \times 156 \text{ mm}^2$ large, 200 μm -thick, 2 $\Omega\cdot\text{cm}$ resistance, p-type, and boron-doped multicrystalline Si wafers. They started the fabrication with front side pyramid texturing. They continued with an industrialization etching process including HF/HCl cleaning before Al_2O_3 deposition. Next, aluminium oxide layer deposition on rear side processed with PECVD system. Then they deposited silicon nitrite on both sides of the cell. On rear side, the $\text{Al}_2\text{O}_3/\text{SiN}_x$ stack was locally ablated by a coherent laser having 355 nm wavelength with the pitch and width of lines 1 mm and 18 μm . Rear side metal contact was formed by screen printing. The front electrode was finally sintered with Ni/Cu/Ag by electroplating. They achieved

18.63% efficiency with screen-printed contacts. An effective surface recombination velocity at the rear of 260 cm/s was achieved with a line pitch of 1 mm.

CHAPTER 4

EXPERIMENTAL PROCEDURES

4.1 PERC Solar Cell Fabrication Procedure

In this chapter, production procedures used in this thesis are discussed. In Figure 24, process steps of this thesis work are summarized.

Solar wafers of resistivity 0.5-3 Ω .cm and thickness 180 μ m were used in this thesis study. PERC solar cell process started with production of random pyramid texturing with alkaline KOH solution. Standard RCA cleaning procedure and dilute-HF dip took place following texturing. After dilute HF-dip, cells were exposed to phosphorus diffusion to form n emitter region on both sides of wafer. Then, front side of the solar cell is coated with a thick silicon nitrite masking layer to protect front surface in rear side polishing process. After rear side-polishing with concentrated KOH solution, wafers were kept inside the HF solution to remove nitrite layer from the front side of the wafer. Then standard RCA cleaning procedure was applied [45]. Wafers were then dipped to dilute-HF solution to remove oxide layer prior to dielectric layer formation. After dielectric layer formation, back and front side of the wafer are coated with SiNx to form anti-reflection layers. After anti-reflection coating, rear side of the cell was ablated with 1064 nm pulsed laser to form local back contact openings on rear side. In this thesis work, EO Technics Super Mark GF pulsed (nanosecond) laser having 1064 nm wavelength, 200 ns pulsed width, 4.5 kWatt peak power for 30kHz and 30 μ m focal spot size was used. Laser parameters of having 100% power (27.5 Watt), 5493 mm/sec velocity and 25% power (4.75 Watt), 586mm/sec velocity were chosen for the laser ablation. Then, rear side of the cell was coated with aluminium by thermal e-beam evaporator. After

aluminium coating process, cells were fired at 800°C for 40 minutes to confine metal diffusion through laser ablated windows. To have accurate thick back metal contact, aluminium evaporation was applied again on the rear side. Finally, screen printing method was used to form front metal contact.

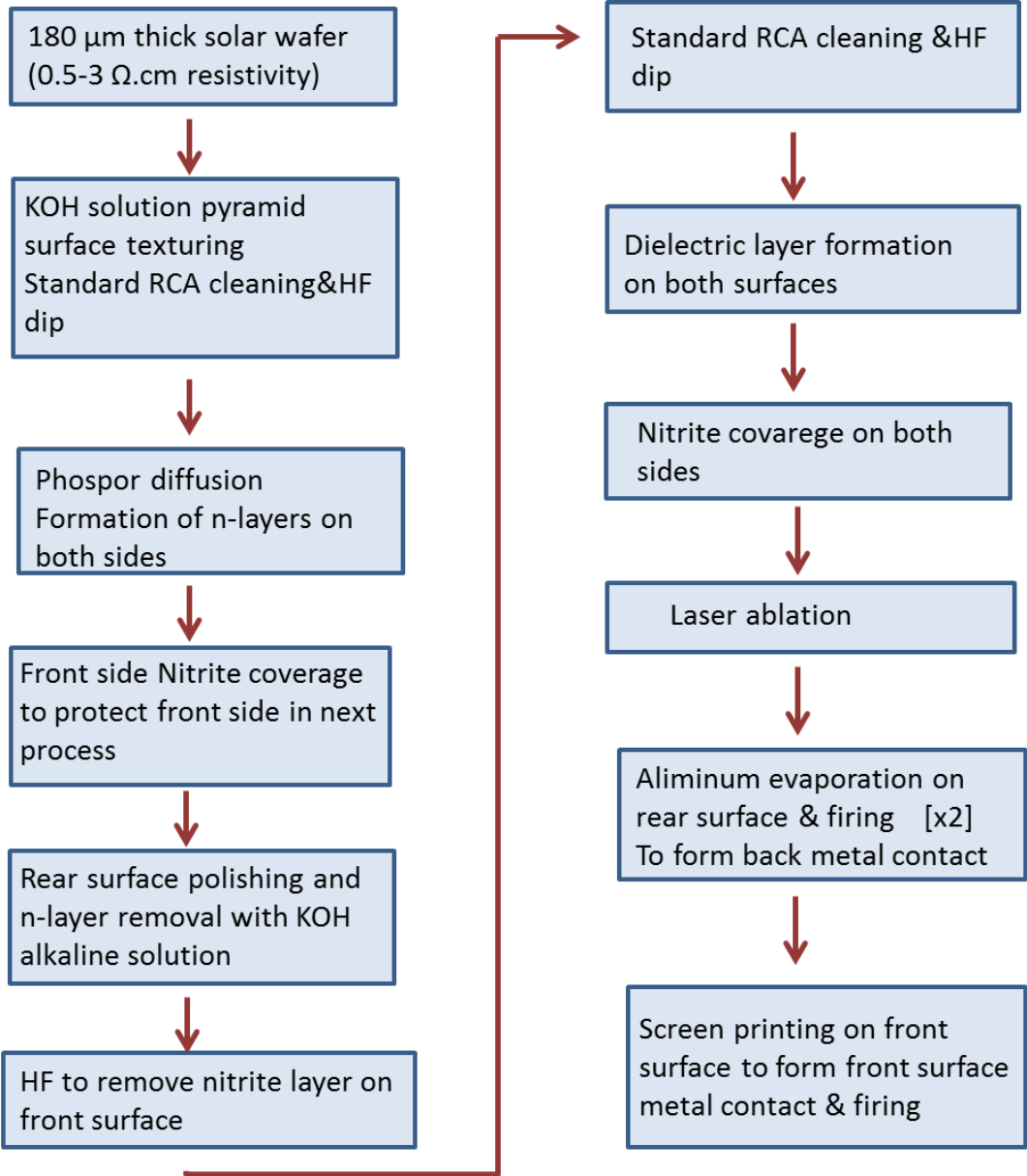


Figure 24: Process flow of PERC cell in this thesis work

4.1.1 Single side etching

PERC solar cells were produced as pyramid textured front surface (Figure 25) and planar rear surface to capture light in the cell. Random pyramid texturing with alkaline KOH solution was the first step of PERC production. To polish rear side of the pyramid textured cell, HNA (HF-HNO₃-CH₃COOH) acidic solution, HF-HNO₃ solution in different percentages and KOH-IPA alkaline solution were utilized.

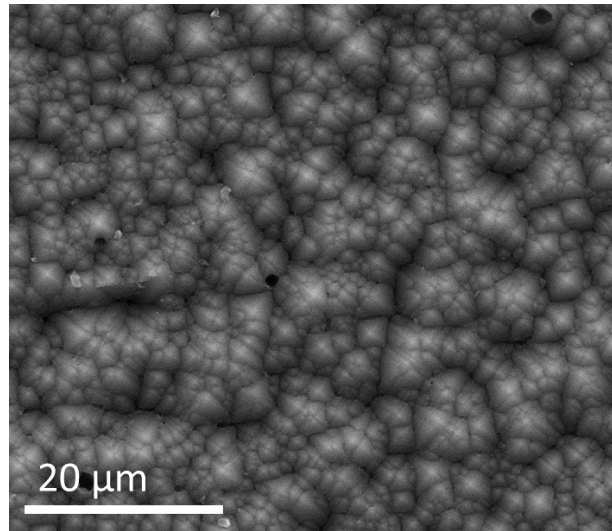


Figure 25: SEM picture of pyramid textured surface

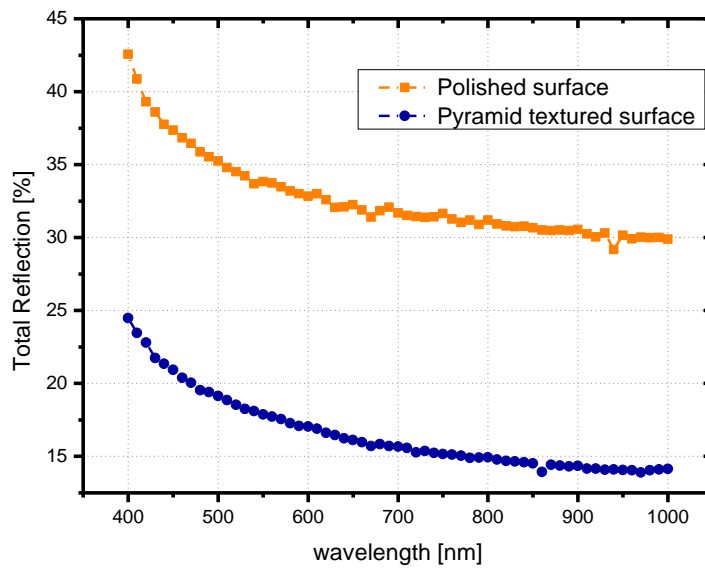


Figure 26: Total reflection graph of polished and pyramid textured wafer

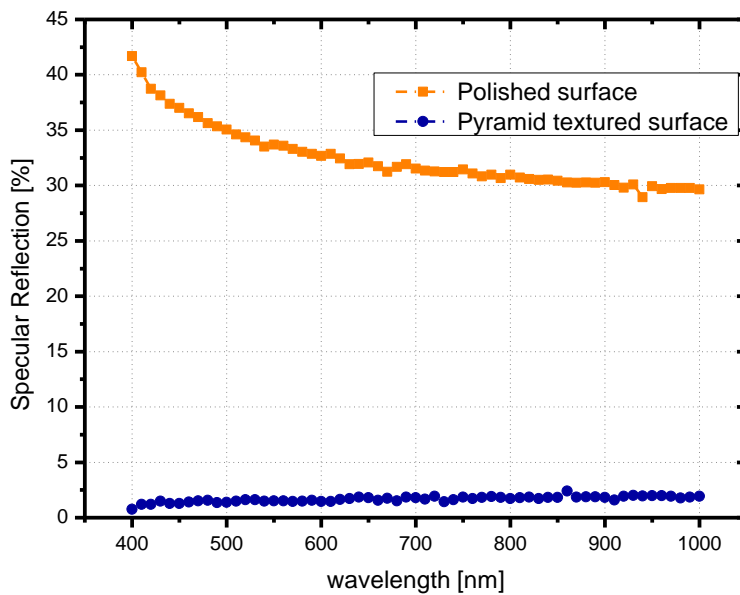


Figure 27: Specular reflection graph of polished and pyramid textured wafer

Total reflection and diffuse (specular) reflection measurements were used to measure the roughness of the etched surfaces. Polished wafer reflects the incoming light, whereas pyramid textured wafer captures the incoming light. Hence, total reflection percentage of polished wafer changes between 32%-44%, whereas pyramid textured wafer reflection percentage changes between 14%-25% (Figure 26 & 27). Specular reflection measurement was a method to measure mirror-like reflection percentage of a surface. Hence specular and total reflection percentages of polished surfaces were nearly equal (Figure 26 & 27 and 28). However, pyramid textured surfaces do not reflect incoming light directly. Hence, specular reflection percentage of pyramid textured surface was very low (Figure 27). Total and specular reflection measurements are used in order to be sure about the reflectivity of surfaces. To support these measurements 4 point probe measurements were conducted. Before polishing process, both sides of the wafer were doped to form n-type region. Back side of the PERC cell should not have n-type layer to have good electric field. Hence, 4 point probe measurement of rear side layer type after polishing process was processed to be sure about also n-layer removal of etching.

KOH solution was chosen to be the polishing agent due to two reasons. First reason was protecting the front surface from etching. With HNA solution etching, it is not easy to protect front side of the wafers since HNA solution is very strong acidic solution. Single side etching tools should be used to protect other side which is not available in GÜNAM labs. With KOH solution we used nitrite coating to protect front side of the cell. Second reason is the etch rate of the HNA and HF-HNO₃ solution which is really high and hard to control. Hence, KOH alkaline solution was processed to produce PERC cell in this thesis work.

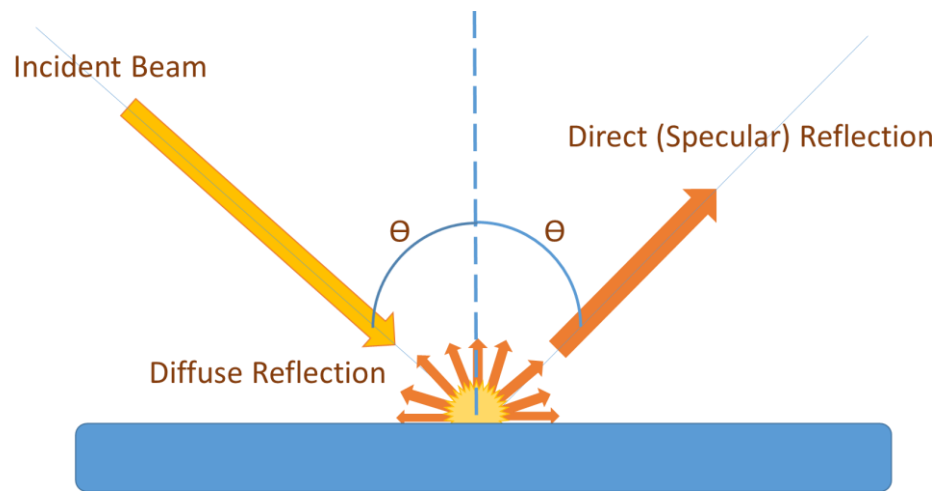


Figure 28: Specular and Diffuse Reflection

4.1.2 Backside passivation

Backside passivation of PERC cell design was done with the standard back side passivation procedure previously optimized by GÜNAM researchers.

Backside passivation process was aimed to saturate the unsaturated bonds of crystal lattice [46]. With the saturation procedure, rear surface recombination velocity of the electron-hole pairs decreased. To saturate the backside of the cell SiO₂ and SiN_x layers were formed on the backside of the cell.

Passivation process started with SiO₂ formation in oxidation furnace on the rear side of the cell after short HF-dip at 800°C. Secondly, SiN_x layer was formed on the SiO₂ layer in PECVD at 400°C. These SiO₂ and SiN_x layers formed on the rear side of the

cell will be called as dielectric layer. Dielectric layer on the rear surface decreased the rear surface recombination velocity by passivating the unsaturated silicon bonds of the rear surface.

Passivation quality of the cell was determined with life-time measurements. Life-time measurements were carried out before annealing step of production, after annealing and after firing. Annealing and firing steps of PERC cell production are processed at high temperatures. Dielectric layers might be damaged by exposing high temperature. Therefore, life-time values were measured before and after annealing and firing processes.

4.1.3 Laser structuring

The main aim of rear surface laser ablation process to back metal contact points was done by ablating small windows above back side dielectric layer without melting the silicon [39]. In this thesis work, EO Technics Super Mark GF pulsed laser having 1064 nm wavelength was used. Laser speed, current and frequency are the three main laser parameters. First step was to analyse the laser parameters which ablated the wafer surface that was coated with SiN, by the optical microscope. Secondly, parameters which did not melt the wafer were chosen to be the parameters of ablation. After laser window opening, aluminium evaporation on the rear side and annealing of aluminium steps were processed. Finally, TLM measurements were used to find the optimal laser parameter to ablate the rear side of the laser.

After optical microscope analysis of laser speed, frequency and power parameters, 30 kHz frequency and laser speed-power interval was chosen to be optimal (Figure 29). Moreover, with the very high laser speeds power of the laser should have been increased to have accurate ablation. With the increase in laser speed, power impact of laser decreases. Since one more parameter at that speed-power area was also chosen as frequency of 30 kHz and velocity of 5493mm/s.

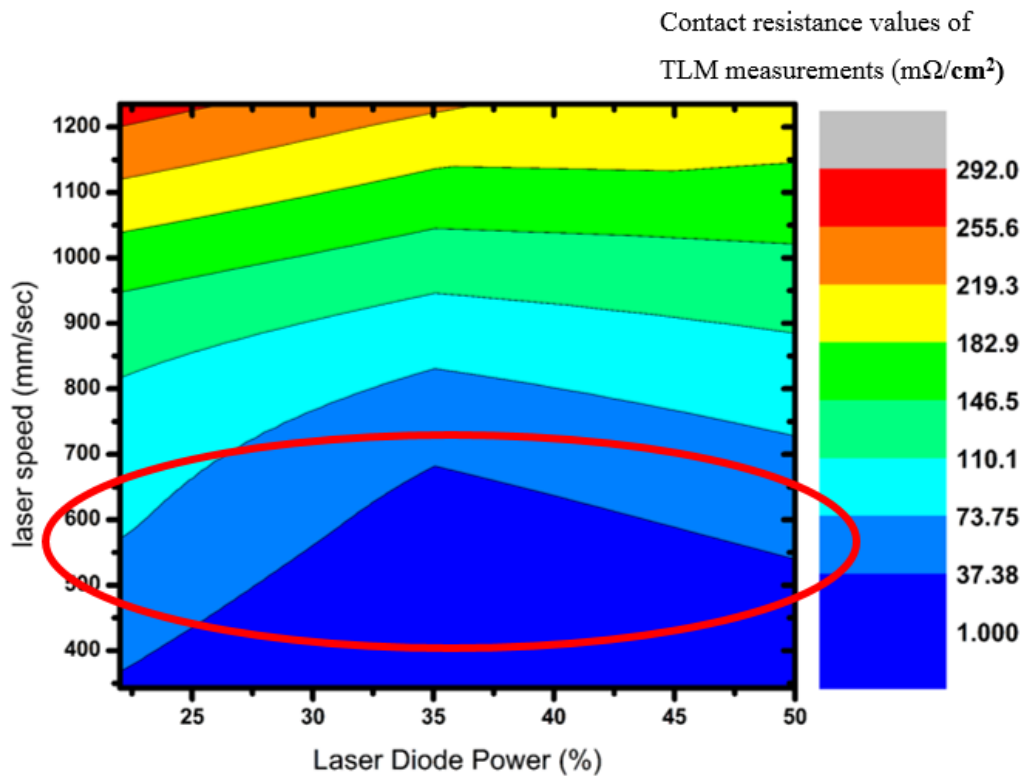


Figure 29: Laser speed-power graph of frequency 30kHz

CHAPTER 5

RESULTS AND DISCUSSION

5.1 Single side etching results

5.1.1 HNA and HF+HNO₃ solution single side etching

In most of the high efficient PERC production procedures, acidic etching solution is preferred to be used for polishing process, since KOH alkaline solution is not as clean production as acidic cleaning [47]. Moreover, solutions work at room temperature for acidic texturing. Hence, we started with acidic HF-HNO₃ solution with changing percentages of solution, changing etching time and adding stirring effect. 300 ml-400 ml HF-HNO₃ was really strong and even enough to vaporize the wafer in 3 seconds. 420 ml-280 ml-100 ml HF-HNO₃-H₂O solution was not strong enough to polish wafer. 420 ml-280 ml-45 ml solution polished the wafer but it also etched the nitrite, so front side of the wafer was not protected. Total and specular reflection percentage graphs after polishing with 420 ml-280 ml-45 ml solutions are shown in Figure 30 and Figure 31. Front surface of wafers that was coated with silicon nitride should be protected from the solution. However, specular reflections of silicon nitride coated surfaces indicate us that front surfaces were also etched.

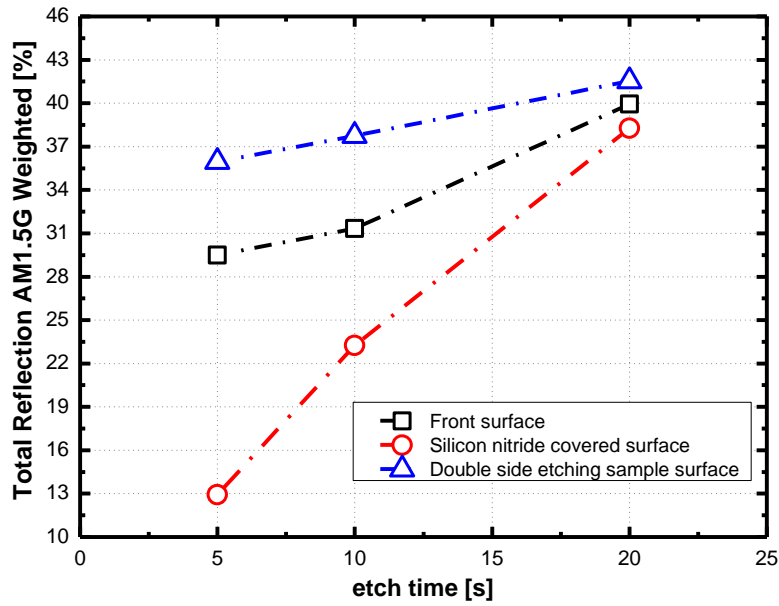


Figure 30: Total reflection AM 1.5 G weighted percentage graph of HF-HNO3-H2O (420 ml-280 ml-45 ml) polishing solution

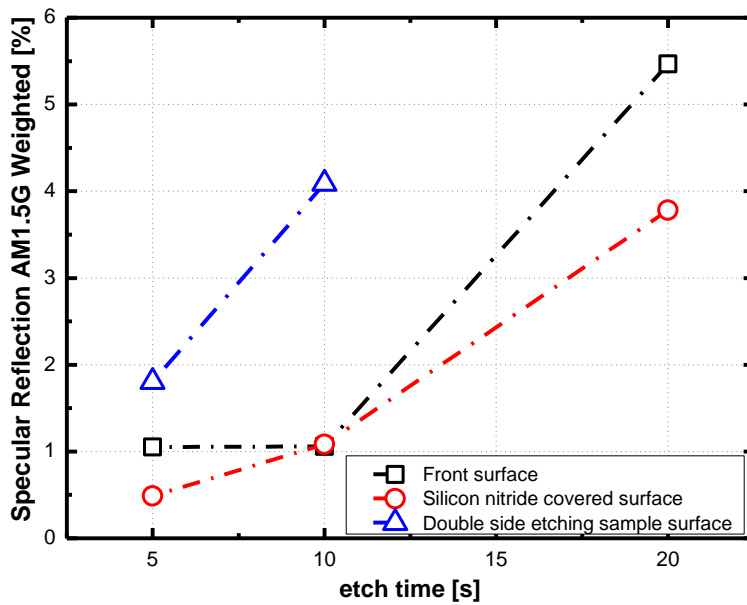


Figure 31: Specular reflection AM 1.5 G weighted percentage graph of HF-HNO3-H2O (420 ml-280 ml-45 ml) polishing solution

HF+HNO₃ (420 ml/280 ml) did properly polish the wafer but also polished the front surface. Total and specular reflection percentage graphs of HF+HNO₃ (420 ml/280 ml) polishing solutions are in Figure 32. 5 s etching of HF+HNO₃ solution was not enough to polish the pyramid textured surface. Since specular reflection of 5 s etching was not high enough (Figure 32). 10 seconds etching time of HF+HNO₃ solution was used to polish the wafer (Figure 32). Optical microscope image of etching 10 s in HF+HNO₃ solution indicates that solution polished the wafer (Figure 33). However, KOH alkaline polishing solution indicates higher percentages of specular reflections, which will be explained in next part. Moreover, HF+HNO₃ polishing solution has an etching rate of 5μm/s, which is very high compared to KOH alkaline polishing solution.

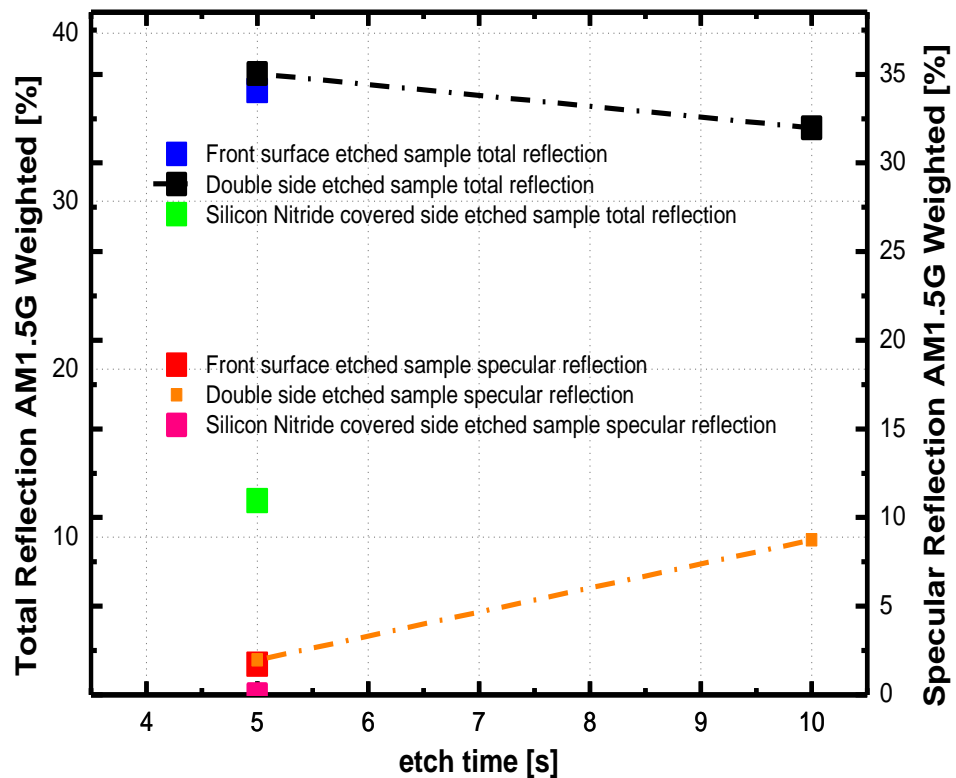


Figure 32: Total and specular reflection AM1.5 G weighted percentage graph of samples treated with HF+HNO₃ (420 ml/280 ml) polishing solution

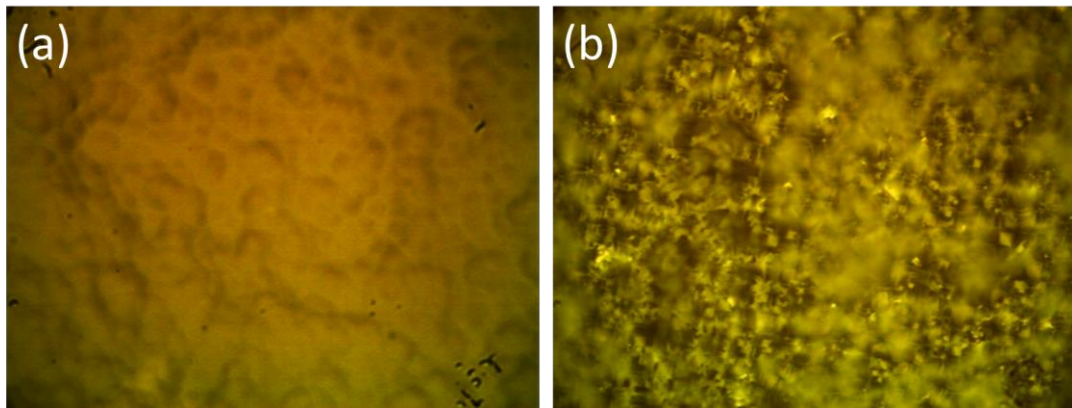


Figure 33: Optical microscope photographs of wafer etched in HF+HNO₃ (420ml/280ml) polishing solution and bare pyramid textured wafer surface (x1500 magnification)

HNA (HF-HNO₃-CH₃COOH) acidic solution is also used to polish the pyramid textured surfaces [48]. HF-HNO₃-CH₃COOH solution with 100 ml-150 ml-300 ml and HF-HNO₃-C₃COOH (60 ml-450 ml-150 ml) solution did not polish the surface properly. The solution HF-HNO₃-C₃COOH 60 ml-450 ml-150 ml polished pyramid textured surfaces with magnetic stirring and with manual pre-stirring in ultrasonic cleaner.

HF-HNO₃-CH₃COOH (100 ml-150 ml-300 ml) etching solution did not polish the surfaces in 25 minutes. Since, specular and total reflection percentages are very low compared to polished surface shown (Figure 34).

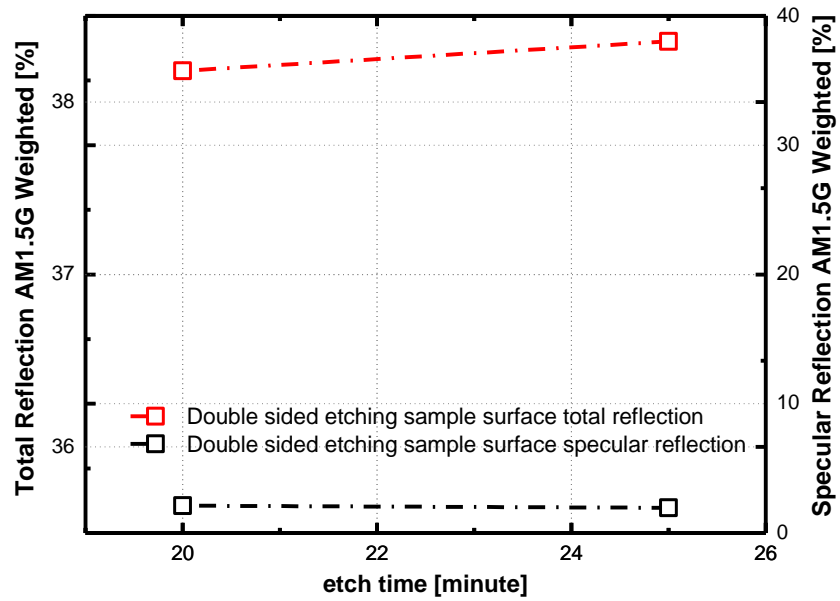


Figure 34: Total and specular reflection AM 1.5G weighted percentage graph of HF-
 $\text{HNO}_3\text{-CH}_3\text{COOH}$ (100 ml-150 ml-300 ml)

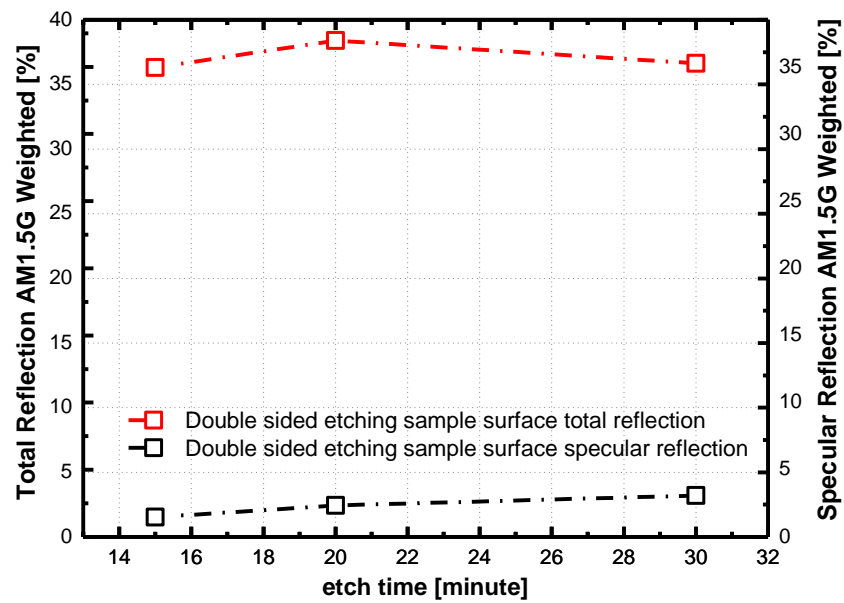


Figure 35: Total and specular reflection AM 1.5G weighted percentage graph of HF-
 $\text{HNO}_3\text{-CH}_3\text{COOH}$ (60 ml-450 ml-150 ml)

HF-HNO₃-C₃COOH (60 ml-450 ml-150 ml) etching solution also did not polish the surfaces. Since, specular and total reflection percentages are very low according to polished surface shown (Figure 35).

HF-HNO₃-C₃COOH (60 ml-450 ml-150 ml) with magnetic stirring polished textured surface. Since specular and total reflection percentages are nearly as high as polished surface values (Figure 36). Etch rate of the solution was 4.85µm/min. 20 minute etching of the solution resulted in polished surface. It can be seen in specular reflection graph and SEM image of the surface (Figure 37).

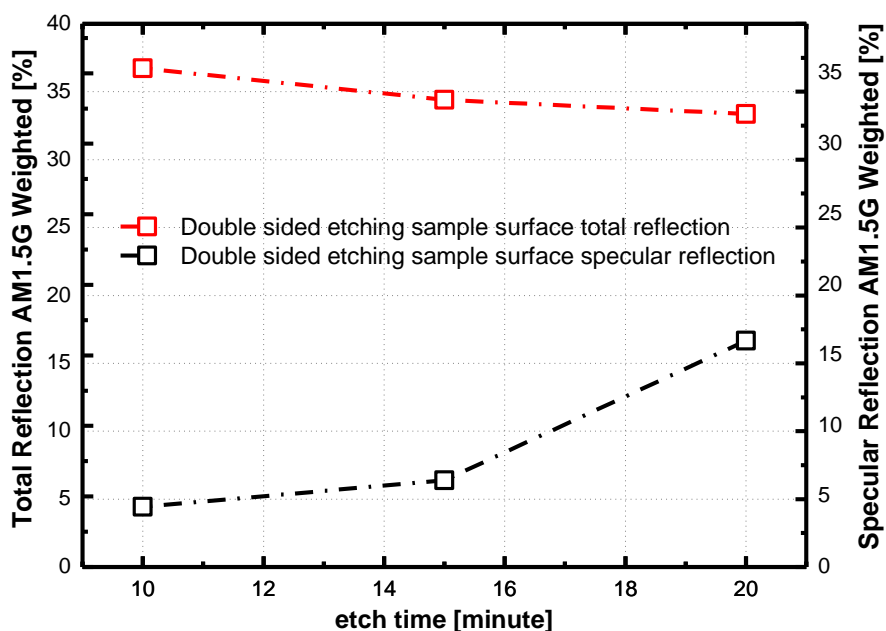


Figure 36: Total and specular reflection AM 1.5G weighted percentage graph of HF-HNO₃-CH₃COOH (60 ml-450 ml-150 ml) with magnetic stirring effect

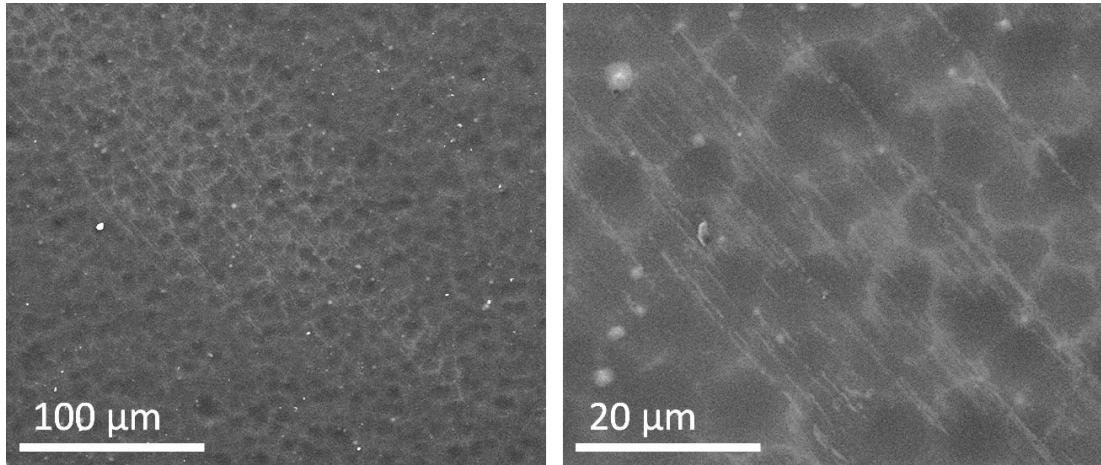


Figure 37: SEM images of surface etched by HF-HNO₃-CH₃COOH (60 ml-450 ml-150 ml) with magnetic stirring for 20 minute

HF-HNO₃-CH₃COOH (60 ml-450 ml-150 ml) solution in ultrasonic cleaner polished the surface since specular and total reflection percentages are nearly as high as polished surface values (Figure 38). Etch rate of the solution was 13 μm/min. 5 minutes etching of the solution polished the surface. It can be seen in specular reflection data and SEM picture of the etched surface (Figure 39).

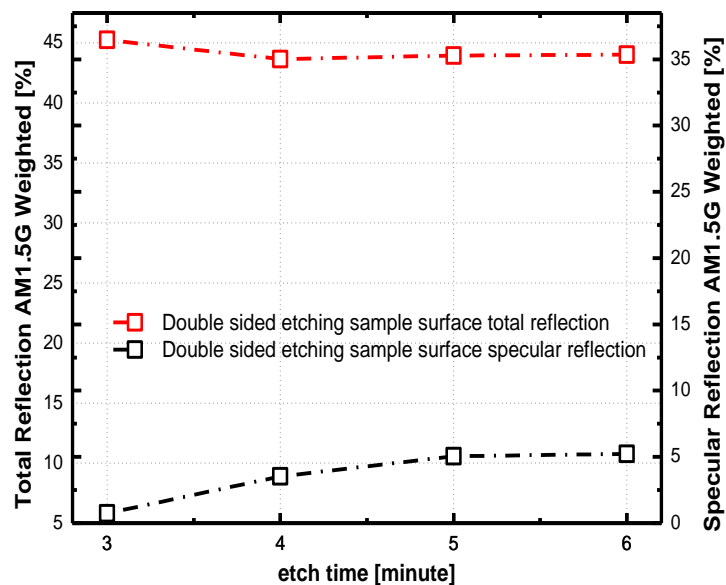


Figure 38: Total and specular reflection AM 1.5G weighted percentage graph of surface etched in HF-HNO₃-CH₃COOH (60 ml-450 ml-150 ml) solution in ultrasonic cleaner manually stirred with previous magnetic stirring effect

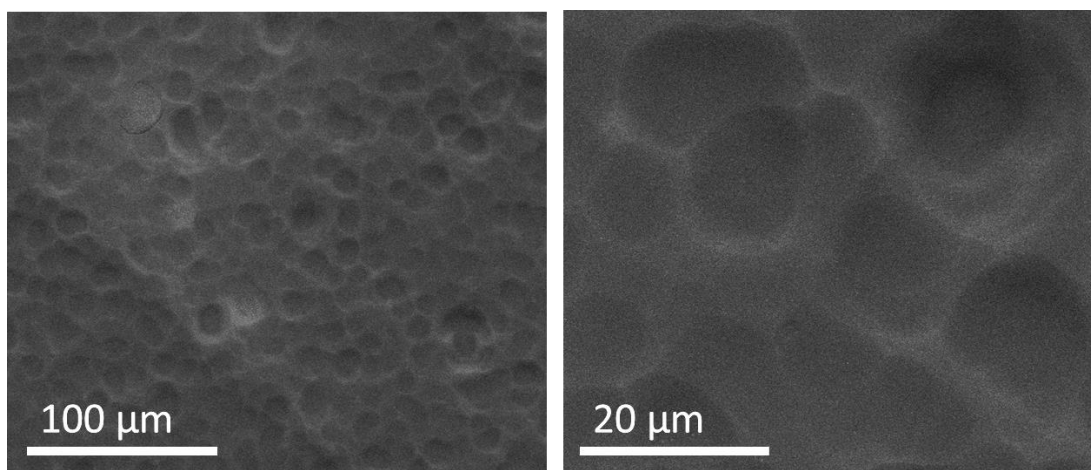


Figure 39: SEM pictures of surface etched by HF-HNO₃-CH₃COOH (60 ml-450 ml-150 ml) solution in ultrasonic cleaner manually stirred with previous magnetic stirring effect

HNA and HF-HNO₃ acidic solution polishing methods were perfect solutions to polish pyramid textured surfaces, however front surface protection was a huge problem. Hence, KOH alkaline solution method was next solution the polish back surface.

5.1.2 KOH-H₂O₂ alkaline solution single side etching

KOH alkaline solution can be also used for polishing of textured surface [49]. We first started with KOH-H₂O (40%-60%) solution. However, it did not polish textured surface properly. Secondly, KOH-H₂O₂-H₂O (40%-20%-40%) solution was processed [50]. This solution polished the wafer but not in room temperature. We also tried etching process of the solution at room temperature but it didn't work. KOH-H₂O₂-H₂O (40%-20%-40%) etching solution works at 80°C. Specular and total reflection percentages of etched surface graphs indicate that 480 s and 900 s etching polished the pyramid textured surfaces (Figure 40). However 900 s of etching time also etched the nitrate covered surface. Since specular reflection and total reflection percentage values of etched surface and nitrate surface indicates nearly same high values (Figure 41). Moreover, optical microscope images of front and back surface of etching indicates us that 480 s of etching is the optimal time (Figure 42).

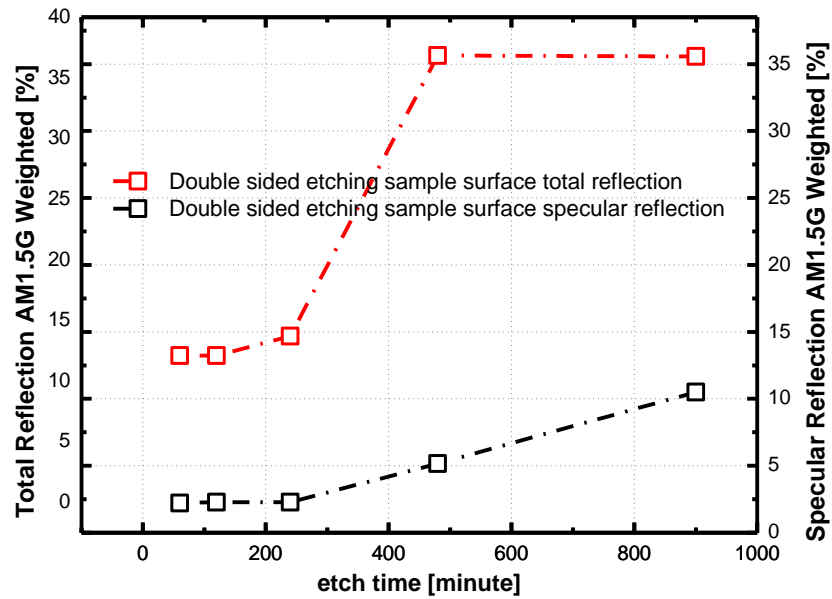


Figure 40: Total reflection AM 1.5G weighted percentage graph of etched surfaces in KOH-H₂O₂-H₂O (40%-20%-40%) solution

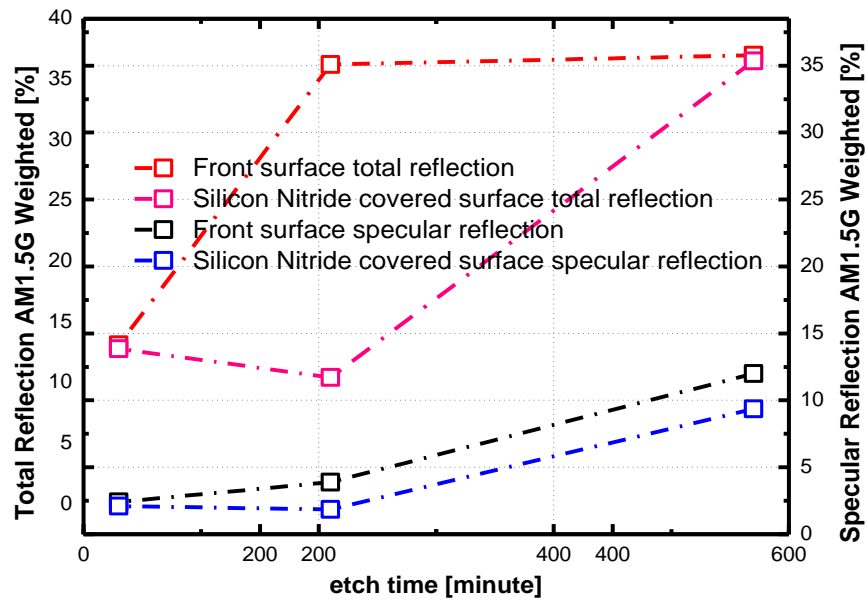


Figure 41: Total reflection AM 1.5G weighted percentage graph of etched and silicon nitride covered surfaces in KOH-H₂O₂-H₂O (40%-20%-40%) solution

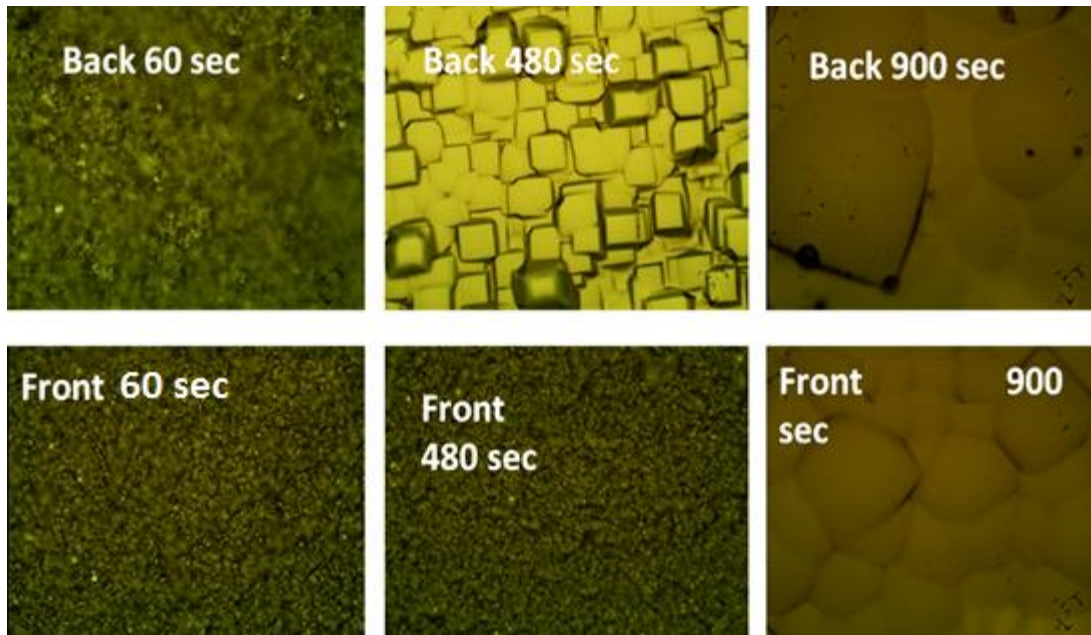


Figure 42: Optical microscope images of bare and silicon nitride covered surfaces in KOH-H₂O₂-H₂O (40%-20%-40%) solution with respect to time [All images are at 1500x magnification]

Finally, KOH-H₂O₂-H₂O (40%-10%-60%) solution was processed. This solution polished wafer better than KOH-H₂O₂-H₂O (40%-20%-40%) solution. Etching time of 240 s, 480 s and 900 s polished the surfaces. Since, total reflection percentages and specular reflection percentages indicated nearly high values as polished surface total and specular reflection percentages (Figure 43). Moreover, optical images of etched surfaces also indicated the same results (Figure 45). However, 900 s of etching resulted in etching of nitrate surface and front surface and resulted in 135 μm thick wafer. 480 and 240 s of etching total and specular reflection percentages were close but 480 s of etching was better. SEM image of the 480 s etched surface is shown in Figure 46 and indicates polished surface. Hence, 480 s etching of KOH-H₂O₂-H₂O (40%-10%-60%) solution was the chosen optimal etching process. Moreover, etching time of the solution was changing due to etching time (Figure 44). Hence, before starting the process we dropped pieces of wafer to balance the etching rate before the process and solved the problem of changing rate. Moreover, rear side n-layer was also etched with the KOH polishing process can be seen in the sheet resistance measurement graph in Figure 47.

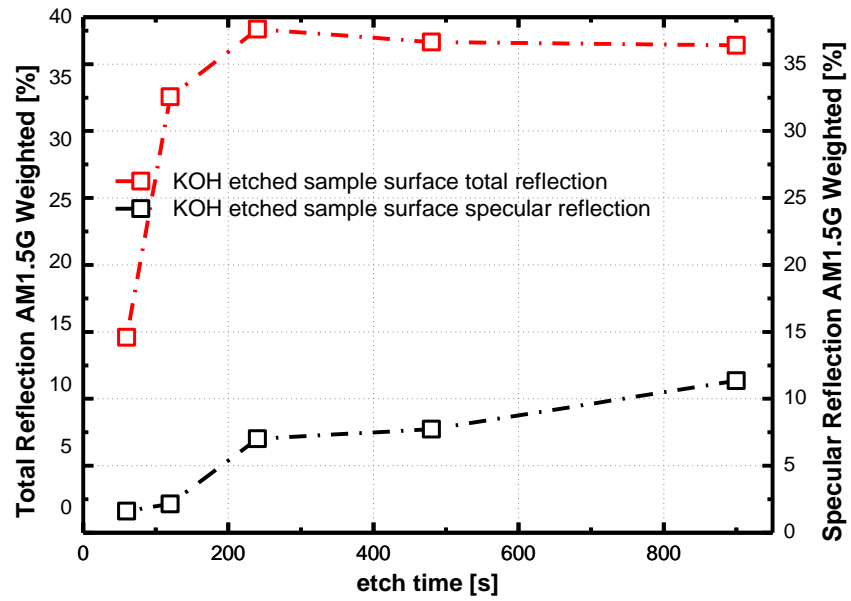


Figure 43: Total reflection AM1.5G weighted percentage graph of etched surfaces in KOH-H₂O₂-H₂O (40%-10%-40%) solution

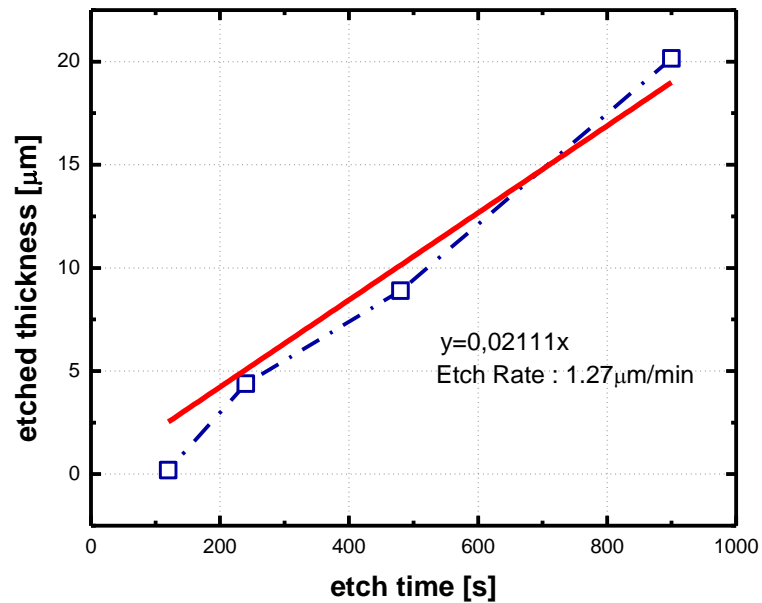


Figure 44: Etch rate of KOH-H₂O₂-H₂O (40%-10%-40%) solution

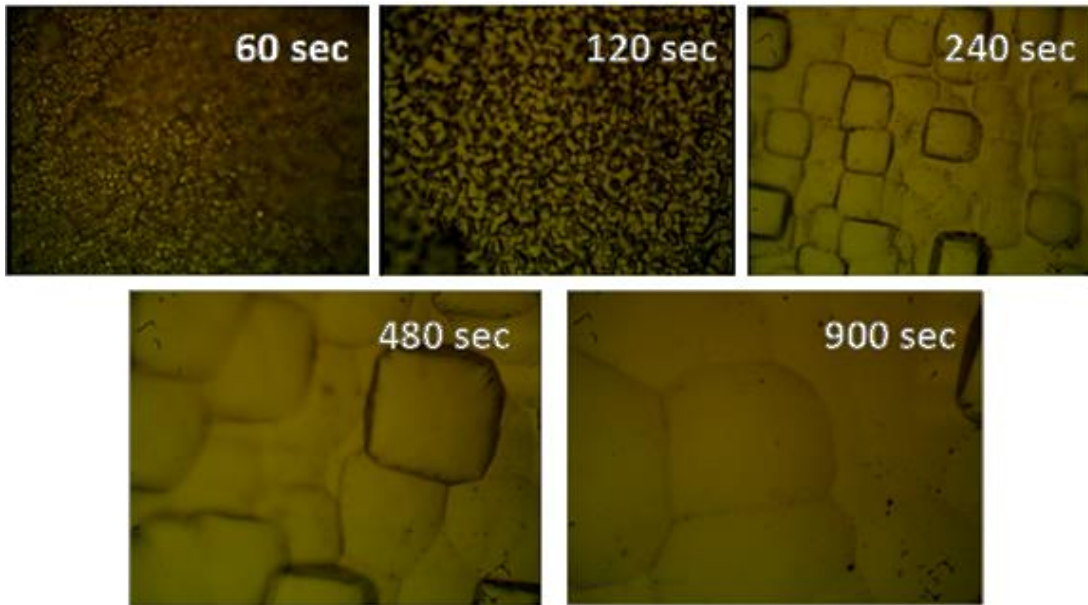


Figure 45: Optical microscope images of etched surfaces in KOH-H₂O₂-H₂O (40%-10%-40%) solution with respect to process time [All images are at 1500x magnification]

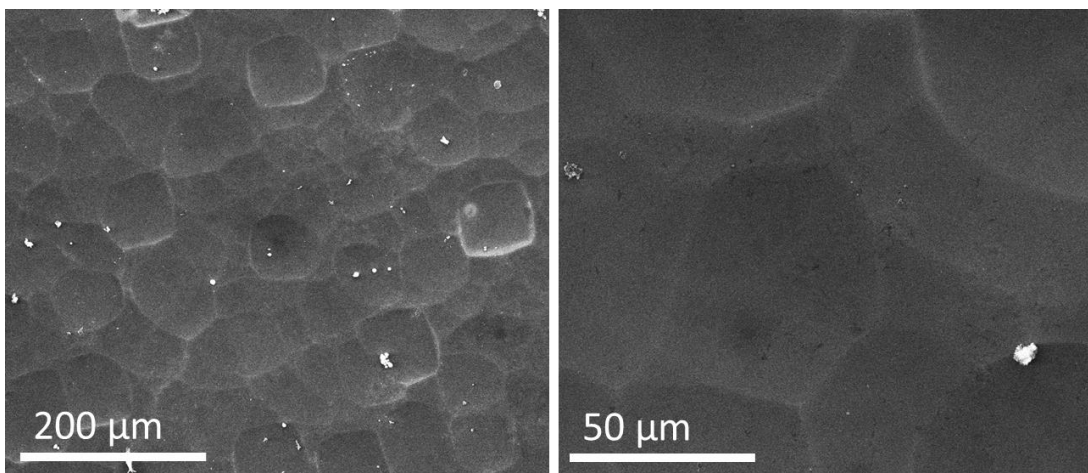


Figure 46: SEM images of etched surface in KOH-H₂O₂-H₂O (40%-10%-40%) solution with etching time 480 s

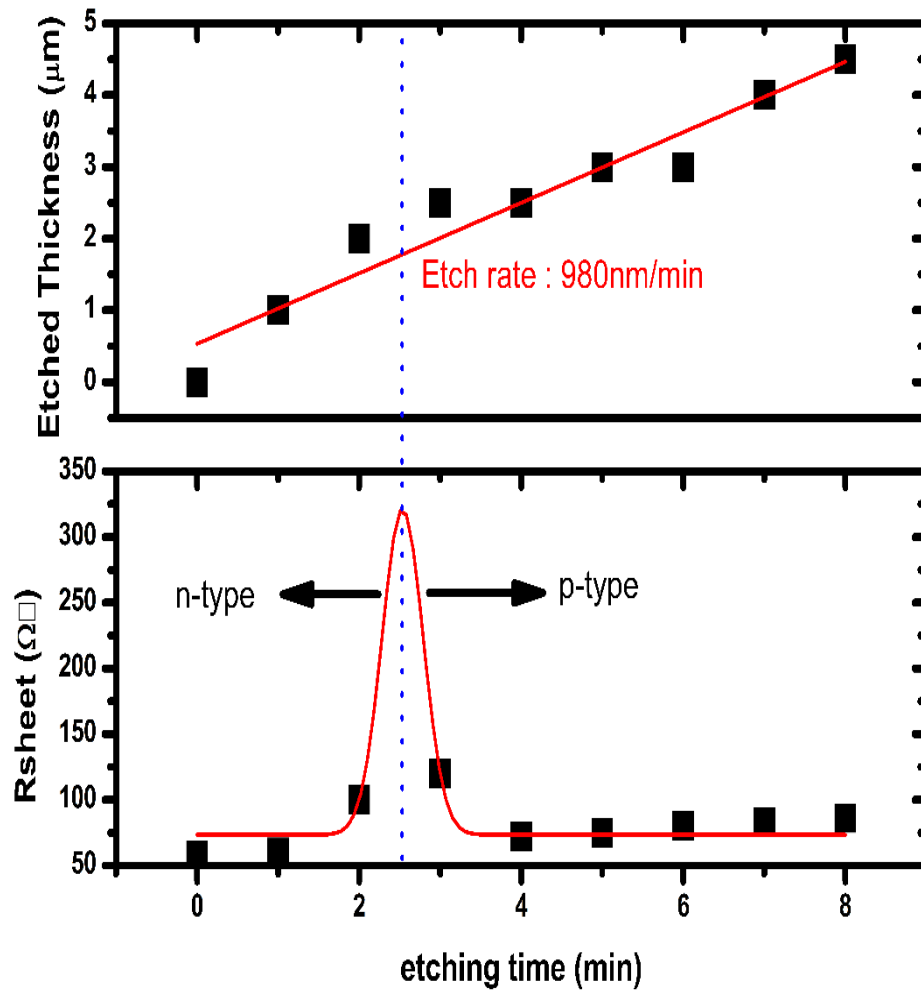


Figure 47: Rear side n-layer etching and etching thickness results

After KOH rear side polishing process, sheet resistances of front surface and rear surface were measured to be sure about nitrite front surface protection and rear surface n-layer removal. Figure 48 indicates that front surface of the wafer was protected since the sheet resistance values indicates that front surface is n-layer. Figure 49 indicates that n-layer on the rear surface of the cell was etched. Figure 50 is the SEM images of the surfaces of the sheet resistance measurements.

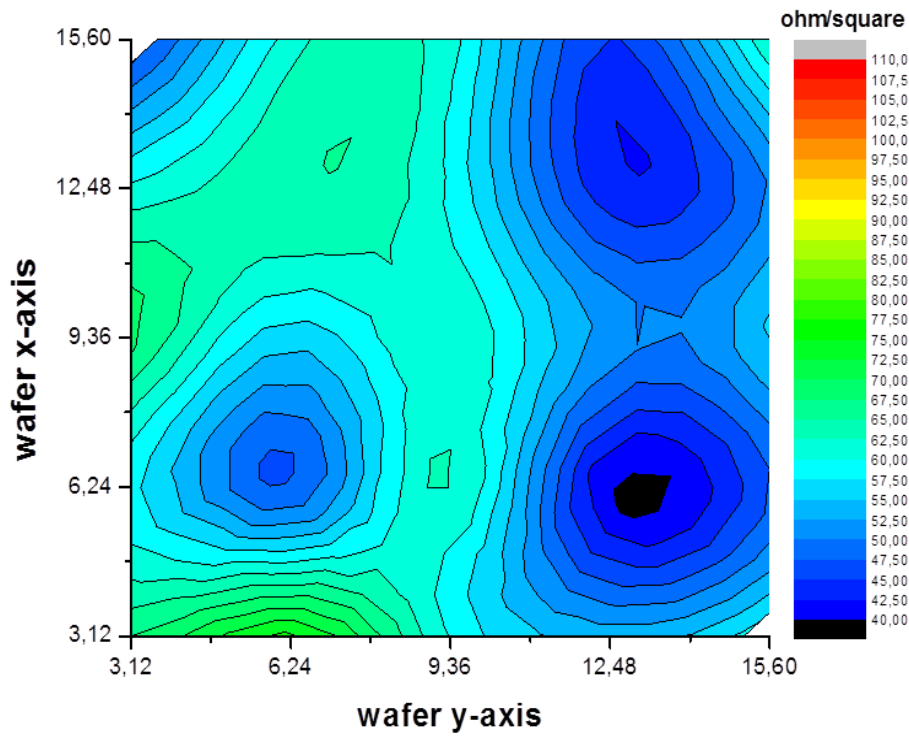


Figure 48: PERC sample front surface sheet resistance graph

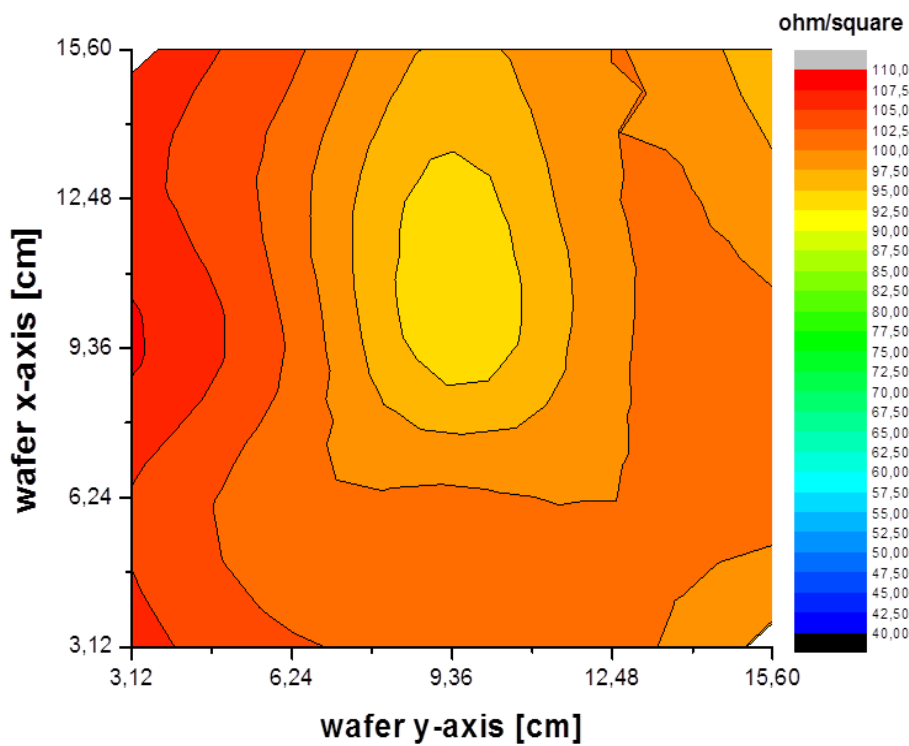


Figure 49: PERC sample rear surface sheet resistance graph

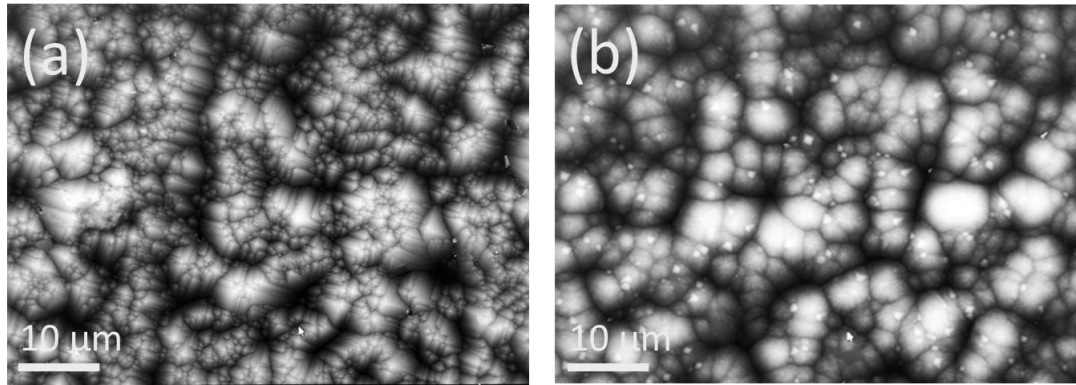


Figure 50: SEM pictures of, (a) silicon nitride covered front surface and (b) etched rear surface of the PERC sample

5.2 Backside Passivation Results

Passivation quality of backside passivation was measured with life-time measurements[51]. Life-time of electron-hole pair in the cell indicates the passivation quality of the cell. Life-time measurements took place before annealing step of production, after annealing and after firing. Since annealing and firing steps of PERC cell production took place at high temperatures. Dielectric layers may be damaged by exposing high temperatures for long time therefore life-time values were measured before and after annealing and firing processes. Actually, expected graph was increased life-times after annealing and firing processes. However, annealing process caused decrease in life-time values (Figure 51& 52). This may be caused by the contamination problem of the furnace or the high annealing temperature and time. Annealing process was done for the metallization layer diffusion. Different temperatures and different annealing times were processed to find the lowest back metal contact. Transmission line method (TLM) was used to measure the resistance of the back metal contacts, which is discussed in next section. Finally, annealing of 40 minutes at 800°C and second annealing (after second Al evaporation) 30 minutes 400°C was found to result in the minimum contact resistance.

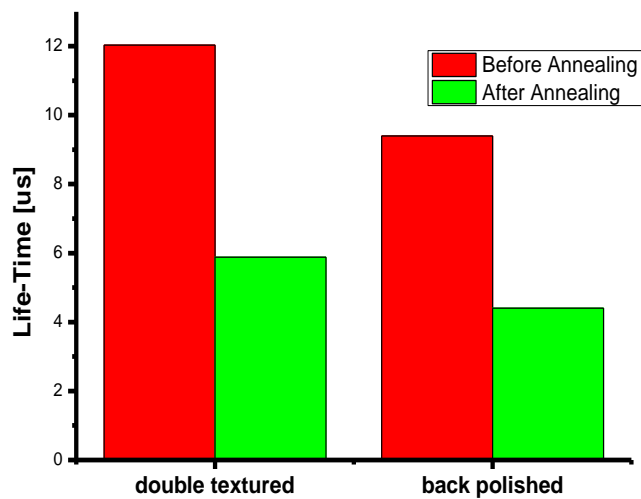


Figure 51: Average life-time graphs of samples done for PERC process

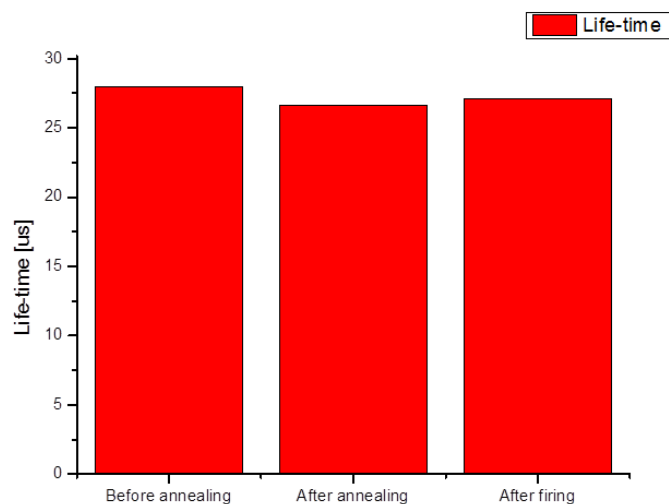


Figure 52: Life-time measurement graph of PERC set sample

For the firing process, screen printing method was used. After the printing of the Ag layer, cells were exposed to 800°C furnace for a short time. However, it didn't affect the life-time value (Figure 52).

5.3 Laser Structuring Results

TLM measurement preparation procedure is shown in Figure 53. For transmission line method measurements, current-voltage measurements were taken place between the laser ablated lines. I-V curve of a good contact design indicates linear graph (Figure 17). The slope of the I-V curves indicates the resistance between the measured ablated lines. Then, resistance and contact distance values graph was drawn to calculate the contact resistance of the laser ablation parameter (Figure 18). Slope equation of the resistance vs contact distance graph was $y=ax+b$. Moreover, b value of the slope equation is twice the contact resistance.

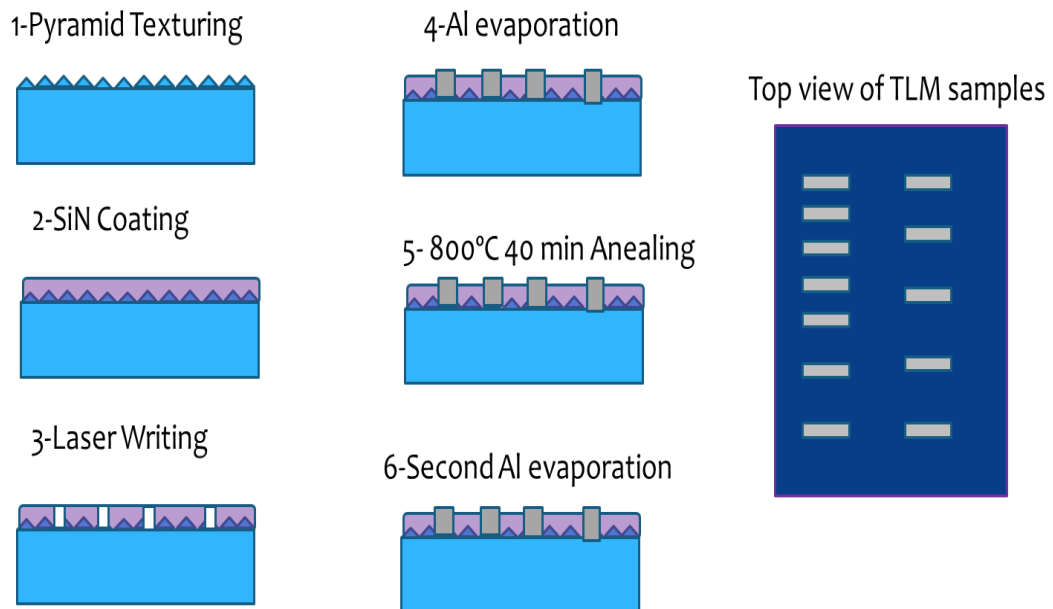


Figure 53: Transmission line method measurement preparation procedure

Contact resistance values of the laser parameters used in TLM measurement method is shown in Table 3. In Table 3, second annealing after second evaporation is indicated that it decreases the contact resistance. Hence, second annealing was added to the PERC cell procedure. First annealing was processed 40 minutes at 800°C. However, second annealing was processed 30 minutes at 400°C. Moreover, SEM view of TLM sample 1 and TLM sample 4 is shown in Figure 54 and Figure 55. Actually, laser ablation procedures are processed on polished surfaces. However, pyramid textured processes were chosen to be the surface texture of TLM samples.

Since, laser parameter accuracy of not melting the wafer could be seen from the optical and SEM view of laser ablation on textured surfaces.

Table 3: Transmission line method results

	Frequency [kHz]	Current [%]	Draw Step	Step Period	Resistance [Ω]			Normalized Resistance [$m\Omega.cm^2$]		
					Last Trial		Previous	Last Trial		Previous
					1st aneal	2 nd aneal		1st aneal	2 nd aneal	
1	30	100	40	20	42.9	1.5	8.5	77.2	2.7	15.3
2	SiN _x surface [no laser writing]				15.6	9.0	-	28.0	16.2	-
3	Si surface [no laser writing]				5.9	0	0	10.6	0	0
4	30	25	10	40	2.3	1.5	1.5	4.1	2.7	2.8
5	40	24	13	70	11.5	6.4	-	20.7	11.6	-
6	30	27	13	70	13.8	6.0	-	24.8	10.9	-
7	30	25	10	80	46.4	5.6	-	83.5	10.8	-
8	30	28	10	40	9.4	10.6	-	16.9	19.1	-

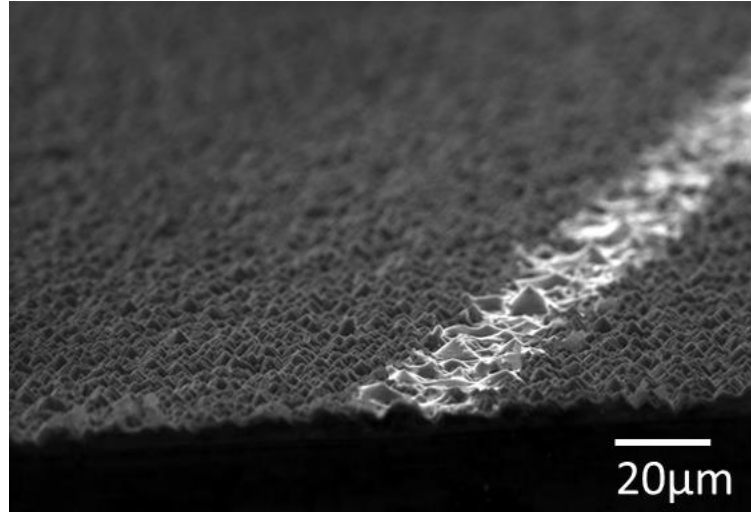


Figure 54: SEM view of TLM sample 1 (Table 3)

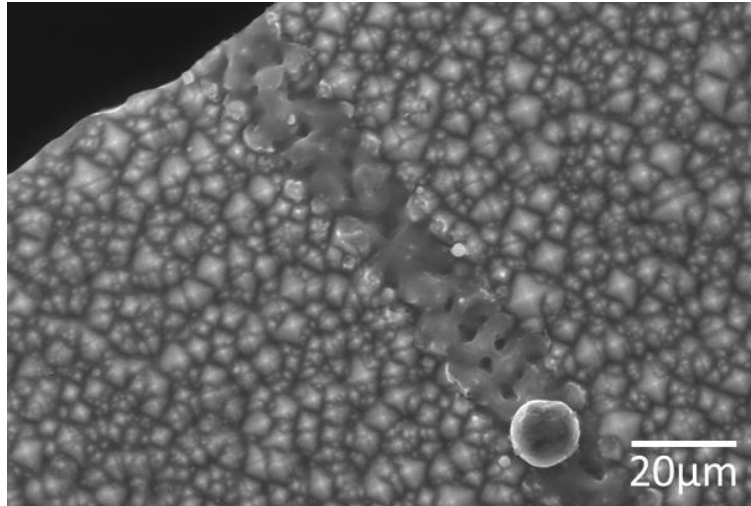


Figure 55: SEM view of TLM sample 4 (Table 3)

5.4 Rear Surface Metal Coverage

After the decision of laser parameter, rear surface metal coverage percentage of PERC cell production step was next. To decide the rear surface metal coverage percentage, simulation of the cell design was used. Simulation of the design of the PERC production was processed by GÜNAM researcher Hande Çiftçinar.

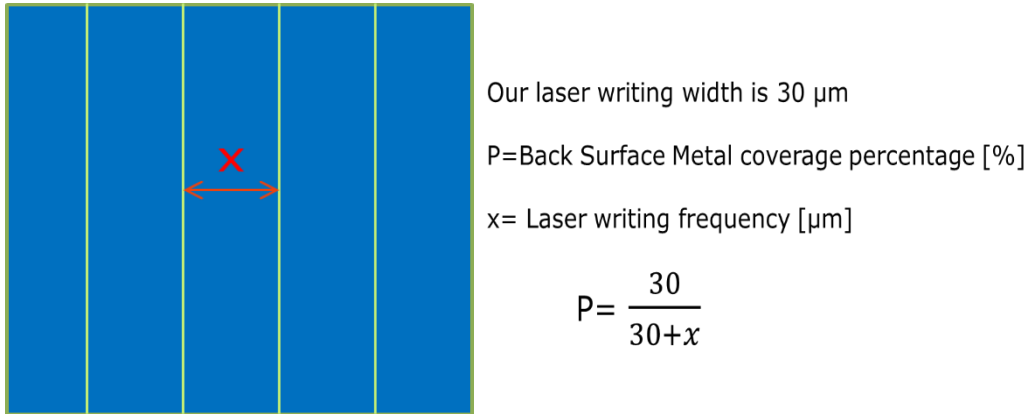


Figure 56: Calculation of laser writing frequency [Green lines represents laser writing, blue square represents rear surface of the wafer, x represents distance between laser written-lines]

In Figure 56, back surface metal coverage calculation is indicated. Rear surface metal coverage percentages are the back surface local Al back surface field contact percentages. Hence, changing the distance between the laser-written lines changes the electric field in the cell. The aim of rear surface metal coverage parametrization is to enhance the back surface field and minimize the recombination and enhance the cell performance. At this point, simulation of the PERC solar cell design was used. Quakka computer simulation program for solar cells was used in this research.

From the Quakka simulation results, rear surface metal coverage percentage values between 8% and 28% results in maximum fill factor and open circuit voltage values (Figure 57). Above than 10% of back surface metal coverage percentages efficiency and short circuit current values saturate at the best performance (Figure 58). Moreover, loss percentage values of quakka simulation indicate that above 10% of back metal coverage percentage loss of the produced cell is minimized (Figure 59). Since below than 10% local back surface field and electric field, which provides electron-hole separation and current formation in the cell, are very low. From the all the Quakka simulation results, back metal percentages between 10% and 30% indicates the best PERC cell performance.

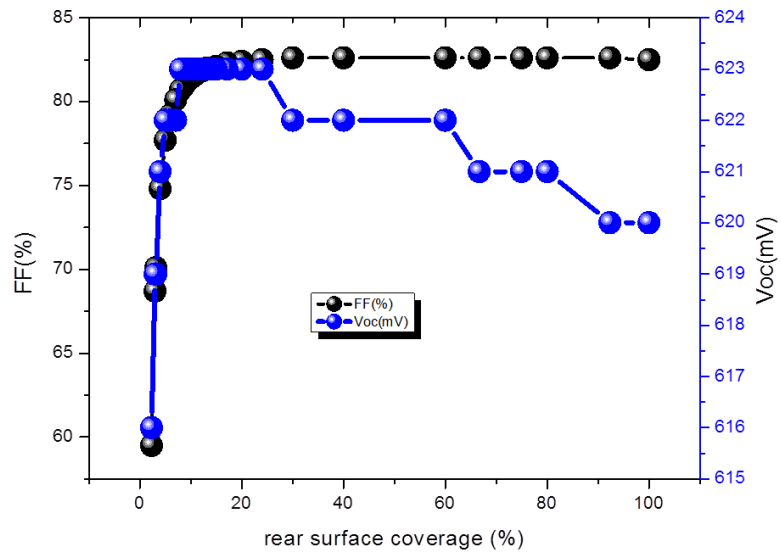


Figure 57: Quakka simulation result graph of Fill Factor (FF) and Open circuit voltage (Voc) vs. rear surface metal coverage percentage

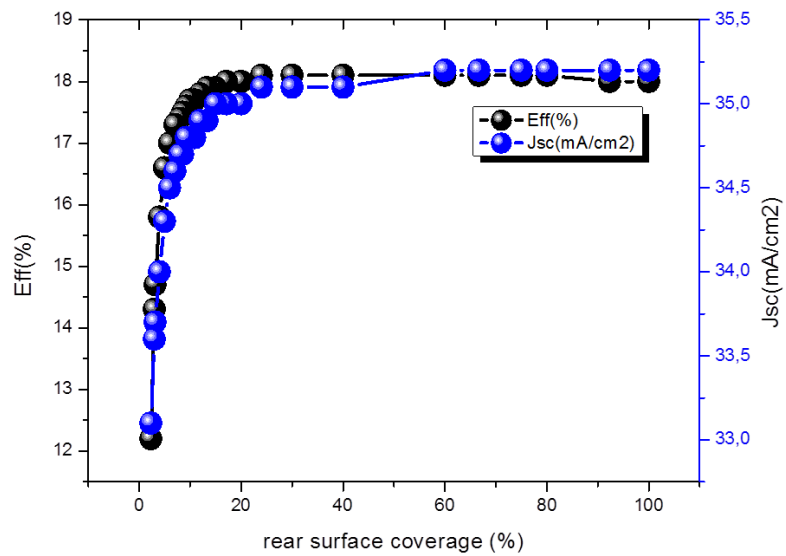


Figure 58: Quakka simulation result graph of Efficiency and Short circuit current (Jsc) vs rear surface metal coverage

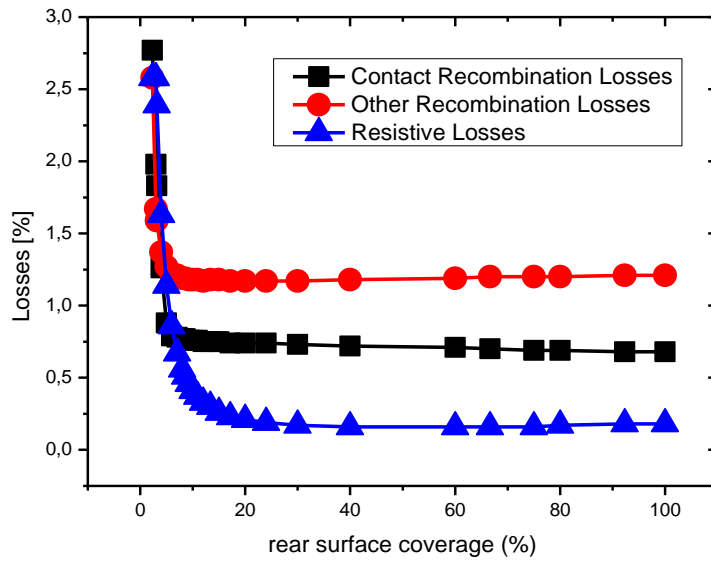


Figure 59: Quakka simulation result of loss percentages vs. rear surface metal coverage

5.5 Produced PERC solar cell results

5.5.1 First PERC solar cell production

The aim of the first PERC solar cell production was to make sure that the design was working practically. Experimental procedure sequence is shown in Figure 24. Fast laser parameter (velocity: 5493 mm/sec, frequency:30kHz, power:100%) was only used for backside laser openings of the first trial. Backside metal coverage percentages of %0, %50 and %100 (reference standard crystalline solar cell) were processed. Table 4 indicates the results of our production. To be sure about the accuracy of efficiency and Jsc results, quantum efficiency results were also measured. With the average values of the production results, Voc and fill factor vs back metal coverage graph (Figure 61), efficiency and Jsc vs back metal coverage graph (Figure 62) were plotted. Our production results are not as high as quakka simulation results. However, experimental results and simulation results are consistent with the change in parameters according to back metal coverage percentage. When simulation results (Figure 57 and Figure 58) and experimental

graph of first production results (Figure 60 and Figure 61) are compared increment and decrease in parameters according to back metal surface coverage change is quite similar.

Table 4: Results of first production

Back Metal Coverage [%]	Voc [mV]	FF [%]	Jsc [mA/cm ²] QE corrected	Efficieny [%] QE corrected
100	531	60.65	23.07	7.43
100	515	36.19	27.95	5.21
100	564	37.59	31.94	6.77
50	552	56.81	33.12	10.39
50	544	56.62	30.33	9.34
50	561	56.90	34.62	11.07
0	426	22.25	20.75	1.97
0	539	24.45	33.35	0.48
0	213	-	0.04	-

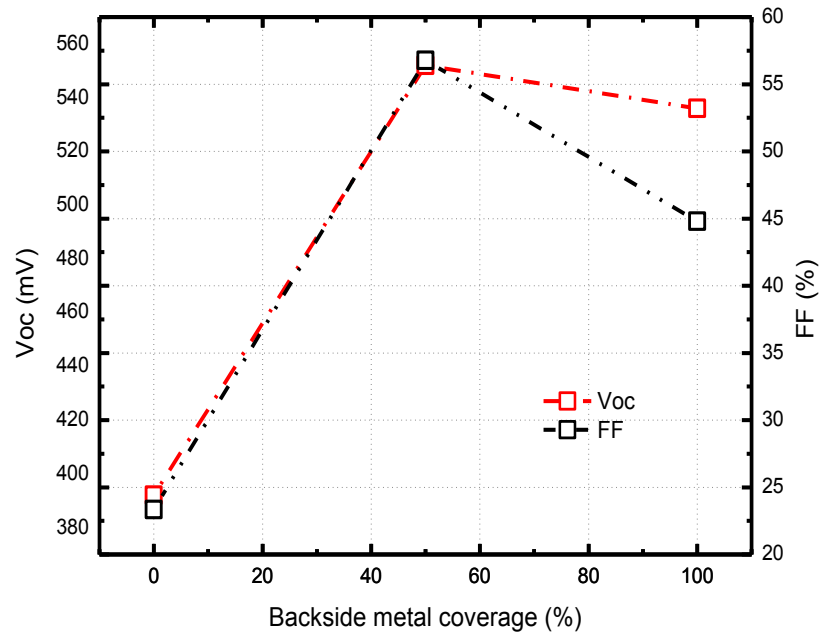


Figure 60: Open circuit voltage and fill factor vs. back metal coverage graph

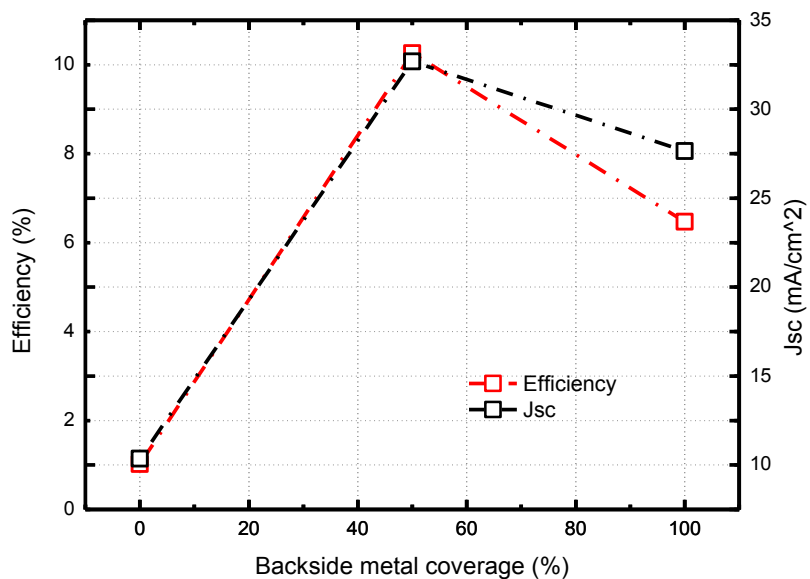


Figure 61: Efficiency and short circuit current vs. back metal coverage graph

Table 5: SunsVoc results of first production

Back Metal Coverage [%]	Voc [mV]	FF [%]	Jsc [mA/cm ²]	Pseudo Efficiencny [%]
100	552	74.3	35	14.3
100	534	73.1	35	13.6
100	570	80.6	35	16.1
50	544	73.5	35	14.0
50	543	74.4	35	14.1
50	563	76.2	35	15.0
0	541	79.5	35	15.0
0	582	76.6	35	15.6
0	150	43.4	35	0.2

Table 5 indicates the SunsVOC results of the first production. Average values of the SunsVoc results are more close to simulation results. Since, laser writing caused the dirt on wafer before aluminium evaporation. This can cause the decrease in the parameters of first production.

Figure 62 indicates the SEM images of aluminium local back contacts. At the top image (a), one can see the laser writing pulses. Also, the dirt on the wafer caused by the laser writing can be seen clearly. The pictures at the bottom (b) and (c) are zoomed in to the crossection of aluminium local back contacts.

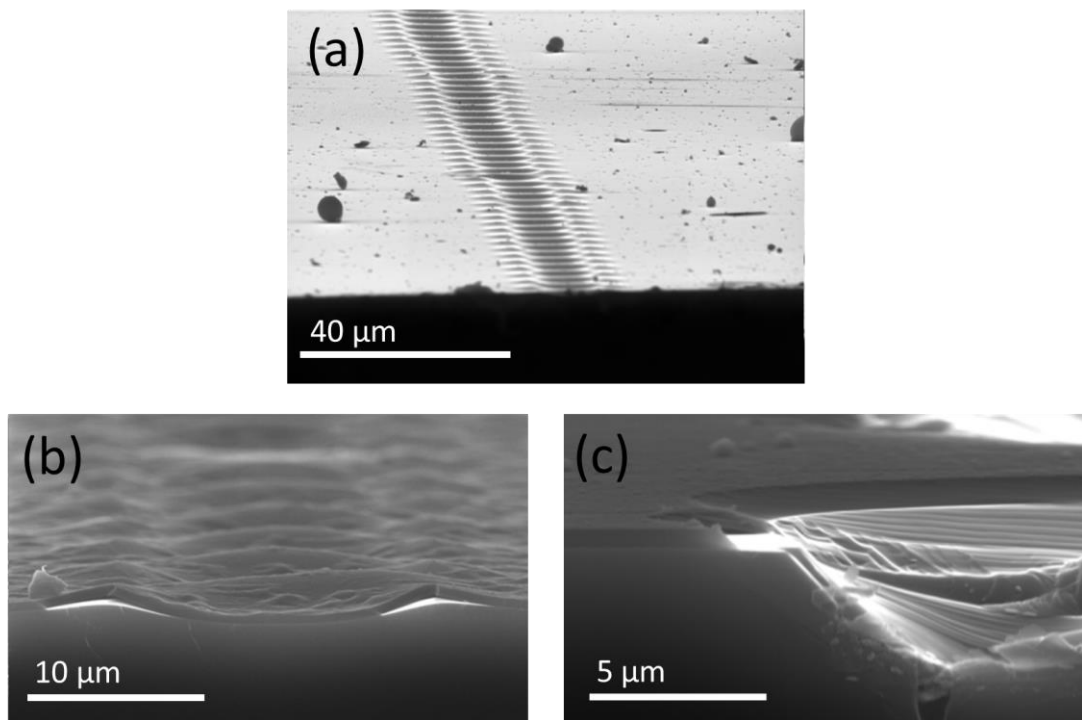


Figure 62: SEM images of aluminium local back contacts (a) view of aluminium local back contacts after the laser writing, (b) and (c) are zoomed pictures showing the cross-section.

5.5.2 Second PERC solar cell production

The aim of the second PERC solar cell production was to scan the back surface metal coverage parameter values. Experimental procedure sequence is shown in Figure 24. Chosen TLM optimized laser parameters (velocity: 5493 mm/sec, frequency: 30kHz,

power: 100% and velocity: 586 mm/sec, frequency: 30 kHz, power: 25%) was used for backside laser openings. Backside metal coverage percentages of 0%, 2%, 5%, 8%, 10%, 30%, 75% and 100% (reference standard crystalline solar cell) were processed. To be sure about the accuracy of efficiency and Jsc results, quantum efficiency results were also measured.

With the production results, Voc and fill factor vs back metal coverage graph (Figure 63 and 64), efficiency and Jsc vs back metal coverage graph (Figure 69 and 70) were plotted. Our second production results are not as high as Quakka simulation results. However, experimental results and simulation results are consistent with the change in parameters according to back metal coverage percentage. When simulation results (Figure 57 and Figure 58) and experimental graph of second production results (Figure 63, 64, 65 and 66) are compared increment and decrease in parameters according to back metal surface coverage change is quite similar. Moreover, associate maximum data point of FF and Voc are at the 10% of back surface metal coverage point on the simulation and laser parameter 1 [velocity: 586 mm/sec, frequency: 30 kHz, power: 25%] graph, whereas laser parameter 2 [velocity: 5493 mm/sec, frequency: 30kHz, current: 100%] graph's associate maximum data is at 5%. Laser parameter 2 is more powerful than laser parameter 1. That strength might cause small defects in silicon surface over dielectric layers. At simulation graph of efficiency and Jsc vs back surface metal coverage results starts with minimum efficiency at 0% back surface metal coverage, increases until 20% back surface metal coverage point and stabilized after that. However, our second production experimental data indicates decrease after 30% of back surface metal coverage. Possible cause of efficiency decrease in production may be caused by the laser dirt of back surface laser openings and dirt of the annealing tube.

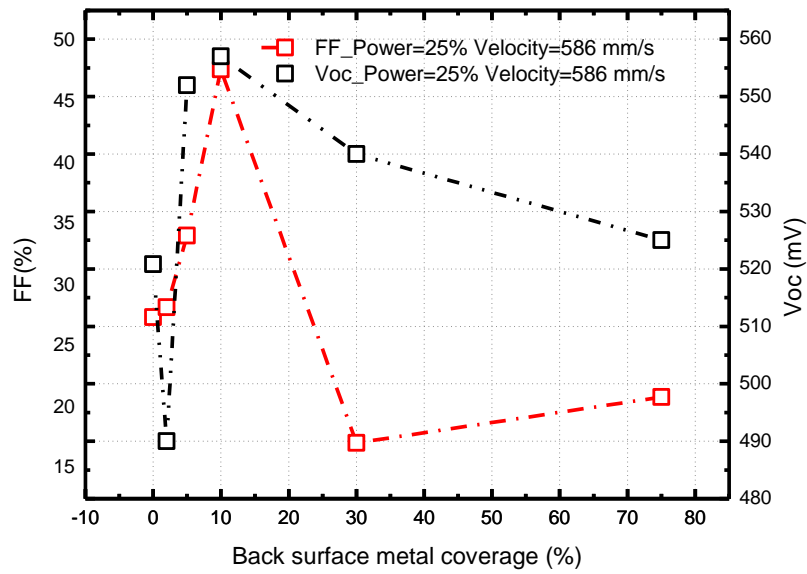


Figure 63: Open circuit current and Fill Factor vs. Back metal coverage graph of laser parameter 1 [velocity: 586 mm/s, frequency: 30 kHz, power: 25%]

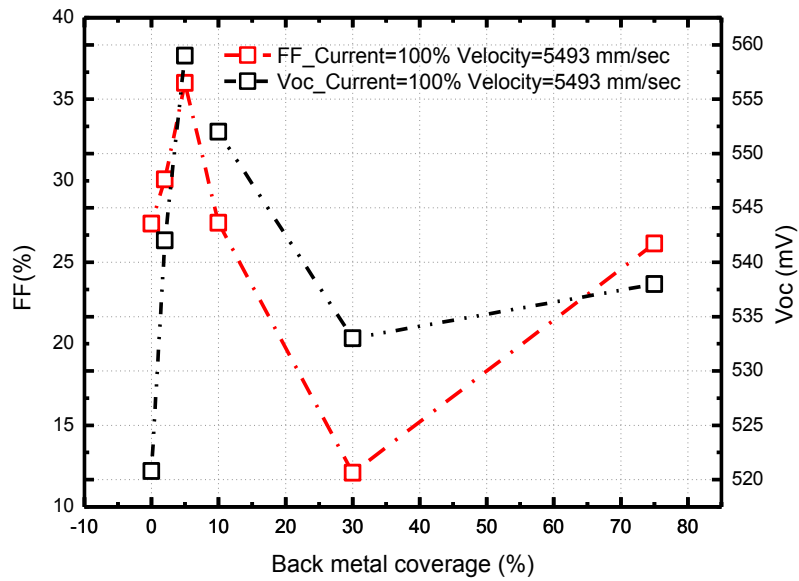


Figure 64: Open circuit current and Fill Factor vs. Back metal coverage graph of laser parameter 2 [velocity: 5493 mm/s, frequency: 30kHz, power: 100%]

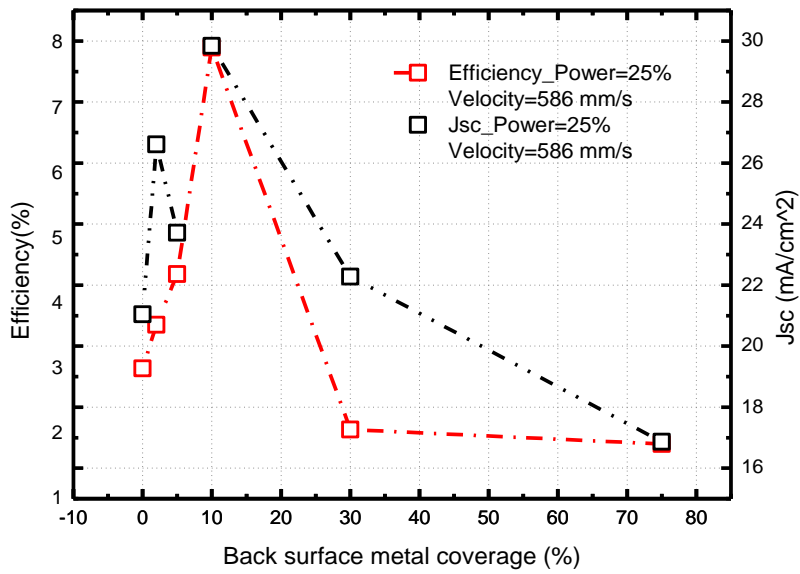


Figure 65: Efficiency and short circuit current vs. Back metal coverage graph of laser parameter 1 [velocity: 586 mm/s, frequency: 30 kHz, power: 25%]

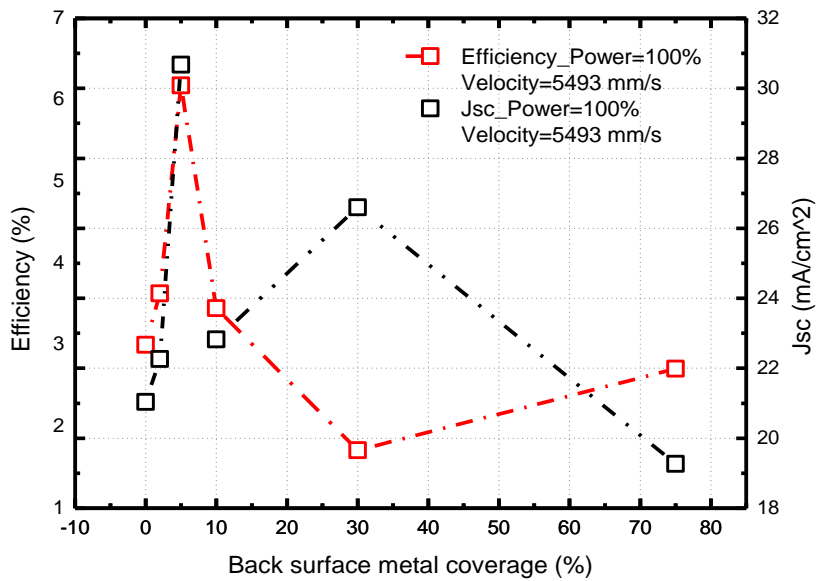


Figure 66: Efficiency and Jsc vs. Back metal coverage graph of samples produced using laser parameter 2 [velocity: 5493 mm/s, frequency: 30kHz, power: 100%]

Table 6: Reference production solar cell results

Efficiency [%]	FF [%]	Voc [mV]	Jsc [mA/cm ²]
3.33	26.33	538	23.52

Table 6 indicates the reference production results. Figure 67 indicates pseudo efficiency values vs back surface metal coverages of the second PERC cell production. Reference efficiency is exceeded by three produced PERC cells. Figure 68 indicates pseudo fill factor values vs back metal coverages of the second PERC cell production. Pseudo fill factor vs back metal coverage result graph trend is very similar to the simulation fill factor vs back metal coverage result (Figure 57). Figure 69 indicates $i-V_{oc}$ values vs back metal coverages of the second PERC cell production. $i-V_{oc}$ values vs back metal coverage graph's laser parameter 2 [Power=25%, velocity=586mm/s] trend is also very similar to the simulation Voc vs back metal coverage result (Figure 58).

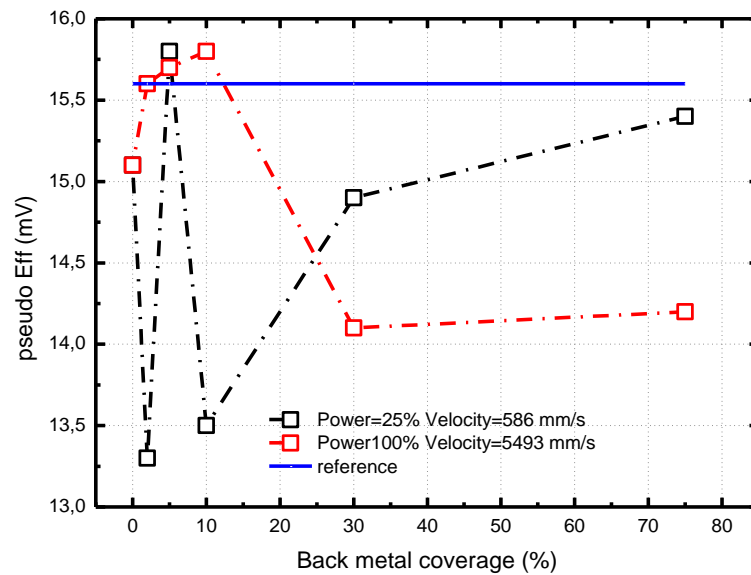


Figure 67: Pseudo efficiency [SunsV_{oc} results] versus back metal coverage graph

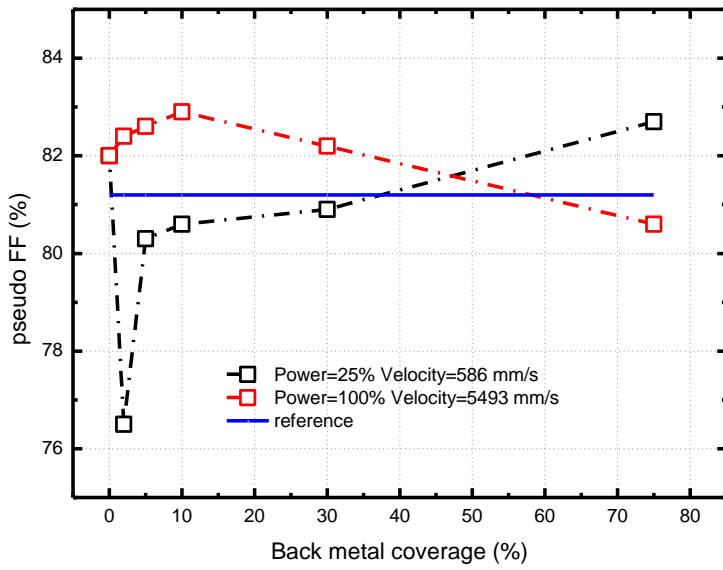


Figure 68: Pseudo Fill Factor [SunsV_{oc} results] versus back metal coverage graph

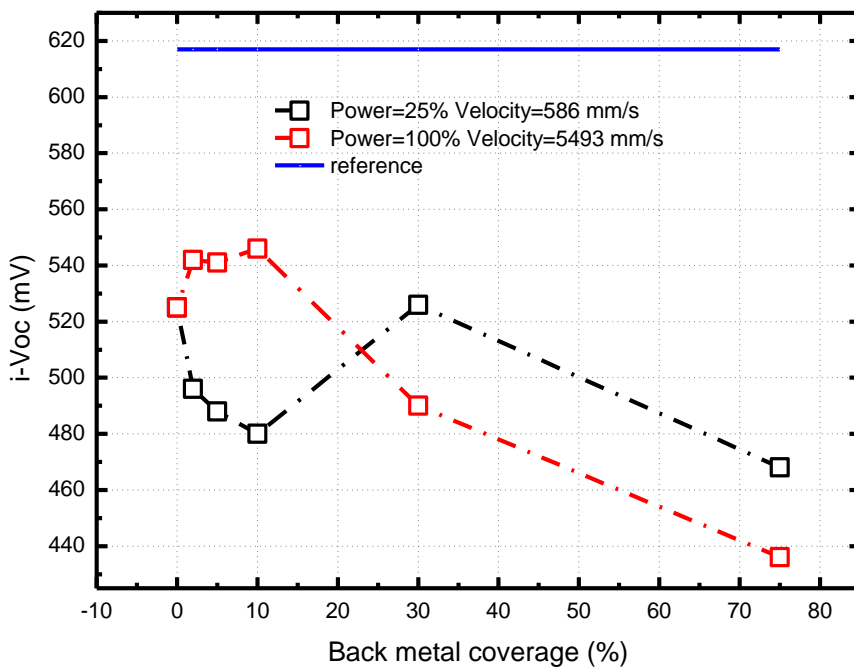


Figure 69: i-Voc [SunsV_{oc} results] versus Back metal coverage graph

5.5.3 Third PERC solar cell production

Table 7: Characterization data obtained from 0% back surface metal coverage sample and reference sample

	Voc [mV]	FF [%]	Jsc [mA/cm ²] QE corrected	Efficiency [%] QE corrected
0% back surface metal coverage	553	58.9	33.5	11.51
Reference	550	51.7	33.8	10.14

Table 8: Characterization results of laser parameter 1 [power= 100%, velocity= 5493 mm/s]

Back Metal Coverage [%]	Voc [mV]	FF [%]	Jsc [mA/cm ²] QE corrected	Efficiency [%] QE corrected
5	548	71.3	32.8	13.5
8	553	65.1	33.3	12.6
10	560	70.6	33.8	14.1
14	555	66.9	33.3	13.0
16	557	67.7	33.3	13.3
18	546	65.8	33.8	12.8
20	556	65.5	33.9	13.0
22	553	49.2	34.1	9.8
24	557	66.2	33.4	13.0
26	547	58.6	33.5	11.3
30	543	40.2	33.1	7.6
50	558	28.3	33.0	5.5
80	548	25.2	0.3	0.05

At third production, second anneal was removed from the experimental procedure (Figure 24). Since, both second annealing and firing step after screen printing of the front surface of the produced cells damaged the passivation and reduce the life-time. Hence, second annealing step was decided to be excluded from the production procedure. Then, results of production have increased dramatically as shown in Table 7, 8 and 9.

Table 9: Characterization results of laser parameter 2 [power= 25%, velocity= 586 mm/s]

Back Metal Coverage [%]	Voc [mV]	FF [%]	Jsc [mA/cm ²] QE corrected	Efficiency [%] QE corrected
5	551	70.7	33.8	13.9
8	557	72.4	33.3	14.1
10	551	67.7	33.4	13.1
14	553	64.2	33.0	12.4
16	556	68.4	33.5	13.4
18	552	70.6	33.5	13.7
20	530	48.3	33.6	9.0
22	555	67.7	32.6	13.0
24	512	41.7	33.5	7.5
26	538	51.6	33.1	9.7
30	551	39.2	33.2	7.5
50	552	66.7	33.1	12.8
80	551	55.0	33.3	10.6

Figure 70 indicates fill factor vs. back surface metal coverage graph of laser parameter 1 [Power= 100%, velocity= 5493 mm/s]. Experimental and simulation trend is close to each other. However, experimental values are lower than the simulation values due to the experimental defects of production. Moreover, produced reference sample fill factor result is passed by the PERC production (Figure 70). Figure 71 indicates the Voc vs. back surface metal coverage graph of laser parameter 1 [Power= 100%, velocity= 5493 mm/s]. As shown in the figure experimental and

simulation trend are very similar. However, experimental values are also lower than the simulation results. Moreover, produced reference sample Voc value is also passed by PERC production (Figure 71). Figure 72 indicates Jsc vs. back surface metal coverage graph of both laser parameters [Power= 100%, velocity= 5493 mm/s and Power= 25%, velocity= 586 mm/s] and reference sample. Reference sample short circuit current density is passed by the production of laser parameter 1 and 22% back surface metal coverage PERC sample.

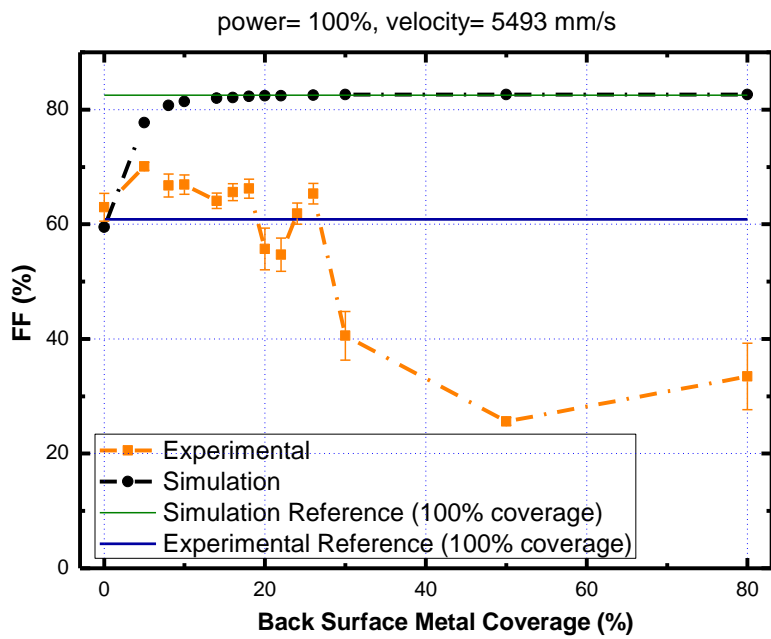


Figure 70: Fill Factor versus back surface metal coverage graph of laser parameter 1 [Power= 100%, velocity= 5493 mm/sec]

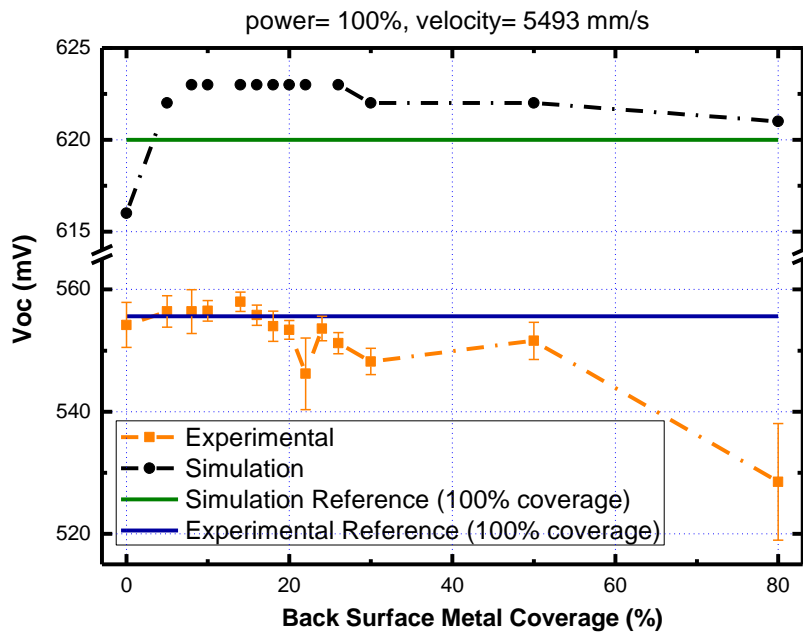


Figure 71: Open circuit voltage versus back surface metal coverage graph of samples produced using the laser parameter 1 [Power= 100%, velocity= 5493 mm/sec]

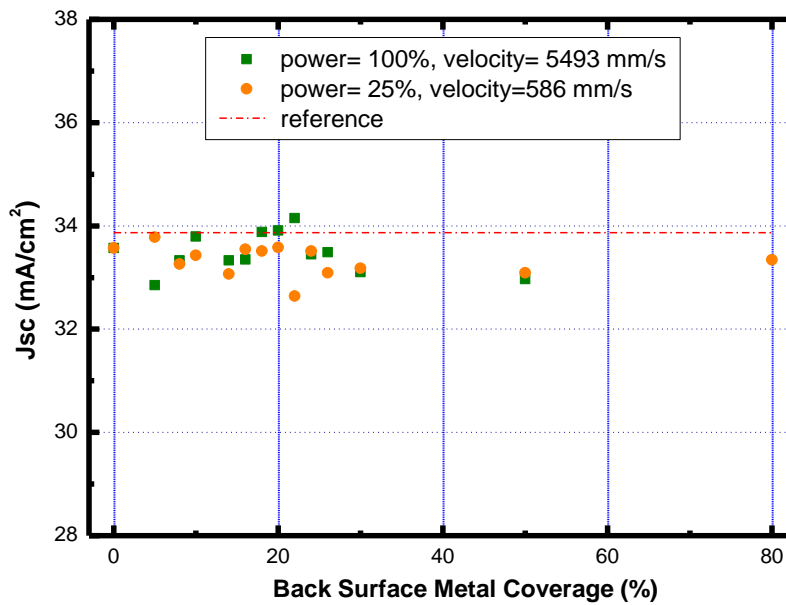


Figure 72: Short circuit current density versus back surface metal coverage graph of samples produced using the laser parameters [Power= 100%, velocity= 5493 mm/s and power= 25%, velocity= 586 mm/s] compared to the reference sample

Figure 73 indicates efficiency vs. back surface metal coverage graph of both laser parameters [power= 100%, velocity= 5493mm/s and power= 25%, velocity= 586 mm/s] and reference sample. Only 7 of 26 PERC designs are resulted in lower efficiency values than the reference cell production.

Figure 74 indicates current-voltage graph of best resulted efficiency [14.1%] produced PERC design [power= 100%, velocity= 5493mm/sec and back surface metal coverage= 10%] of third set and reference cell. PERC design of laser parameter1 with the 10% back metal surface coverage resulted in a better (higher current density and rapid decrease while reaching the maximum voltage and hence higher fill factor) I-V curve than the reference produced cell.

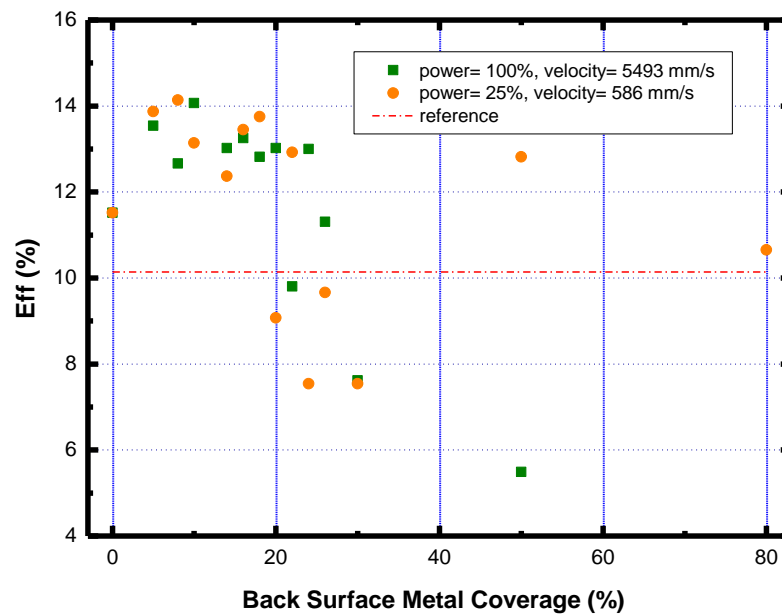


Figure 73: Efficiency vs. back surface metal coverage graph of the sample produced using the laser parameters [Power= 100%, velocity= 5493 mm/sec (orange dots) and Power= 25%, velocity= 586 mm/s (green dots)] compared to the reference sample.

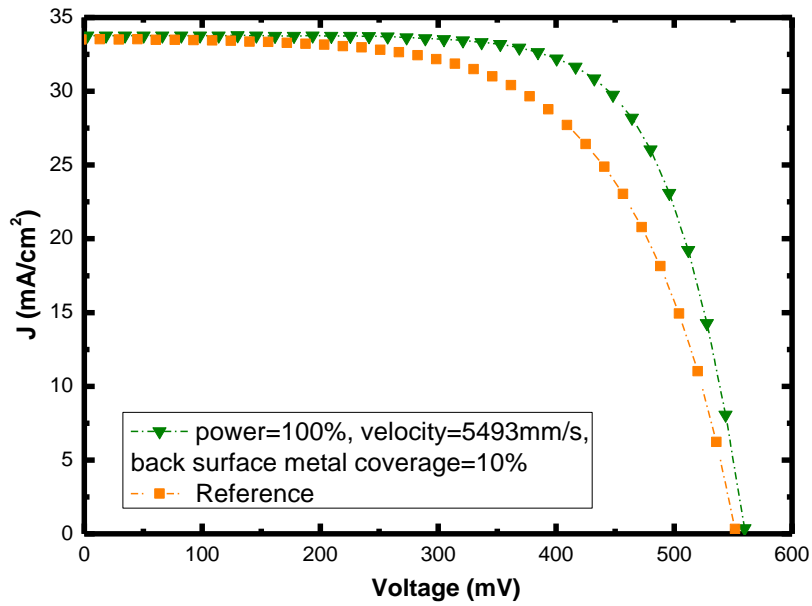


Figure 74: Current-voltage graph of best produced PERC cell compared to the reference cell

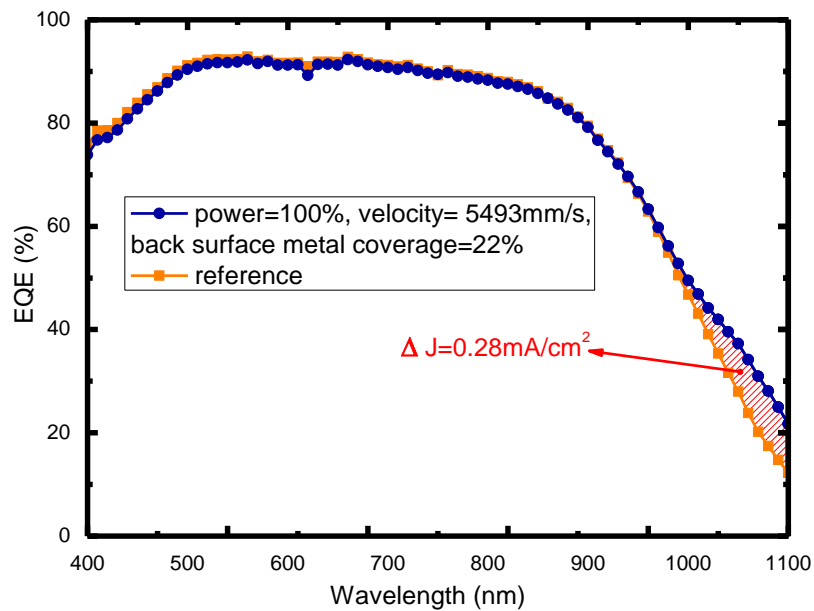


Figure 75: External Quantum Efficiency vs. wavelength graph of reference cell and best short circuit current density cell

Figure 75 indicates the external quantum efficiency values of the reference cell and best short circuit current density resulted PERC sample of third production set [power=100%, velocity=5493mm/s, laser parameter and back surface metal coverage=22%]. Increase in the quantum efficiency measurements of higher wavelength verifies that passivation layer at the back surface of the produced PERC cell works. Since, higher wavelengths are absorbed at the back surface of the solar cell.

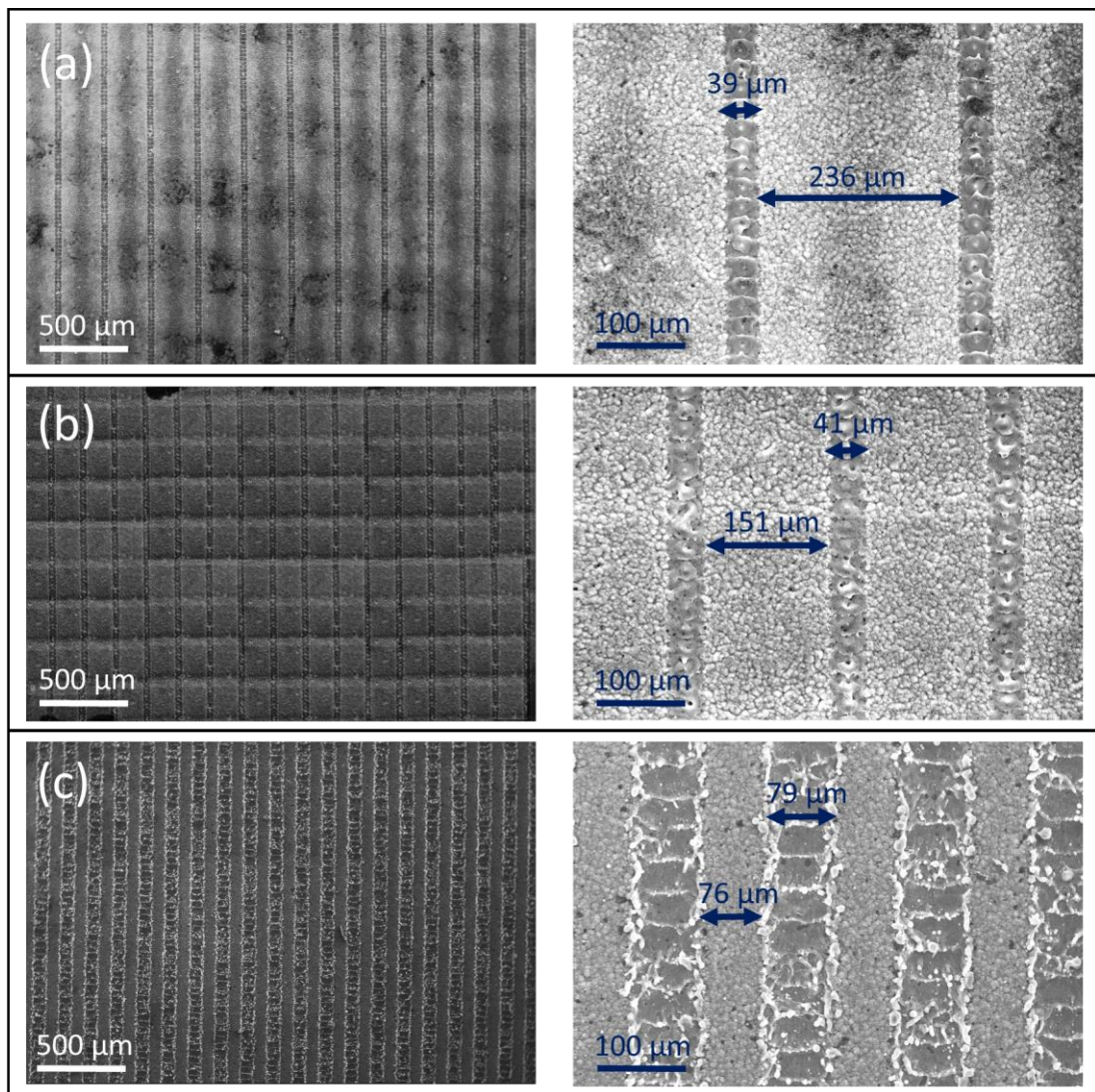


Figure 76: SEM images of laser parameter 1 [Power=100%, velocity=5493 mm/s] with calculated back surface metal coverage values of (a) 5 %, (b) 14 %, (c) 50 %.

SEM images of produced PERC cells' back surface metal contacts are shown in Figure 76. Lines in the figures are laser ablated contacts. With the decrease in the

distances of laser lines, laser ablation line width increases. This may be caused by the resolution of the laser used for the ablation. Moreover, other possible reason is that increase in the dirt of laser ablation by the decreasing distance of laser ablated lines could be appearing thicker line after metal evaporation. To decrease the dirt, femtosecond laser usage for the back surface laser ablation could be used.

CHAPTER 6

CONCLUSIONS

PERC solar cells are very promising among next generation solar cells. PERC solar cells have two main advantages over standard crystalline solar cells. The first main advantage of PERC cell is highly reduced rear side surface recombination requiring low recombination velocity and high internal reflection on the dielectrically passivated rear. The second main advantage is to reduce the silicon consumption by optical confinement of the cell structure.

PERC solar cell's working principle is very close to standard photovoltaic solar cell working principle. However, PERC cells have some benefits due to its design difference. The most important difference of PERC cell design is local back surface field contacts and passivation layer. Backside of a PERC cell is coated with dielectric layer with laser opening holes that decrease the recombination thus increases the overall efficiency. If an electron is generated near the rear side of the conventional solar cell, it is recombined by back surface metallization layer and it doesn't contribute to the overall cell current. However, the dielectric layer of PERC solar cells restrains the electron-aluminium metallization layer attraction. Hence, most of the electrons do reach the depletion region and contribute to the current.

PERC solar cell process started with production of random pyramid texturing with alkaline KOH solution. Standard RCA cleaning procedure and dilute-HF dip took place. After dilute HF-dip, cells were exposed to phosphorus diffusion to form n emitter region on both sides of wafer. Then, front side of the solar cell is coated with

a thick silicon nitrite masking layer to protect front surface in rear side polishing process. After trials of acidic solution polishing, KOH solution was chosen to be the polishing agent. Since, it is not easy to protect front side of the wafers with HNA solution etching. Single side etching tools should be used to protect other side. With KOH solution, nitrite coating was used to protect front side of the cell. Moreover, etch rate of the HNA and HF-HNO₃ solution is really high and hard to control. Hence, KOH alkaline solution was processed to produce PERC cell in this thesis work. However, acidic polishing results in higher efficiency results cleaner polished wafers. That is the first possible solution for better production for the future work.

After rear side-polishing with concentrated KOH solution, sheet resistances of rear and front surface were measured. With the sheet resistance graph of front surface, it is concluded that front surface was protected with silicon nitride coverage (Figure 48). Moreover, n-layer on the rear surface of the cell is etched with KOH polishing solution (Figure 49). Since the PERC solar cell design does have n-layer on front surface only.

After that, wafers were kept inside the HF solution to remove nitrite layer from the front side of the wafer. Then standard RCA cleaning procedure took place. Wafers were then dipped to dilute-HF solution to remove oxide layer prior to dielectric layer formation. After dielectric layer formation, back and front side of the wafer are coated with SiNx to form anti-reflection layers. After anti-reflection coating, rear side of the cell was ablated with 1064 nm pulsed laser to form local back contact openings on rear side. With the Transmission Line Method (TLM) measurements, laser parameters were optimized. Laser parameters of having 100% power, 5493 mm/s velocity and 25% power, 586mm/s velocity were chosen for the laser ablation. Then, rear side of the cell was coated with Aluminium by thermal e-beam evaporator. After Aluminium coating process, cells were fired at 800°C for 40 minutes to confine metal diffusion through laser ablated windows. To have accurate thick back metal contact, Aluminium evaporation and annealing step was applied again on the rear side. Finally, screen printing method was used to form front metal contact. However, second annealing is realized to decrease the life-time of the samples after second production. Since, firing step is also applied after front surface

metal contact screen printing method. Both second annealing and firing steps take place in high temperature environments. High temperatures over a long time result in defects in silicon crystal and damage the passivation layer on the back surface of the solar cell. That is the main reason for low first and second PERC production results. In the third PERC production, the second annealing step was omitted from the production procedure and better cell results were obtained.

Back side metal coverage percentage is the most important parameter for PERC solar cells. In the third production, back side metal coverage is also aimed to be parametrized. Power 100% and velocity 5493 mm/s laser parameters resulted in better results compared to other chosen laser parameters. The highest efficiency of 14.1 was obtained with 10% back surface metal coverage percentage parameter. Moreover, PERC cell production results exceeded the results of reference cell production. Laser ablation caused dirt on the back surface of the cell, which may result in a decrease in production results. To decrease the dirt, femtosecond laser could be used.

From the results of the third production, it can be concluded that PERC solar cell increases cell performance due to an increase in absorption on the rear surface of the cell. Hence, longer (above than 900 nm) wavelengths can be absorbed with the back surface passivation layer of PERC cell design.

With the above mentioned improvements, an increase of a 7% efficiency can be further expected.

REFERENCES

- [1] F. R. Spellman, *Environmental impacts of renewable energy*. 2014.
- [2] L. Łukasiak and A. Jakubowski, “History of Semiconductors”, *J. of Telecom and Inf Tech*, 2010.
- [3] R. Williams, “Bequerel photovoltaic effect in binary compounds,” *J. Chem. Phys.*, vol. 32, no. 5, pp. 1505–1514, 1960.
- [4] H. Spanggaard and F. C. Krebs, “A brief history of the development of organic and polymeric photovoltaics,” *Sol. Energ. Mat. Sol. C*, vol. 83, no. 2–3, pp. 125–146, 2004.
- [5] ““NREL Best Research Cell Efficiencies.” [Online]. Available: http://www.nrel.gov/ncpv/images/efficiency_chart.jpg. [Accessed: 10-December-2015]
- [6] T. Saga, “Advances in crystalline silicon solar cell technology for industrial mass production,” *NPG Asia Mater.*, vol. 2, no. 3, pp. 96–102, 2010.
- [7] S. Edition, *Photovoltaic Science Handbook of Photovoltaic Science*. 2011.
- [8] A. G. Aberle, “Thin-film solar cells,” *Thin Solid Films*, vol. 517, no. 17, pp. 4706–4710, 2009.
- [9] “Thin-Film-Solar-Cell.” [Online], Available: <http://www.circuitstoday.com/thin-film-solar-cell> [Accessed:10-May-2015] .
- [10] M. Grätzel, “Dye-sensitized solar cells,” vol. 4, pp. 145–153, 2003.
- [11] J. F. Geisz and D. J. Friedman, “III N V semiconductors for solar photovoltaic applications,” *Semicond. Sci. Technol.*, vol. 17, no. 8, pp. 769–777, 2002.
- [12] W. De Soto, S. a. Klein, and W. a. Beckman, “Improvement and validation of a model for photovoltaic array performance,” *Sol. Energy*, vol. 80, no. 1, pp. 78–88, 2006.

- [13] M. Wolf, "Limitations and Possibilities for Improvement of Photovoltaic Solar Energy Converters: Part I: Considerations for Earth's Surface Operation," *Proc. IRE*, vol. 48, no. 7, pp. 583–595, 1960.
- [14] "Photovoltaic Solar Cell" [Online], Available: <http://solarlove.org/how-solar-cells-work-components-operation-of-solar-cells/> [Accessed: 10-November-2015]
- [15] A. Adud, "Advance Temperature Modeling of Solar PV," November, 2011.
- [16] a. R. Jha, *Solar Cells Technology and Applications*, 2010.
- [17] D. K. Schroder and D. L. Meier, "Solar cell contact resistance - A review," *IEEE Trans. Electron Devices*, vol. ED-31, no. 5, pp. 637–647, 1984.
- [18] A. H. H. Ali, Y. Matsushita, and S. Ookawara, "Photovoltaic Module Thermal Regulation: Effect of the Cells Arrangement Configurations on the Performance," *Int. J. Therm. Environ. Eng.*, vol. 2, no. 1, pp. 41–47, 2010.
- [19] W. Shockley and H. J. Queisser, "Detailed Balance Limit of Efficiency of p-n Junction Solar Cells," *J. Appl. Phys.*, vol. 32, no. 3, p. 510, 1961.
- [20] "Spectral irradiance of Silicon" [Online], Available: <http://lasp.colorado.edu/home/sorce/instruments/sim/science/> [Accessed: 20-December-2015]
- [21] M. Loncar, "Cavities lead the way," *Nat. Photonics*, vol. 2, no. 2, pp. 76–76, 2008.
- [22] a W. Smith and a Rohatgi, "Ray tracing analysis of the inverted pyramid texturing geometry for high efficiency silicon solar cells ," *Sol. Energy Mater. Sol. Cells*, vol. 29, no. 1, pp. 37–49, 1993.
- [23] P. Papet, O. Nichiporuk, a. Kaminski, Y. Rozier, J. Kraiem, J.-F. Lelievre, a. Chaumartin, a. Fave, and M. Lemiti, "Pyramidal texturing of silicon solar cell with TMAH chemical anisotropic etching," *Sol. Energy Mater. Sol. Cells*, vol. 90, no. 15, pp. 2319–2328, 2006.
- [24] H. Seide, L. Csepregi, and a Heuberge, "Anisotropic Etching of Crystalline Silicon in Alkaline Solutions," *J. Electrochem. Soc.*, vol. 137, no. 11, pp. 249–260, 1990.
- [25] Y. Yang, "Microelectronics Devices Type of Solid Materials," 1988.
- [26] "P-n junction formation." [Online], Available: <http://www.circuitstoday.com/understanding-the-pn-junction> [Accessed: 6-December--2015]

- [27] D. Bouhafs, a. Moussi, a. Chikouche, and J. M. Ruiz, "Design and simulation of antireflection coating systems for optoelectronic devices: Application to silicon solar cells," *Sol. Energy Mater. Sol. Cells*, vol. 52, no. 1, pp. 79–93, 1998.
- [28] B. A. Swatowska, T. O. Stapinski, K. A. Drabczyk, and P. I. Panek, "The role of antireflective coatings in silicon solar cells – the influence on their electrical parameters," *Opt. Appl.*, vol. XLI, no. 2, pp. 487–492, 2011.
- [29] P. Spinelli, M. a Verschuuren, and a Polman, "Broadband omnidirectional antireflection coating based on subwavelength surface Mie resonators.," *Nat. Commun.*, vol. 3, p. 692, 2012.
- [30] G. K. Reeves and H. B. Harrison, "Obtaining the specific contact resistance from transmission line model measurements," *IEEE Electron Device Lett.*, vol. 3, no. 5, pp. 111–113, 1982.
- [31] K. C. Fong, T. C. Kho, A. Fell, E. Franklin, N. Zin, A. W. Blakers, K. R. McIntosh, T. Ratcliff, M. Stocks, J. Bullock, and E. Wang, "Contact Resistivity of Evaporated Al Contacts for Silicon Solar Cells," *IEEE J. Photovoltaics*, vol. 5, no. 5, pp. 1304–1309, 2015.
- [32] A. W. Blakers, J. Zhao, A. M. Milne, A. Wang, and X. Dai, "Characterization of 23 -Percent Efficient Silicon Solar," *Ieee Trans. Electron Devices.*, vol. 37, no. 2, pp. 331–336, 1990.
- [33] Y. Hwang, C. Park, J. Kim, J. Kim, J.-Y. Lim, H. Choi, J. Jo, and E. Lee, "Effect of laser damage etching on i-PERC solar cells," *Renew. Energy*, vol. 79, pp. 131–134, 2014.
- [34] A. Uruena, L. Tous, F. Duerinckx, I. Kuzma-Filipek, E. Cornagliotti, J. John, R. Mertens, and J. Poortmans, "Understanding the Mechanisms of Rear Reflectance Losses in PERC Type Silicon Solar Cells," *Energy Procedia*, vol. 38, pp. 801–806, 2013.
- [35] U. Zastrow, L. Houben, D. Meertens, a. Grohe, T. Brammer, and E. Schneiderlöchner, "Characterization of laser-fired contacts in PERC solar cells: SIMS and TEM analysis applying advanced preparation techniques," *Appl. Surf. Sci.*, vol. 252, pp. 7082–7085, 2006.
- [36] "26th European Photovoltaic Solar Energy Conference and Exhibition 21.7 % EFFICIENT PERC SOLAR CELLS WITH ALO," *Sol. Energy*, pp. 1115–1119.
- [37] C. Kranz, S. Wyczanowski, U. Baumann, S. Dorn, S. Queisser, J. Schweckendiek, D. Pysch, and T. Dullweber, "Industrial Cleaning Sequences for Al₂O₃-passivated PERC Solar Cells," *Energy Procedia*, vol. 55, no. 0, pp. 211–218, 2014.

- [38] B. Soediono, “No Title No Title,” *J. Chem. Inf. Model.*, vol. 53, no. September, p. 160, 1989.
- [39] D. A. R. Barkhouse, O. Gunawan, T. Gokmen, T. K. Todorov, and D. B. Mitzi, “Device characteristics of a 10.1% hydrazine-processed Cu₂ZnSn(Se,S)₄ solar cell,” *Prog. Photovoltaics Res. Appl.*, vol. 20, no. 1, pp. 6–11, 2012.
- [40] S. Gatz, J. Müller, T. Dullweber, and R. Brendel, “Analysis and Optimization of the Bulk and Rear Recombination of Screen-Printed PERC Solar Cells,” *Energy Procedia*, vol. 27, pp. 95–102, 2012.
- [41] B. Hallam, A. Urueña, R. Russell, M. Aleman, M. Abbott, C. Dang, S. Wenham, L. Tous, and J. Poortmans, “Efficiency enhancement of i-PERC solar cells by implementation of a laser doped selective emitter,” *Sol. Energy Mater. Sol. Cells*, vol. 134, pp. 89–98, 2015.
- [42] E. Cornagliotti, “a Study on the Impact of Rear Side Polishing in Perc Solar Cells,” pp. 561–566.
- [43] M. Kim, D. Kim, D. Kim, and Y. Kang, “Analysis of laser-induced damage during laser ablation process using picosecond pulse width laser to fabricate highly efficient PERC cells,” *Sol. Energy*, vol. 108, pp. 101–106, 2014.
- [44] S. Zhao, Q. Qiao, S. Zhang, J. Ji, Z. Shi, and G. Li, “Rear passivation of commercial multi-crystalline PERC solar cell by PECVD Al₂O₃,” *Appl. Surf. Sci.*, vol. 290, pp. 66–70, 2014.
- [45] O. The, W. Kern, and P. Setup, “RCA-1 Silicon Wafer Cleaning,” *Film*, vol. 2, pp. 2–4, 1960.
- [46] S. M. De de Nicolas, “a-Si : H/c-Si heterojunction solar cells : back side assessment and improvement,” 2012.
- [47] M. Aslam, “Bulk etching of silicon wafer and development of a polyimide membrane,” *J. Phys. Conf. Ser.*, vol. 439, p. 012029, 2013.
- [48] S. Operating, S. Operating, P. Faculty, P. Faculty, R. White, R. White, M. Engineering, M. Engineering, S. Office, S. Office, P. Nowak, P. Nowak, T. Emergency, T. Emergency, M. Services, M. Services, N. Acid, N. Acid, C. Etching, C. Etching, E. Society, E. Society, H. Acid, H. Acid, G. A. Acid, G. A. Acid, I. Hf, I. Hf, T. Ems, T. Ems, M. Requirements, and M. Requirements, “Isotropic Silicon Etching using HF/Nitric/Acetic Acid (HNA),” *Emerg. Med. Serv.*, vol. 73246, no. 617, pp. 2–6, 2007.
- [49] J. Rentsch, R. Ackermann, K. Birmann, H. Furtwängler, J. Haunschild, G. Kästner, J. Nievendick, A. Oltersdorf, S. Rein, A. Schütte, M. Zimmer, and R. Preu, “Wet Chemical Processing for C-SI Solar Cells - Status and Perspectives,” *Proc. 24th EPVSEC*, no. September, pp. 21–25, 2009.

- [50] K. O. H. Etching and D. Procedures, "KOH etching of Silicon KOH ETCHING AND DECONTAMINATION PROCEDURES," pp. 2–7, 2012.
- [51] J. R. Lloyd, "The effect of passivation thickness on the electromigration lifetime of Al/Cu thin film conductors," *J. Vac. Sci. Technol. A Vacuum, Surfaces, Film.*, vol. 1, no. 2, p. 455, 1983.